Exploring the chemistry of syngas on a m-ZrO_2 surface with computational methods

University of Jyväskylä
Department of Chemistry
Master's thesis
15.9.2023
Rasmus Ikonen

Tiivistelmä

Isosynteesillä tarkoitetaan katalyyttistä prosessia, jossa synteesikaasusta valmistetaan haarautuneita hiilivetyjä, kuten isobutaania ja isobuteenia. Vaikka kyseinen reaktio on tunnettu jo vuosikymmeniä, isosynteesin potentiaaliset käyttökohteet synteettisten polttoaineiden tuotannossa on herättänyt kiinnostuksen uudelleen. Isosynteesin yksityiskohtainen reaktiomekanismi on edelleen tuntematon, ja siksi reaktio tarjoaa kiinnostavan tutkimuskohteen. Isosynteesireaktion katalyytteinä toimii siirtymämetallioksidit, joista tutkituin on zirkoniumdioksidi, eli zirkonia. Tässä pro gradu tutkielmassa perehdyttiin tarkemmin zirkonian katalyysikemiaan erityisesti isosynteesin kontekstissa.

Tutkielman ensimmäisessä osassa perehdyttiin kirjallisuuden kautta isosynteesiin, sitä ympäröivään synteesikaasun kemiaan, sekä isosynteesissä katalyytteinä toimiviin metallioksideihin ja niiden ominaisuuksiin. Toinen osa käsittää laskennallisen tutkimuksen, jossa tiheysfunktionaaliteoriaan (DFT) pohjautuvien laskujen avulla tutkittiin isosynteesin ensimmäisiä alkeisaskeleita askelmaisella m-ZrO_2-pinnalla. Tarkemmin reaktioverkostoa tutkitaan vedyn dissosiatiivisesta adsorptiosta aina ensimmäisen hiili-hiili-sidoksen muodostumiseen.

Tutkimuksessa pyrittiin tunnistamaan ne alkeisaskeleet, jotka johtavat C–C sidoksen muodostumiseen m-ZrO_2-pinnalla, ja määrittämään näille askeleille reaktio- ja aktivaatioenergiat. Aktivaatioenergioiden määrittämistä varten alkeisaskeleille etsittiin siirtymätiloja NEB-menetelmällä. Lisäksi projektissa hyödynnettiin Ab initio molekyylidynamiikkaa, jolla simuloitiin ajan funktiona synteesikaasun käyttäytymistä m-ZrO_2-pinnalla. Tutkituista reaktioaskelista C–O sidoksen katkeamiselle määritettiin korkein aktivaatioenergia, kun taas C–C sidoksen muodostumisen havaittiin etenevän lähes ilman reaktiovallia.

Abstract

Isosynthesis is a catalytic process, in which synthesis gas is transformed to branched hydrocarbons such as isobutane and isobutene. Although the reaction has been known for decades, the potential applications in the production of more sustainable fuels have caused a renewed interest in this reaction. The detailed reaction mechanism of isosynthesis is still unknown, and therefore the reaction offers an interesting topic for research. Typical catalysts for the isosynthesis are transition metal oxides, and the most studied one is zirconium dioxide, or zirconia. In this master's thesis, the chemistry of catalytic zirconia was in the context of isosynthesis.

In the first part of this thesis, isosynthesis and related syngas chemistry, as well as properties of catalytic oxides are investigated through earlier literature. The second part of the thesis involves a computational study, in which DFT based calculations are used to study the first elementary steps of isosynthesis on a stepped m-ZrO_2 surface. More precisely, the reaction network is studied from the dissociative adsorption of hydrogen to the formation of the first carbon-carbon bond.

The aim of this thesis was to identify the elementary steps that lead to the formation of the first C–C bond on m-ZrO_2 surface, and to determine the reaction energies and the activation energies for these steps. To determine the activation energies, transition states for these reactions had to be found via NEB method. In addition to the static DFT calculations, Ab initio molecular dynamics was used in the project to simulate the synthesis gas on the m-ZrO_2 surface as a function of time. The highest activation energy was found for the breaking of the C–O bond, while the formation of the C–C bond was found to be almost barrierless.

Preface

This master's thesis was carried out in the University of Jyväskylä for the department of chemistry. The calculations were mostly conducted during summer 2022. The computational resources for the heavy calculations were provided by CSC. The thesis was carried out partly as a part of Synjet project, which aims to find sustainable routes to manufacture jet fuel. The thesis was written between the years 2022 and 2023. For the literacy section, the most used databases for the resource gathering were Web of science and Jykdok.

I would like to thank my supervisors Karoliina Honkala and Ville Korpelin, as well as Toni Kiljunen who helped with molecular dynamics. I also want to thank my family and friends who have supported me throughout my studies.

List of acronyms

AFM Atomic force microscopy

AIMD Ab initio molecular dynamics

BO Born-Oppenheimer (approximation)

DFT Density functional theory

FT Fischer-Tropsch

GGA Generalized gradient approximation

HF Hartree-Fock

IR Inrfared

KDE Kernel density estimation

KS Kohn-Sham

LDA Local density approximation

MD Molecular dynamics

NEB Nudged elastic band (method)

SCF Self-consistent field

STM Scanning tunneling microscopy

TPD Temperature programmed desorption

WGS Water-gas shift (reaction)

XC Exchange-correlation (functional)

XPS X-ray photoelectron spectroscopy

XRD X-ray diffraction

YSZ Yttria-stabilized zirconia

vdW van der Waals

Contents

Abstract iii

Preface iv

List of acronyms v

1 Introduction 1

2 Heterogeneous catalysis 2

2.1 Computational catalysis 2

2.1.1 Density functional theory 5

2.1.2 Choosing the functional 7

2.2 Thermodynamics and kinetics 8

2.3 Ab initio molecular dynamics 9

2.4 Experimental methods in catalysis research 10

3 Syngas chemistry 12

3.1 Methanol synthesis 13

3.2 Fischer–Tropsch 14

3.3 Isosynthesis 16

3.3.1 Selectivity in isosynthesis 17

4 Metal oxides 19

4.1 Acid-base properties 21

4.2 Metal oxides in catalysis 21

4.3 Modification of oxide catalysts 22

4.3.1 Doping 23

4.3.2 Nanostructuring 24
4.4 Zirconia 24
4.4.1 Reducibility of zirconia 26
4.4.2 Zirconia in heterogeneous catalysis 27

5 Isosynthesis on zirconia 28

5.1 Initial phases 29
5.1.1 Dissociative adsorption of H_2 29
5.1.2 CO adsorption 31
5.2 CO hydrogenation and reaction intermediates 32
5.2.1 Formate formation 32
5.2.2 Formaldehyde and methoxy formation 33
5.3 Chain growth and branching mechanism 34
5.4 Formation of side products 34
5.4.1 CO_2 formation 35
5.5 Modified zirconia in isosyntheis 36

6 Computational details 37

6.1 Computational methods 38
6.2 The m-ZrO_2 model 40
6.2.1 The bulk structure 40
6.2.2 Surfaces 41
6.2.3 Thickness of the surface 43

7 DFT results 44

7.1 Syngas adsorption 44

7.1.1 Dissociative adsorption of H_2 45
7.1.2 Adsorption of CO 47
7.2 CO hydrogenation 48
7.2.1 First hydrogenation 48
7.2.2 Formaldehyde and methoxy formation 50
7.3 C–O bond breaking 52
7.4 C–C coupling 54
7.5 Adsorption of isobutane and isobutene 56
7.6 Effect of coadsorbates 57
7.7 Summary of results 61

8 DFT molecular dynamics for syngas 63

8.1 Results of MD simulations 65
8.1.1 Observed chemistry 66
8.1.2 Surface restructuring 69
8.2 Limitations of the MD model 70

9 Conclusions 71

1 Introduction

Synthetic jet fuel is a topic that has raised interest in various points in time. Environmental questions have sparked this interest again and finding more environmentally friendly methods to produce jet fuels is an attractive goal. Synthetic jet fuel could offer a way to reduce oil dependency and make production of jet fuels more sustainable. This quest for more sustainable jet fuels is also the underlying motivation for the subject of this thesis.

The production of branched hydrocarbons, more specifically compounds with a structure similar to isobutane and isobutene has been a subject of interest in the fuel industry for a long time.[1] These branched molecules are important reactants in the production of multiple fuel additives that are used to improve performance of fuels.[1] Moreover, isobutene and isobutanol could also be used in the production of synthetic jet fuels via isobutanol oligomerization [2, 3]. There are many ways to produce these branched hydrocarbons. One particularly interesting method is called isosynthesis, a catalytic reaction which turns synthesis gas, a mixture of CO and H_2 catalytically to branched hydrocarbons. Catalysts for isosynthesis are typically oxides, the most well-known one being zirconium dioxide (ZrO_2) also known as zirconia [4, 5, 6]. Even though isosynthesis has been known for decades, similar to many catalytic reactions understanding of this reaction on the atomic level is still lacking.

The aim of this thesis is to investigate chemistry associated with isosynthesis, and in a broader picture chemistry of syngas on catalytic oxide surfaces. The focus is on the chemistry catalyzed by zirconia in the presence of CO and H_2, with high emphasis on computational chemistry. Modern computational tools have become an important part of catalyst research since they can offer mechanistic insights on a scale that would be difficult to achieve solely via experimental methods. This thesis includes a computational study on the first steps of isosynthesis on monoclinic zirconia, starting from adsorbed CO and H_2 to the formation of the first C–C bond. The purpose of these calculations is to build a basis for a comprehensive reaction network and mechanism, which further studies can hopefully build on.

2 Heterogeneous catalysis

A catalytic reaction is a chemical process in which one component called a catalyst plays a key role in the reaction without being consumed by the reaction. Heterogeneous catalysis means in general a catalytic process that has the catalyst and the reactants in different phases and the catalytic reaction happens at the interface of these phases. Commonly the catalyst is some solid material and the reactants are gas or liquid, meaning that the reactions take place at the surface of the catalytic material.[7] To address sometimes heard misconception, a catalyst does not change thermodynamics of reactants and products, meaning that if the product molecules are less stable than the reactant molecules catalyst can't make this reaction exothermic. The purpose of the catalyst is to offer a reaction pathway that has a low enough activation energy and high enough activity and selectivity to make the transformation from one set of chemicals to another feasible, both in practical and economic sense. Figure 1 shows schematic illustration of heterogeneous catalysis where species A and B are combined to form species AB. In contrast to a non-catalytic reaction, in heterogeneous catalysis the reaction consists of the adsorption of reacting molecules, the actual reaction that can include any number of steps and finally the desorption of products. The mechanism depicted in figure 1 is called the Langmuir-Hinshelwood mechanism in which all the reactants are assumed to be adsorbed to the catalyst before reacting. In contrast, the Eley-Rideal mechanism describes a situation where one reactant is in the gas phase. [8]

Heterogeneous catalysis is extremely important for the modern society. In fact, over 80% of all processes in chemical industry are based on heterogeneous catalysis. [9] Most important example is probably the ammonia synthesis via the Haber-Bosch process. This over 100 years old process uses an iron catalyst in high pressures and temperatures to transform N_2 and H_2 to NH_3. [9].

2.1 Computational catalysis

Computational tools have become increasingly important for heterogeneous catalysis. A latin term ab initio is used to describe methods in computational chemistry that involve electronic structure calculations from quantum mechanical description

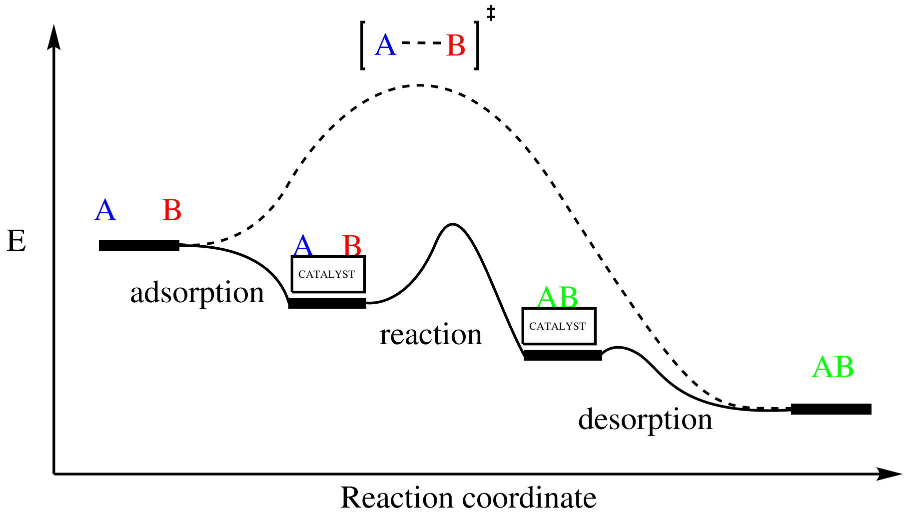

Figure 1: An illustrative example of heterogeneous catalysis. The dashed line represents the non-catalytic pathway and the solid line is pathway offered by the catalyst.

of atoms and molecules. Ab initio calculations can give the atomic level insight which is difficult to obtain via experimental methods. For example, ab initio methods can be used to study and evaluate individual reaction steps, while experimental methods usually give information about the entire reaction.[8] The basis of the computational chemistry is in the quantum mechanical description of studied systems. Often problems in chemistry involve solving the time independent atomistic Schrödinger equation.

$$\hat{H}\psi = E\psi, \tag{1}$$

where $\hat{H}$ is the Hamiltonian and ψ is a wave function. The molecular Hamiltonian includes kinetic energy operators $\hat{T}_N$ and $\hat{T}_e$ for atomic nuclei and electrons, repulsions between two nuclei $\hat{V}_{NN}$, repulsion between two electrons $\hat{V}_{ee}$ and attraction between nuclei and electrons $\hat{V}_{eN}$.

$$\hat{H} = \hat{T}_N + \hat{T}_e + \hat{V}_{NN} + \hat{V}_{eN} + \hat{V}_{ee}. \tag{2}$$

Here the total kinetic energy operator $\hat{T}_N + \hat{T}_e$ written in atomic units is [10]

$$\hat{T} = -\sum_{A=1}^{M} \frac{1}{2M_A}\nabla_A^2 - \sum_{i=1}^{N} \frac{1}{2}\nabla_i^2, \tag{3}$$

where M_i is the mass of the nucleus i, M is the number of nuclei, and N is the number of electrons. Potential energy $\hat{V}_{NN} + \hat{V}_{eN} + \hat{V}_{ee}$ is similarly in atomic units [10]

$$\hat{V} = \sum_{A=1}^{M}\sum_{B>A}^{M} \frac{Z_A Z_B}{|R_A - R_B|} + \sum_{i=1}^{N}\sum_{A=1}^{M} \frac{Z_A}{|r_i - R_A|} + \sum_{i=1}^{N}\sum_{j>i}^{N} \frac{1}{|r_i - r_j|}, \tag{4}$$

where R_A and R_B are the coordinates of the nuclei A and B, and r_i and r_j are the coordinates of the electrons i and j. In computational science, it is more practical to use atomic units to mitigate floating point errors that can arise when calculations include operations with extremely precise values like the Planck constant and elementary charge in SI units. When the time independent Schrödinger equation is solved in this form, the energies are given in Hartrees.[10]

For any multielectron system there is no analytical solution to the Schrödinger equation, and therefore numerical tools must be used. Usually the calculations also include multiple approximations to make them feasible. One of the most common ones is the Born-Oppenheimer (BO) approximation, sometimes referred to as the adiabatic approximation, since the main idea of this approximation is that movement of electrons happen on so much faster timescales than the movement of nuclei that the nuclei and the electrons can be treated separately. Even though the BO-approximation is commonly used there are some cases where this approximation breaks down, for example when potential surfaces of different energy levels come close together. [10]

One of the most basic approaches to solve the time independent Schrödinger equation for molecules is the Hartree-Fock (HF) method. The HF-method is a self-consistent field (SCF) method, which means that the solution is found iteratively using the mean field approximation. HF method is usually not accurate enough for applications in chemistry because it doesn't account for the full electronic correlation.[10] There exist many so-called post-HF methods that mitigate this problem, but these methods usually increase the computational cost significantly. [11]

2.1.1 Density functional theory

Density functional theory (DFT) is commonly titled as the workhorse of computational catalysis. This is because it makes possible to calculate energies for large systems like catalytic surfaces with usually good enough accuracy while still maintaining a relatively low computational cost.[11]

The justification for the density functional theory is given by the two theorems introduced by Kohn and Hohenberg. The first theorem states that the total energy is a unique functional of electron density, and the second that energy as a functional of electron density is minimized by the true ground state electron density. This leads to the fact that the total energy of ground state can be expressed as a functional of the ground state electron density. [12] This by itself is not really practical, but the formalism developed by Kohn and Sham opened the possibility to apply DFT effectively in computational work. This formalism allows a SCF algorithm that resembles the one used in the Hartree-Fock method. In KS-DFT, electron density $\rho(r)$ is expressed with non-interacting single-electron wave functions $\phi_j(r)$ called Kohn-Sham orbitals. [12, 11, 13]

$$\rho(r) = \sum_{i}^{N} |\phi_i(r)|^2, \tag{5}$$

and Kohn-Sham DFT involves solving Kohn-Sham equations. [12, 11]

$$\left(\frac{\hbar^2}{2m_i}\nabla^2 + \upsilon_{\text{eff}}(r)\right)\phi_j(r) = \epsilon_j\phi_j(r), \tag{6}$$

where $\upsilon_{\text{eff}}(r)$ is the effective potential which depends on electron density, and ϵ_j is the energy for a single KS-orbital.

$$\upsilon_{\text{eff}}(r) = \int \frac{\rho(r')}{|r-r'|}dr' + \upsilon_{\text{XC}}(r) - \sum_{A}^{M} \frac{Z_A}{|r-R_A|} \tag{7}$$

Here, the first integral is the Hartree potential, which describes the electrostatic potential caused by the electron density. The equation in the sum is external potential. This is the same potential also found in the equation 4. υ_{XC} is potential raised by exchange correlation energy E_{XC} and it is defined as functional derivative

$$v_{\mathrm{XC}} = \frac{\delta E_{XC}(r)}{\delta n(r)}. \tag{8}$$

Equation 8 is important as it provides an approximation for the exchange-correlation functional. The exact form of the exchange-correlation functional is unknown and therefore different approximations are used. Choosing the right exchange-correlation functional is discussed in the section 2.1.2.

Equations 7 and 6 tell us that to solve the electron density we need an effective potential which again is solved with the electron density. Here self-consistent field method come to the picture. Since effective potential depends on electron density, an initial guess is needed. After the initial guess, the SCF cycle begins. Figure 2 shows a simplified scheme for a DFT SCF cycle. Convergence of the SCF cycle can be improved by implementing density mixing, which means that instead of just using the density given by the previous cycle as an input for the next cycle, a better input density is calculated from several previous densities.[14]

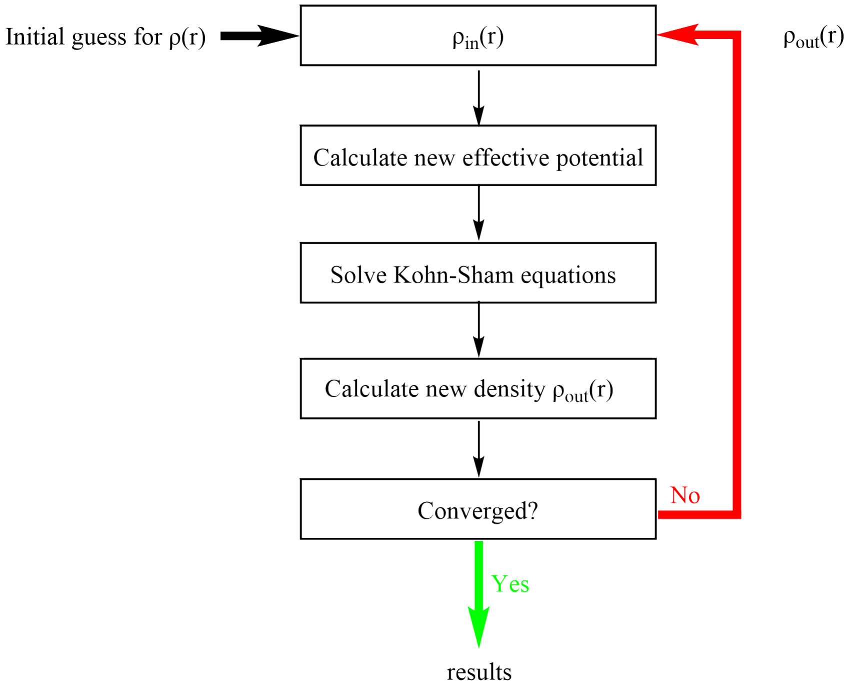

Figure 2: Simplified scheme for the self-consistent field method in DFT.

2.1.2 Choosing the functional

For efficient use of DFT, it is important to know what the DFT can and cannot do. First of all, the choice of the exchange-correlation functional is essential in defining the performance of the model. The starting point for the XC functional is the local density approximation (LDA) which is a class of functionals that construct the XC functional by assuming that the υ_{XC} at each point is given by the uniform electron gas.[11] This is, however, an insufficient approximation for applications in chemistry since LDA overestimates molecular bond energies. [15] To capture the effect of varying electron density, the generalized gradient approximation (GGA) is usually implemented. In this class of functionals local gradient of the electron density is used in construction of the functional. GGA-DFT has been utilized for calculating chemisorption since late 1990s [15]. Two common GGA-based functionals used in computational chemistry are Perdew-Wang (PW91) and Perdew-Burke-Ernzerhof functional (PBE).[12, 11]

Functionals based on the GGA are suited for many problems, but GGA have some weaknesses. One of the problems encountered with some oxides is overdelocalization of electron density. While DFT with commonly used GGA functionals works well with metals, problems arise when the electron density varies rapidly and is more localized. This is why insulating oxides like zirconia can be problematic. Especially problematic species are oxides that include highly localized f-orbitals, such as $\mathrm{CeO_2}$. [16] There are two commonly used work-arounds for this problem. The first commonly used method is the Hubbard-correction, also known as DFT + U. In this method, a correction term based on the Hubbard model is added to the DFT. One way to do this is shown by equation 9[16]

$$E_{\mathrm{DFT\,+\,U}} = E_{\mathrm{DFT}} + \frac{1}{2}\sum_{I,\sigma}\sum_{nl} U^{l}_{nl}[\mathrm{Tr}(n^{I,\sigma}_{nl}) - \mathrm{Tr}(n^{I,\sigma}_{nl} n^{I,\sigma}_{nl})], \tag{9}$$

where E_{DFT} is energy from uncorrected DFT, U^{l}_{nl} is the effective electron-electron interaction parameter, $n^{I,\sigma}_{nl}$ is the occupation matrix, and Tr is a trace of matrix. for a given shell of the atom I.[16]. The Value for this correction term is usually found empirically for the studied system. A computationally more demanding option is to use hybrid functionals that include some exact exchange terms calculated with the HF method. Example of this kind of XC functional is B3LYP.[11]

Another problem with DFT is that it doesn't include natively the effects of dispersion. In other words, DFT cannot describe physisorption on its own and therefore some kind of a correction for van der Waals forces must be included into the calculations. [11]

2.2 Thermodynamics and kinetics

DFT calculations are used to get the physical properties of a chemical system, importantly the total energy of a given system, which can be used to calculate strength of interactions. In heterogeneous catalysis, DFT is especially used to reveal thermodynamics and chemical kinetics of catalytic reactions. For example, adsorption and desorption of surface species is a fundamental part of heterogeneous catalysis, and DFT is commonly used to calculate adsorption energies. This can be done by subtracting total energy of the surface and the gas phase adsorbate from the total energy of the surface-adsorbate complex (equation 10).

$$E_{\mathrm{ads}} = E_{(\mathrm{x}\,+\,\mathrm{surface})} - E_{\mathrm{x}}(g) - E_{(\mathrm{surface})}, \tag{10}$$

where $E_{(\mathrm{x}\,+\,\mathrm{surface})}$ is the energy for the surface-adsorbate complex, $E_{\mathrm{x}}(g)$ is energy for the adsorbing molecule in gas phase, and $E_{(\mathrm{surface})}$ is the energy of the surface structure.

Calculating adsorption energies is meaningful only if the structure of adsorption complex is physically sensible and corresponds to a local energy minimum. This is why adsorption calculations always involve structure optimization which means that the geometry of calculated system is varied until pre-set force convergence criteria are met. Structure optimization also produces minimum energy bond lengths and bond angles.

When investigating reaction networks and chemical kinetics, finding transition states and corresponding activation energies becomes an important task. For example, reaction rate constants can be calculated via the Arrhenius equation [7]

$$k = Ae^{\frac{-\Delta E_{\mathrm{a}}}{k_{\mathrm{B}}T}}, \tag{11}$$

where prefactor A is a constant, E_a is the activation energy, k_B the Boltzmann constant and T temperature. The activation energy for the forward reaction is essentially the energy difference between an initial state and a transition state (equation 12).

$$E_a = E_{\mathrm{T}} - E_{\mathrm{i}} \tag{12}$$

The reaction energy can be likewise calculated as a energy difference between the initial and final states of an elementary reaction (equation 13).

$$\Delta E = E_{\mathrm{i}} - E_{\mathrm{f}} \tag{13}$$

A transition state corresponds to a saddle points on a potential energy surface, and finding these states is considerably a more difficult task than optimizing a structure to the minimum energy. One way to find a transition state for a reaction using DFT calculations is via the Nudged elastic band-method (NEB). The idea behind NEB is to find the minimum energy path (MEP) between two states and find the point on the path in which the force component along the path is minimized. [11].

NEB calculations are used extensively in computational catalysis, especially when screening possible reaction paths for catalytic reactions. Practical examples of use cases include investigation of glycerol hydrodeoxygenation reaction network on a Re-based catalyst [17], investigating the mechanism of the Fischer-Tropsch reaction network on a cobalt catalyst [18] and studying mechanism of methanol synthesis from CO and H_2 on a Cu-catalyst. [19]

2.3 Ab initio molecular dynamics

Since real chemical systems are not static but in constant movement, and simulating movement of molecules as a function of time is an attractive idea. Molecular dynamics (MD) can also be carried out via models based entirely on classical mechanics, but in chemistry ab initio molecular dynamics (AIMD) are usually implemented. In AIMD, forces needed for simulating dynamics are calculated via ab initio methods, typically with DFT, and the calculated forces are used to integrate equations of motion for atoms and molecules.[11]

Typical MD-simulations are conducted in a canonical ensemble which means constant temperature, volume and the number of particles. There are multiple thermostats used for keeping the temperature constant, like Nosé-Hoover, Berendsen or Langevin thermostats, but especially the first two thermostats are known to have difficulties maintaining uniform average temperature throughout the system. [20]. Time steps for MD-simulations are usually no larger than 10 fs. [11]

Typical applications for AIMD are simulating complex materials such as liquids or amorphous materials, or exploring energy surfaces to help finding local energy minima. [11] DFT-MD can be used for example to simulate proton migration and dissociation of water on oxides surfaces, like Sato *et al.*[21] have done for hydrated cubic zirconia. Their initial structure consisted a six layer slab of cubic ZrO_2 with a (110) surface, and 27 H_2O molecules. Simulations demonstrated that at 500 K both Zr-OH_2 and Zr-OH^- species exist on this zirconia surface, and proton hopping can happen between Zr-H_2O and Zr-OH^- surface species or between surface species and surrounding water.

2.4 Experimental methods in catalysis research

The main focus of this thesis is on computational chemistry. However, since a large portion of heterogeneous catalysis is experimental and the experimental research goes hand in hand with the computational studies, some light should also be shed on the common experimental methods used in the research of heterogeneous catalysis. The most of the methods introduced here are from the textbook *Concepts of modern catalysis and kinetics* by Chorkendorff and Niemansverdriet. [8]

In computational research, modelling a real catalyst accurately is a major challenge and therefore experimental characterization of catalysts is invaluable. Catalyst characterization involves multitude of methods that include methods to define the structure of a catalytic material as well as methods to analyze the chemistry. Probably the most common techniques used for analyzing the structures of solid catalysts are based on X-ray diffraction (XRD). The main idea behind XRD is to utilize the Bragg's law to extract information about the crystal structures. Radiating a crystalline sample with x-rays gives a diffraction pattern that can be deciphered using a Fourier transform to get the crystal structure of the given sample. XRD is extensively used to determine the crystalline phase of the sample. [22, 23, 24].

X-rays can also be used to create photoelectrons via the photoelectric effect which is utilized in X-ray photoelectron spectroscopy (XPS). XPS is also among the most used techniques for surface characterization since it can provide accurate information about the surface composition, and it can be used to investigate how catalytic nanoparticles are dispersed on a surface. XPS is commonly used in conjunction with the XRD and can provide information such as concentration of dopant atoms in structures. [25] XPS can also be used to detect oxygen vacancies on oxide structures. [26]

Other common spectroscopic methods such as UV-Vis and infrared (IR) spectroscopy are also extensively used in catalysis. Especially infrared spectroscopy has been found useful in identification of adsorbed surface species. One benefit of IR-spectroscopy is that it can be applied in situ, meaning that the measurements can be done for real catalysts under actual reaction conditions. One specific type of IR-spectroscopy used to some extent in catalysis is diffuse reflectance infrared Fourier transform spectroscopy (DRIFTS), and as it is indicated in the name, it is used to gather an accurate infrared spectrum from diffused reflectance. The key benefit of this technique is that the spectrum can be measured from powder samples. This technique is sensitive to surface species and therefore useful in heterogeneous catalysis. [27]. Raman spectroscopy can also be used to detect surface defects due to changes in bonding energies at a surface. The intensity ratio of defect induced vibration modes to other vibration modes can be used as a descriptor for defect concentrations.[28].

Precise information about the surface geometry can be obtained with the scanning tunnelling microscopy (STM) and the atomic force microscopy (AFM). These techniques can give extremely precise information about a atomic structure of the surface via probes that detect individual atoms. In STM, the probe is used to detect currents that are induced by the tunnelling of electron density. AFM, on the other hand measures movement of an extremely delicate probe head via the forces induced by surface atoms. These techniques along with electron microscopy methods are useful in characterization and observation of small structures like atomic defects on catalytic surfaces. [28]

Research of catalytic processes involves methods like temperature programmed desorption (TPD) in which stream of desorbing species is monitored as a function of temperature. This method gives valuable information about the adsorption energies of different species and can be used to determine surface coverage and rates of desorption. Closely related to this technique is also temperature-programmed reduction (TPR), which is used to investigate reducibility of a catalyst. Reducibility of a catalyst is discussed in more detail in section 4.

3 Syngas chemistry

Synthesis gas or syngas is a term that means generally any mixture of CO and H_2. Syngas is a versatile starting material with a large range of applications. The most important processes involving syngas include methanol synthesis, hydroformylation reactions and production of heavier hydrocarbons including Fischer–Tropsch synthesis for production of linear carbon chains as well as isosynthesis for producing branched hydrocarbons. [8]

Nowadays, most of the syngas is made from natural gas via methane reforming.[29, 30] There exist more than one way of transforming methane to syngas, and different methods can give different CO:H_2 ratios. One of the most common processes is the catalytic steam reforming reaction (reaction R1). In this reaction, methane and water vapor are transformed at high temperatures and pressures to syngas. The reaction is catalyzed by group VIII transition metals such as Rh, Ru, Ni and Ir. [31]. Equation R1 depicts the reaction on a nickel-based catalyst. [1]

$$\mathrm{CH_4(g) + H_2O(g) \rightleftharpoons CO(g) + 3\,H_2(g)} \tag{R1}$$

Another viable way to produce syngas is a dry reforming reaction in which the water vapor in steam reforming is replaced by CO_2 (reaction R2). Similarly to the steam reforming, nickel is also viable the catalyst for the dry reforming method. [31]

$$\mathrm{CH_4(g) + CO_2(g) \rightleftharpoons 2\,CO(g) + 2\,H_2(g)} \tag{R2}$$

The third known reaction for syngas production is the catalytic partial oxidation of methane [31] (reaction R3).

$$CH_4(g) + \frac{1}{2}O_2(g) \rightleftharpoons CO(g) + 2\,H_2(g) \tag{R3}$$

This reaction has not seen as wide industrial use as the steam reforming reaction due to slower advancement in the catalyst technology. Particularly catalyst deterioration due to carbon deposition has been a problem. [32] Partial oxidation has still attracted a lot of interest because the ratio of produced CO and H_2 is more optimal for further processing like Fischer-Tropsch synthesis which is discussed in section 3.2. [31, 32]. Catalysts for the catalytic partial oxidation are again transition metals, and Ni based catalysts can also be used for this reaction. [31]

Closely related to the syngas chemistry is the water-gas shift (WGS) reaction (reaction R4). It transforms CO and water or steam to CO_2 and hydrogen gas [33, 34], meaning that the methanol reformation can be coupled with the WGS reaction for enhanced hydrogen production.

$$CO + H_2O \rightleftharpoons CO_2 + H_2 \tag{R4}$$

In the context of green chemistry, natural gas is not the most attractive reactant, and therefore there is an ongoing effort to find more sustainable ways to produce syngas, including production using biomass as the source of methane [35, 36]. From an environmental perspective hydrogen production via the WGS reaction also has problems due to formed CO_2. Green hydrogen can be produced for example via electrolysis of water by using renewable energy like solar or wind power. [37]

3.1 Methanol synthesis

Modern industrial methanol synthesis doesn't use pure syngas, but a mixture of CO, CO_2 and H_2 with a ratio of (5:5:90). This mixture is transformed to methanol using a $Cu/ZnO/Al_2O_3$ catalyst at 500-550 K temperature and 50 to 100 bar pressure. [8, 38]. Methanol can be produced by CO reacting with H_2 or H_2O, or CO_2 reacting with H_2. [38]. There is no single reaction that is responsible for the methanol production, but multiple simultaneous processes that all result in formation of CH_3OH molecules.

Since $Cu/ZnO/Al_2O_3$ has become the catalyst used by the industry, Cu based catalysts have been studied extensively. Especially the role of CO in the reaction have been a topic of controversy. Computational studies have confirmed the experimental results that both CO and CO_2 mechanisms are present and contribute to the formation of methanol [19, 39, 40]. It has also been computationally demonstrated that CO is the main carbon source for the methanol if the conversion takes place on Cu^+ species, but on metallic Cu, CO_2 is more likely to be the main carbon source and the mechanism is thus different. [41]. In the industrial reaction conditions, syngas can reduce Cu_2O to a metallic Cu, and on the other hand Cu^+ species are stabilized by water and CO_2, meaning that these different reaction pathways are coupled. [41] This highlights how complicated catalytic processes involving syngas can be. Catalytic processes can indeed include multiple competing pathways even for the same product. In addition to the methanol synthesis, there is also pursuit for synthesizing higher alcohols from syngas, and at least a highly selective method for the synthesis of ethanol has been reported. [42]

3.2 Fischer–Tropsch

The Fischer–Tropsch (FT) process is a widely used method for turning syngas into a mix of mostly linear hydrocarbons. Alkene and alkane formation in the FT process can be described by reaction equations [1]

$$2\,\mathrm{nH_2} + \mathrm{nCO} \longrightarrow \mathrm{C_nH_{2n}} + \mathrm{nH_2O}\cdot \tag{R5}$$

$$(2\mathrm{n}{+}1)\mathrm{H_2} + \mathrm{nCO} \longrightarrow \mathrm{C_nH_{2n+2}} + \mathrm{nH_2O}\cdot \tag{R6}$$

The equations R5 and R6 suggest that the main side product in the FT process is water. Catalysts for the FT synthesis are mostly transition metals, commonly Fe or Co nanoparticles, supported on oxides like SiO_2,TiO_2 or ZrO_2. While cobalt shows high activity, selectivity and stability, its high cost compared to iron is a large disadvantage. [43]. In fact, the activity and selectivity of Fe are quite poor compared to Co, but a low cost makes it a viable catalyst for industry. [1]

When it comes to the reaction conditions, FT synthesis is typically carried out at temperatures between 470 to 620 K and at pressures around 2–6 MPa [44]. Product distribution in FT synthesis follows the Anderson-Flory-Schulz distribution, and the normalized distribution of weights is given by the equation

$$w_i = i(1-\alpha)^2\alpha^{i-1}, \tag{14}$$

where i is the length of the carbon chain and α is the chain growth propagation probability.[8]. In figure 3 this equation is used to plot selectivities for a couple of different chain lengths as function of α.

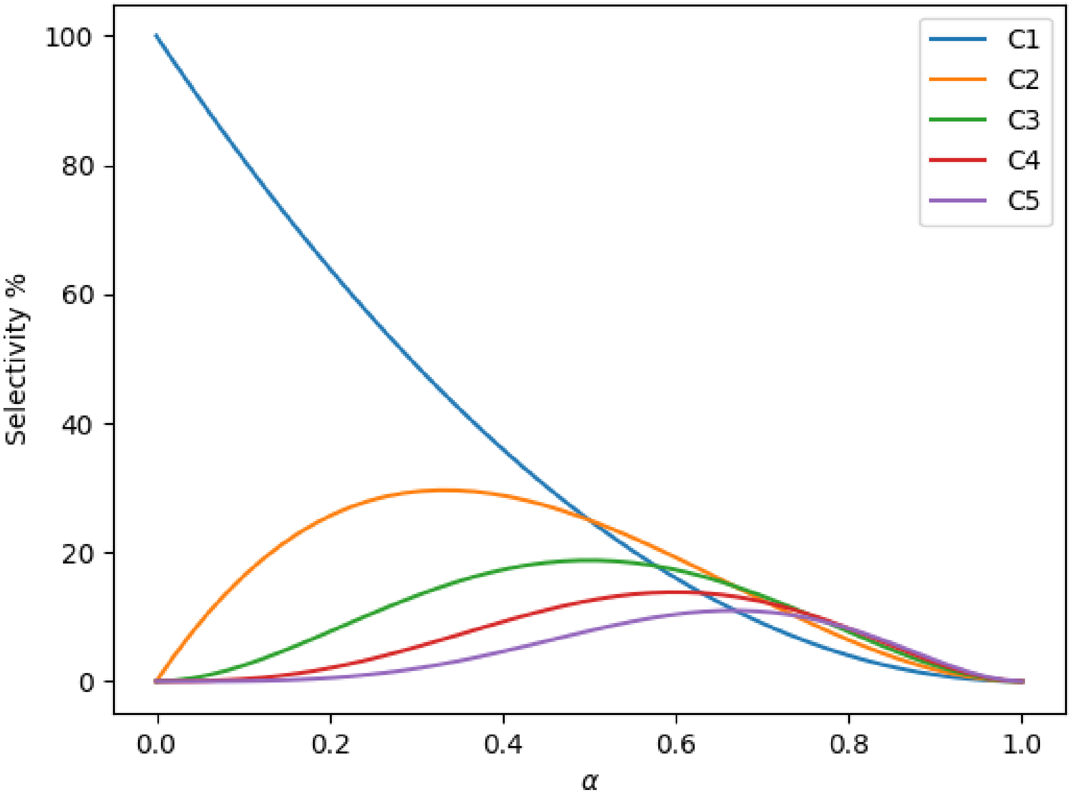

Figure 3: Selectivity for different chain lengths in the FT-process according to the Anderson-Flory-Schulz distribution.

It is suggested that there are two mechanisms in FT synthesis responsible for chain growth. The first one is the carbide mechanism in which C–O bond of adsorbing

CO is broken leaving carbide species on the surface. These carbide species react further to form CH_n species, and the chain growth occurs via coupling of the CH_n monomers.[45] Computational studies have supported the carbide mechanism for the chain growth, [45] and experimental data shows that in cobalt catalyzed FT synthesis CH_n surface species have an active part in chain growth. [46] The second mechanism is based on CO insertion. In this mechanism, instead of the coupling of C_nH_n species, CO molecule is inserted to an existing structure. [46] It is suggested by computational work that at least on a Fe_5C_2 surface both of these mechanisms are present and work synergistically. [47]

DFT calculations by Liu *et al.* [18] have shed some light on the more detailed mechanisms associated with the FT process on a Co catalyst, including CH_n formation and C–C bond formation with different mechanisms. They concluded that CO dissociation and H-assisted CO dissociation leads to the formation of CH and CH_2 species, and chain growth would be initialized by self-coupling between these species forming C_2H_2 and C_2H_4.

3.3 Isosynthesis

Isosynthesis is a catalytic reaction that is closely related to the FT synthesis. Similarly to the FT-synthesis, in isosynthesis, syngas is transformed to a mix of hydrocarbons, but the difference is that instead of linear hydrocarbons the main products are branched hydrocarbons that usually terminate at 4 to 8 carbon. The most important products are four-carbon iso-products, isobutane and isobutene (figure 4). [5] From now on, molecules with the similar four carbon core structure will be referred to as i-C_4 products. The reported temperatures for isosynthesis are usually a bit higher than in the FT synthesis. Temperatures range from 573 to 723 K [48], and pressures are typically less than 5 MPa due to selectivity issues at higher pressures. [5]

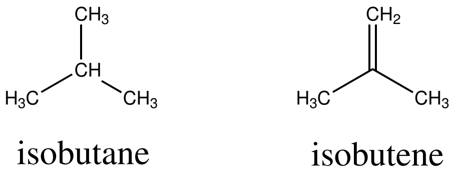

Figure 4: Structures of isobutane and isobutene.

Research of isosynthesis dates back decades and has raised some interest from time to time, but without any major breakthroughs the process has not been so attractive to the chemical industry. The main driving force for research has been the possibility to produce high grade fuels from i-C_4 products. [4, 5]. Nowadays environmental factors play a large role in the newly sparked interest in isosynthesis, since isosynthesis could provide way to shift from petroleum-based products to greener alternatives, given that syngas production could be done in an environmentally friendly way. This search for a better way to manufacture jet fuel is also at the center of this thesis, since the computational part of the thesis is conducted as a part of Synjet, a joint project of multiple academic and industrial partners to find viable greener solution for fuel manufacturing.

A clear distinction to FT synthesis is found from isosynthesis catalysts. Unlike in many other catalytic reactions, the best catalysts for isosynthesis have been found to be irreducible oxides commonly considered to be inert materials. In addition to zirconia, other possible catalysts for isosynthesis include for example thoria (ThO_2) and alumina (Al_2O_3). [4]. Some CeO_2-based catalysts have also been studied [4, 49, 50]. However, the poor stability of CeO_2 at high temperatures poses a challenge for applications in isosynthesis [22]. The stability of CeO_2 could be increased by mixing CeO_2 with other oxides. For example, a CeO_2-TiO_2 catalyst has shown increased thermal stability compared to CeO_2 but even this catalyst suffers from poor stability. [50]

3.3.1 Selectivity in isosynthesis

Catalysts that show high selectivity for $i-C_4$ products are generally inactive, irreducible oxides. (More about the properties of these oxides in section 4). By far, the most studied catalyst for isosynthesis is ZrO_2 because it has high selectivity for i-C_4 products compared to other catalysts like alumina. [5]. Along with the $i-C_4$, other hydrocarbons with differing molecular weights are produced. Usually, the hydrocarbon side products are lighter hydrocarbons, methane having in most cases the highest yield. This is illustrated in table 1, which shows distribution of hydrocarbons on different ZrO_2-based catalysts. The table is combined from two different experimental studies that used similar reaction conditions, and it includes four pure ZrO_2 catalysts manufactured via different methods, as well as one Zn doped catalyst. [51, 52]. Catalysts ZrO_2 and ZrO_2-HT were produced via a hydrothermal method, ZrO_2-Ref was synthesized via a refluxing method and ZrO_2-CP via a precipitation method. More important than the details of manufacturing method are the structural differences between these catalysts. In both studies, high-resolution TEM was used to characterize synthesized catalysts, and according to the results, ZrO_2 and ZrO_2-HT were mostly monoclinic zirconia, while ZrO_2-CP and ZrO_2-Ref exhibited also small amounts of the tetragonal phase. Catalysts also differed slightly by the ratio of acidic and basic sites. The number of acidic and basic sites was calculated via TPD. The acidic sites were defined by NH_3 adsorption, and number of the sites was calculated by integrating the NH_3-TPD curve. Similarly, the basic sites were determined via CO_2-TPD. ZrO_2-HT had base/acid ratio of 1.2, ZrO_2-CP had a ratio of 1.1 and for ZrO_2-Ref the ratio was 0.9. More detailed discussion about the acid-base properties of oxides is in section 4.1.

Table 1 highlights that the manufacturing method of a catalyst can have a significant effect on the product distribution. Indeed, selectivity in isosynthesis for certain products is controlled by multiple factors including temperature, pressure, and the structure of catalyst. For example, it has been shown that pressures above 50 atm increase the formation of longer C_{5+} products. [5] Some aspects affecting selectivity in isosynthesis go well beyond the scope of this thesis. For example Li *et al.* [53] showed that even the reactor material has a remarkable effect on the selectivity of a ZrO_2 based catalyst. They found that a quartz lined stainless steel tubular reactor achieves higher i-C_4 selectivity compared to a steel tubular reactor. The mechanistic details of this phenomenon were not disclosed, but it was concluded that the bare metal walls were responsible for changing the product distribution while the quartz lining inhibited this effect.

Selectivity to hydrocarbons is usually the bottleneck for isosynthesis, and it is common that a catalyst with high activity has poor selectivity towards i-C_4 products. An example of this is seen in table 1. The catalyst ZrO_2-Ref has the highest CO conversion rate but the lowest i-C_4 selectivity, and it also produces a lot more methane than the other catalysts. As seen from the table, CO_2 formation makes up a large portion of the CO conversion, which is one of the largest problems in isosynthesis, not only because CO_2 constitutes usually 40 to 60 percent of product[53], but also because the formation of greenhouse gases is kind of counterproductive

Table 1: Hydrocarbon distribution in isosynthesis for different ZrO_2-based catalysts from literature (C mol%). HT is hydrothermal preparation method, CP precipitation method and Ref refluxing method

Catalysts	CO conv. %	CO_2	C_1	C_2	C_3	C_4	C_5+	$i - C_4/\sum C_4$
ZrO_2[b]	21.1	65.9	7.0	14.3	8.8	57.8	12.1	92.6
ZrO_2-Ref[a]	55.4	16.9	20.2	20.2	9.5	38.9	10.9	75.8
ZrO_2-HT[a]	49.0	30.2	1.4	15.9	7.7	61.0	13.9	90.3
ZrO_2-CP[a]	51.0	24.4	6.5	14.0	6.1	61.7	11.7	90.1
$Zn_1Zr_{300}O_Z$[b]	60.0	20.7	7.0	13.0	8.0	61.7	10.2	93.9

a, Zhang *et al.* [51], reaction conditions: 400°C, 5.0 MPa, CO/H_2 = 1,GHSV = 900 h^{-1}
b, Wu *et al.* [52], reaction conditions: 400 h°C, 5.0 MPa, CO/H_2 = 1,GHSV = 430^{-1}

considering the initial motivation behind this thesis. This is why understanding the formation of CO_2 is important. Study from Li *et al.*[54] that considered the effects of CO_2 in isosynthesis over a zirconia-based catalyst concluded that adding CO_2 gas to the reaction feed only decreased CO_2 formation during the reaction but had no effect on the net formation of hydrocarbons, yet enhancement in the i-C_4 selectivity was observed. This interesting result indicates that CO_2 formation, while reducing total selectivity for hydrocarbon formation, could have an important role in i-C_4 selectivity.

4 Metal oxides

Metal oxides are commonly considered to be semiconductors insulators. One way to understand their behavior is to use the band theory. Transition metals are usually good conductors since they have a partially filled d-band. This also makes the bond formation easier and thereby transition metals are active catalysts. With oxides, however, sp bands of transition metals can hybridize with the oxygen p orbitals, resulting in a new band that is further away from the Fermi level. This leads to lower conductivity and reactivity. [8] Oxides can also be characterized by the ionicity of their chemical bonding. While chemical bonding in oxides is mostly ionic like for example in many oxides of alkali metals, some transition metal oxides have a significant covalent nature.[55]

Another important concept used in the classification of oxides is the reducibility of an oxide. Metal oxides are usually categorized as reducible and irreducible oxides, and a commonly used descriptor for the reducibility is the formation energy of oxygen vacancy.[56, 57] In computational chemistry, this energy is often defined by using O_2 as a reference (equation 15),

$$\Delta E_{\mathrm{v}} = E_{\mathrm{r}} + \frac{1}{2}E_{\mathrm{O}_2} - E_{\mathrm{s}}, \tag{15}$$

where E_{r} is the energy of the reduced surface, E_s is the energy of the stoichiometric surface and E_{O_2} is the energy of the gas phase oxygen.[58, 59] Sometimes, however, instead of O_2, H_2O is used as a reference (equation 16) because the energy of O_2 can be difficult to calculate accurately by DFT. [60]

$$\Delta E_{\mathrm{v}} = E_{\mathrm{r}} + E_{\mathrm{H_2O}} - E_{\mathrm{s}} - E_{\mathrm{H}_2}. \tag{16}$$

Here $E_{\mathrm{H_2O}}$ is the energy of the gas phase H_2O, and E_{H_2} is the energy of the gas phase H_2.

For reducible oxides, formation energy of oxygen vacancies is low. The ability to form O-vacancies makes the reducible oxides desirable catalysts, since by giving surface oxygens to the reaction they catalyze reactions proceeding via the Mars-van Krevelen mechanism illustrated in figure 5. [8] In this mechanism, CO is oxidized by lattice oxygen producing CO_2. The formed oxygen vacancies are then filled again by gas phase O_2. Alternatively, stable oxygen vacancies can create active sites. As illustrated in figure 5, oxygen vacancy can in some cases lead to electron deficient sites. An example of well-known reducible oxide is ceria (CrO_2), which has multiple catalytic applications such as the steam and dry reforming, and the WGS reaction [61] discussed in section 3.

Irreducible oxides have the opposite behavior. They don't form oxygen vacancies easily and are generally less reactive.[57] Because of this, irreducible oxides are better suited for applications that demand stability and high corrosion resistance. Well known irreducible oxides include SiO_2, alumina (Al_2O_3) and MgO. ZrO_2 is also considered to be an irreducible oxide [59], but it has also been described to have an intermediate character. [56] Reducibility of ZrO_2 is discussed in more detail in section 4.4.1.

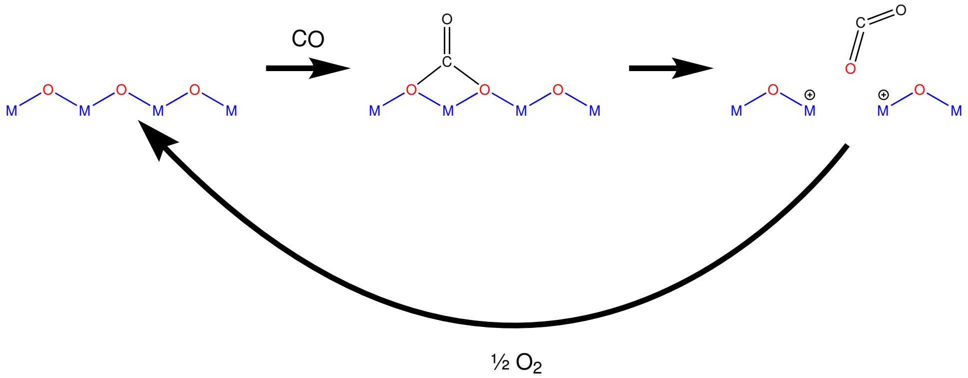

Figure 5: Illustration of Mars-van Krevlen mechanism producing CO_2.

4.1 Acid-base properties

One of the defining properties of a catalyst is its ability to work as a proton donor or an acceptor. This ability is highly related to the acid-base nature of the catalyst, as by Brønsted definition acid is a proton donor and base is a proton acceptor. The Lewis definition generalizes this by defining the electron donor as a base and the electron acceptor as an acid. [62]. Consequently, many chemical reactions between a catalytic surface and an adsorbate are defined by the acid-base properties, since many catalytic reactions involve reduction or oxidation of organic compounds.

Acidity of oxide surfaces is not so straightforward, since acid-base behavior can depend on surface site. One way to measure the acidity of a surface is to use the isoelectric point which is in case of metal oxides defined as a pH of a solution in which the concentrations of ${MOH_2}^+$ and MO^- surface sites are equal. Multiple parameters have been used to predict surface acidity of an oxide, such as formal charge or the size of a cation.[62] On the atomic level, instead of defining surface acidity it is more meaningful to identify individual acidic and basic sites. Many oxides are commonly labelled as bi-functional catalysts since they include both acidic and basic sites. Metal cations are usually Lewis acids, and oxygen anions are Lewis bases.[63]

4.2 Metal oxides in catalysis

The high stability of oxides in harsh reaction conditions makes them attractive materials for industrial applications where the reaction temperatures and pressures can be relatively high. There exists a large range of catalytic applications for oxide materials ranging from inactive support materials to active catalysts. Support materials in catalysis are needed to to prevent the active metal nanoparticles from clumping together and losing their catalytic sites.[8] Especially irreducible oxides are implemented as support materials for catalysts due to their stability and expected inactivity at least for oxidation reactions.

Support materials rarely are just passive bystanders in catalytic processes, and they can have quite a significant role in the chemistry involved. In fact, distinction between the support material and the catalyst can be a bit artificial since support materials are known to affect the chemistry. For example, one study [26] compared the CO_2 methanation reaction on a ZrO_2 and a Al_2O_3-supported Co catalysts, and found higher activity and selectivity towards CH_4 formation for ZrO_2 supported Co. Another example is Pd supported on CeO_2 where the structure of support affected activity of the Pd/CeO_2 catalyst in a CO oxidation reaction. [64]

Some reducible oxides, such as CeO_2, are also known to have a large number of applications as the primary catalyst. Reactions where CeO_2 is considered as a promising catalyst include at least water-gas shift, steam and dry reforming of hydrocarbons and some C–C coupling reactions. [61]. To give also a peek of broader applications than just heterogeneous catalysis, in the field of electrocatalysis transition metal oxides, such as RuO_2 and IrO_2 are known to catalyze the oxygen evolution reaction (OER) in water splitting, and interest for these catalysts is raised by ongoing research for sustainable hydrogen production. [65]

4.3 Modification of oxide catalysts

In section 3, it was briefly mentioned how the thermal stability of CeO_2 can be improved by mixing it with TiO_2. Tuning catalytic properties of materials by modifying their chemical composition or structure is extensively studied, and there exist many methods to modify the behaviour of the bulk catalytic material. For example doping[52, 25, 66], nanostructuring [67, 68] and modification of metal-oxide interaction [57, 60] are all effective methods for tuning the catalytic behaviour of an oxide material. In the case of oxides, altering reducibility is a frequently seen topic in literature. In this section, two different ways of modifying properties, especially the reducibility of an oxide catalyst, are discussed briefly: doping and nanostructuring.

4.3.1 Doping

Doping of material means inducing small amounts of impurities into the bulk material in order to modify catalytic properties. Doping, in the context of metal oxides, can be either cationic or anionic. Cationic doping usually means that some of the metal atoms are replaced with dopant atoms, and anionic that the dopant substitutes a lattice oxygen. Cationic doping is more studied [25] and therefore the examples given here consider mainly cationic doping. Nonetheless, anionic doping has also seen growing interest due to possible applications, especially in photocatalysis.[69]

The effects of doping can be quite complex and unpredictable, but there are certain trends. Dopants can be categorized to low, high, and same valence dopants depending on the valence of dopant atoms compared to bulk oxide. Low-valence dopants can make the doped oxide more reactive and reducible. For example, a computational study has found that the energy of vacancy formation for Y-doped $CeO_2(111)$ is 1.06 eV while energy for the undoped surface is around 3.00 eV. [58] The effect applies also to irreducible oxides, and the same study found that Li-doped MgO(001) lowered the energy of vacancy formation from 6.15 eV (undoped) to 3.15 eV. High valence dopants usually have an opposite effect.[25] The same valence dopants have more complicated behaviour and general rules are hard to establish. [25]

In heterogeneous catalysis, doped oxides have been investigated especially for improved selectivity for certain reactions. For example, Na-doped CeO_2 exhibited high selectivity for glycerol to acetol conversion. [66] A more interesting reaction, in context of this thesis, is Zn doped zirconia, which is shown to be a promising catalyst for isosynthesis [52]. Doped zirconia in isosynthesis is discussed more in section 5.5.

4.3.2 Nanostructuring

Another viable way to change the properties of an oxide catalyst is to alter its surface structure. Surface defects can introduce low coordinated atoms that are usually more reactive than the bulk structure. In practice, this means that the benefit of having the catalyst as nanoparticles is not just increased catalytic surface area, but there can also be significant changes to the properties of a catalyst compared to the bulk material.

Notably, reducibility of metal oxides is affected by surface morphology. Computational results have shown that the energy required of oxygen vacancy formation in CeO_2 is significantly decreased on nanoparticles, however, this effect appears to have a non-linear relation to the size of nanoparticles. [70]. The O-vacancy formation enhancing effect in nanoparticles has also been demonstrated computationally for oxides that are considered to be irreducible, like ZrO_2. DFT calculations have shown that the formation energy of an O-vacancy is influenced by structural properties. While the O-vacancy formation energy for a 3-coodinated oxygen on a tetragonal ZrO_2 (101) surface is 5.97 eV, bi-coordinated oxygens on nanoparticles have significantly lower energies, such as 2.62 eV for a $Zr_{80}O_{160}$ nanoparticle. [71] DFT calculation also demonstrate that nanostructured ZrO_2 has unexpected properties on hydrogen dissociation, essentially exhibiting reducible behavior. [67]

Nanostructuring has also significant effect on the metal-support interactions. Computational studies by Vayssilov *et al.* [68] have demonstrated that oxygen spillover to ceria supported platinum is a process that requires nanostuctured surfaces or nanoparticles. More detailed discussion about this matter will be in section 5.1.1 where hydrogen dissociation on zirconia is delved into.

4.4 Zirconia

After discussing oxides in general, it is now time to take closer look at the most studied isosynthesis catalyst, zirconia.[5, 52] Zirconia is found in three different crystal structures: Monoclinic ($P2_i/c$), tetragonal ($P4_2/nmc$) and cubic (F-m3m). Monoclinic zirconia (m-ZrO_2) is the most common one in nature and it is found as a mineral called baddeleyite [23]. This is the most stable form of zirconia from 0 to 1180 °C, after which tetragonal phase (t-ZrO_2) becomes the stable structure up to

2370 °C, and beyond that, the cubic form (c-ZrO_2) is the stable phase from 2370 °C to the melting point of zirconia at 2600 °C.[23] In addition to these crystalline forms, there is also an amorphous form of zirconia, which has been studied as a possible catalyst for the production of biodiesel.[72]

t-ZrO_2 has each Zr atom coordinated to eight oxygen atoms. In monoclinic zirconia each Zr atom is coordinated to 7 oxygen atoms, and in cubic zirconia each Zr has six oxygen neighbours. [73, 74].

Tetragonal and cubic zirconia can be stabilized at room temperature via doping. Yttria-stabilized zirconia or YSZ is form of cubic or tetragonal zirconia that is stabilized by doping with Y_2O_3. YSZ has many applications that demand hard, heat resistant and durable materials, such as dental crowns [75] and heat resistant coatings.[76]

The crystal structure of zirconia has a significant effect on its properties, and different applications benefit from different structures. For example, monoclinic zirconia has interesting catalytic properties [77] (see section 4.4.2), but the heat resistant coatings benefit from tetragonal and cubic phases that are more stable at higher temperatures. In fact, one of the key properties of YSZ is that the doping prevents the transition from tetragonal to monoclinic phase. This is important since the transition causes material to expand which can ruin the coating [23, 76]

In heterogeneous catalysis, the structure of a catalytic surface is also a highly important factor. The most stable surface depends on the crystal structure. For monoclinic zirconia the most stable surface plane is described by Miller index $\bar{1}11$, and for tetragonal zirconia the most stable surface is 111 [23]. For monoclinic zirconia, TEM measurements have reported at least 111, 001 and 011 surface planes for monoclinic zirconia. [73]

Zirconia is an insulator with an experimentally measured band gap of 5 eV. [55] This insulating nature makes zirconia a less appealing material in typical semiconductor applications such as solar technology, but there is evidence that oxygen-deficient zirconia materials can have a band gap as low as 1.5 eV, making these materials solar light absorbing and opening possible applications also in photocatalysis. [78]

4.4.1 Reducibility of zirconia

Reducibility (or irreducibility) of zirconia is at the center of zirconia chemistry. Despite the irreducible nature of zirconia, there are experimental reports of oxygen vacancies, including evidence of Zr^{3+} cations [79]. Formation of oxygen vacancies is thought to be the reason for some chemistry associated with zirconia. Charge balancing in doped zirconia structures is thought to happen via formation of oxygen vacancies. [55]. It also appears that selectivity in isosynthesis is enhanced by the presence of oxygen vacancies. [5]

DFT calculations have shown that the surface structure has a significant effect on stability of oxygen vacancies. On a m-ZrO_2 $(\bar{1}11)$ surface, the most stable oxygen vacancy according to calculations is a two-fold vacancy, but on $(\bar{1}01)$ surface, a three-fold vacancy is found to be more stable. [59] Reducibility of ZrO_2 can be enhanced by doping, for example, Zn as a dopant for zirconia is shown to promote formation of oxygen vacancies [80]. A Computational study of oxygen vacancy formation on a $(\bar{1}11)$ surface of m-ZrO_2 concluded that the formation energy for a vacancy is high, highlighting the irreducible nature of zirconia. [81] The same study found that similarly to Zn, Ca also enhances formation of vacancies, especially formation of 2-fold O vacancies. This was attributed to charge imbalance caused by Ca^{2+} cations. The larger ionic radius of Ca^{2+} compared to Zr^{4+} leads to local distortion of a lattice. It was also found that doping with Ca stabilizes the surface. Recent DFT studies also suggest that single transition metal atoms on a m-ZrO_2 surface can enhance reducibility. The magnitude of the effect depends on multiple factors, including electronic properties of the metal atom and the adsorption site. Interestingly, the adsorption of a transition metal on two-coordinated lattice oxygens was found to prevent the enhancement of reducibility. [60]

When it comes to the nature of oxygen vacancies, the behaviour of ZrO_2 resembles a highly irreducible MgO, meaning that the excess electrons in oxygen vacancies are trapped to the vacant site. This is not the case, for example, with TiO_2, which distributes electrons to the neighboring cations. [55]

4.4.2 Zirconia in heterogeneous catalysis

Numerous papers discuss zirconia based catalysts, where zirconia is used as a support material for transition metals such as Co[26], Ni[82], Cu[40, 24] and Pt[83]. As discussed above, zirconia makes a great support material for metal catalyst due to high stability and inert behavior in many reactions. However, the distinction between a supporting material and a catalyst can be a bit artificial since the support can sometimes have almost as large a role in catalytic process as the metal component. This is also the case with zirconia and for example, The phase of zirconia support is found to affect performance of the metal domain. Witoon *et al.* [24] found in an experimental study that a Cu/ZrO_2 catalyst had the highest active copper surface area on amorphous and t-ZrO_2, and the larger area was correlated to increased methanol yield from CO_2 hydrogenation. Zirconia has not been applied as a support only for metal catalysts, but also for other oxides. Lu *et al.* have studied ZrO_2 as a support for a Cu-Mn-Ce mixed oxide catalyst (essentially Cu and Mn doped ceria) and found that the ZrO_2 support did not only improve stability but also the catalytic performance of the ceria-based catalyst via enhancing mobility of lattice oxygens. It was surmised that the $Zr_{0.88}Ce_{0.12}O_2$ phase formed at the interface between ZrO_2 and the mixed oxide catalyst played a key-role in the improvement of the performance.

As a catalyst, monoclinic zirconia is especially interesting, not only because of its stability even at relatively high temperatures, but because it incorporates zirconium atoms with differing coordination numbers, which leads to multiple possible active sites. On a monoclinic zirconia surface. there are unsaturated cation Zr^{3+} and Zr^{4+} sites.[73]. There are not many examples of catalytic processes where pure zirconia is among the most promising catalysts, excluding the production of isobutene by hydrogenating CO (isosynthesis). Modified zirconia has been investigated as a potential catalyst for esterification and transesterification reactions [84] Especially sulfated zirconia exhibits promising properties as an acid catalyst. [85]. Another example is Zn doped zirconia that has raised some interest, as it has shown to catalyze isobutene formation from bio-ethanol, with yields as high as 83%. [86]

Zirconia as a supporting material is also found to increase catalytic activity in methanol formation. [87] In_2O_3 is known to catalyze hydrogenation of CO_2 to methanol, and a ZrO_2 support is found to induce significant improvement to catalytic activity compared to unsupported In_2O_3. This behaviour is somewhat unique compared to other support materials like Al_2O_3 or CeO_2 [88]. The reason for this behaviour was attributed to the ability of zirconia to affect the epitaxial growth of In_2O_3, resulting in structures with an abundance of oxygen vacancies.

5 Isosynthesis on zirconia

The role of zirconia in isosynthesis is highlighted throughout this thesis, but details of the reaction mechanisms are kept under a veil up until now. This is because similarly to the FT process isosynthesis involves a complicated network of possible reactions and detailed understanding in some parts is still lacking. Therefore, a satisfactory summary is hard to make.

Starting from details of zirconia catalysts, usually real catalysts consist of multiple phases of zirconia. It has been shown that the phase of ZrO_2 plays an important role in $i-C_4$ selectivity [77]. The highest selectivities for iso-products have been achieved with monoclinic zirconia. [77] In fact, $i-C_4$ selectivity has been shown to increase when the percentage of the monoclinic phase is increased, and almost pure monoclinic ZrO_2 has shown excelled selectivity. [51] Some early studies suggest that an active isosynthesis catalyst should have an equal amount of acidic and basic sites. [5] On the other hand, an experimental study by Su *et al.* [89] found that higher ratio of basic sites leads to increased $i-C_4$ selectivity. Similar results were also obtained by another group [90] which remarked that the increased number of acid sites results in increased activity for linear C_4 hydrocarbon formation.

The mechanism for isosynthesis has mostly been studied experimentally. The current understanding of the mechanism is largely based on studies from 1980s to early 2000s. [91, 92, 93]. Even though the full details are still unknown, there is some agreement on the general mechanism. First, the initiation of chain growth is assumed to happen via CO adsorption, followed by consecutive hydrogenation reactions leading to formyl, formate, formaldehyde and methoxy species (figure 6)[92] For hydrogenation, gas phase hydrogen needs to be activated.

After the initiation, the carbon chain growth likely proceed via CO insertion pro-

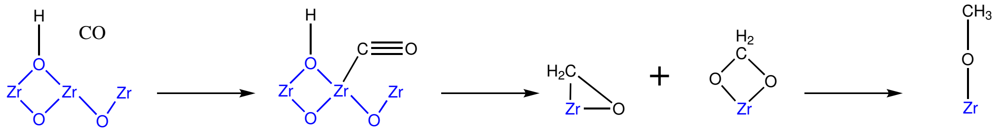

Figure 6: Proposed steps for the initiation of isosynthesis reaction.

ducing C_2 species, after which the longer carbon chains can be formed via aldol condensation or CO insertion. During the next sections, the individual elementary steps will be looked at in more detail, and since zirconia is the catalyst of interest, the mechanism will be discussed only on zirconia.

5.1 Initial phases

5.1.1 Dissociative adsorption of H_2

Zirconia is known to catalyze the dissociative adsorption of water even at low temperatures [94, 73], but reactivity with the gas phase H_2 has been studied less. The fact that zirconia is known to catalyze hydrogenation and dehydrogenation is one indication of possible dissociative adsorption of hydrogen. More direct proof of reactivity with gas phase H_2 is that hydrogen gas atmosphere has been observed to affect the composition of a zirconia catalyst.[79] UV-Vis measurements of a ZrO_2 surface have indicated that hydrogen treatment reduces Zr^{4+} concentration and produces Zr^{3+} cations. [79]

Commonly, transition metals are used for hydrogen activation. Especially Group 10 metals like Pt and Pd are known for their ability to activate hydrogen and catalyze hydrogenation reactions.[95]. H_2 usually dissociates upon adsorption. In contrast CO adsorption is more often associative, meaning that the molecule does not at least immediately dissociate. [8]

On an oxide surface, dissociative adsorption of H_2 can happen in two ways: Homolytically, which means that charge (or more precisely bond forming electrons) are distributed equally between both hydrogen atoms, or heterolytically so that charge is distributed unequally. [67, 96]

An important detail with homolytic and heterolytic dissociation is that heterolytic dissociation does not result in reduction of the surface, since the heterolytic dis-

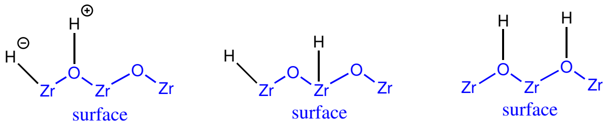

Figure 7: Hydrogen dissociation schemes. From right to left, heterolytic and two homolytic ways for dissociation.

sociation leads to formation of H^- and H^+ species, and charges get balanced. Homolytic dissociation leading to formation of two species with the same charge means that total charge balance of the surface changes and the surface reduces or oxidizes in the process. Consequently the heterolytic dissociation is the dominant mechanism on oxide surfaces where metal-oxygen acid-base pairs are present. Therefore the heterolytic dissociation is also the more likely process on zirconia. [96]

H_2 adsorption on monoclinic ZrO_2 $(\bar{1}11)$ and $(\bar{1}01)$ surfaces has previously been studied computationally by Syzgantseva *et al.*[97] and they found that the molecular H_2 adsorbs on both surfaces with adsorption energy approximately -0.10 eV, and the adsorption is mostly physisorption. For the dissociated H_2, adsorption energy on the $(\bar{1}11)$ surface was found to be around 0.24 eV, and on the $(\bar{1}01)$ surface -0.08 eV, meaning that the adsorption of dissociated hydrogen is endothermic only on the $(\bar{1}01)$ surface. The activation energies for the dissociaton reaction were found to be between 0.28–0.65 eV. The experimental value for the activation energy determined via IR-spectroscopy is around 10 kcal/mol [98] (0.43 eV), but what phase or surface plane this value represents, is unclear.

The effect of the surface structure on dissociative adsorption of H_2 on zirconia has been studied computationally by Puigdollers *et al.*[67], who found that the structure have a significant effect on reactivity even to the point that nanostructured irreducible zirconia could become reducible. They studied dissociation process on facets of multiple different sized nano particles of tetragonal zirconia, as well as periodic (101) and stepped (156) t-ZrO_2 surfaces. It was found that on both (101) and (156) surfaces, only heterolytic splitting was exothermic, but on nanoparticles both heterolytic and homolytic splitting were found to be exothermic. In other words, nanostructuring can make homolytic dissociation a feasible mechanism.

It is also possible that the initial dissociative adsorption is carried out by some active metal component instead of the oxide, after which the dissociated hydrogen migrates to the oxide via the hydrogen spillover mechanism. [99, 100] Figure 8 illustrates this process. On clean metal surfaces, the homolytic pathway is usually the preferred mechanism for the dissociation of H_2. [96]

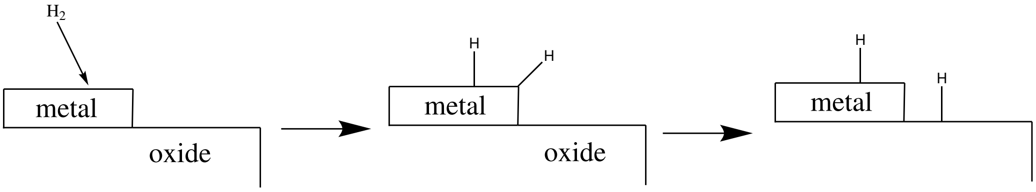

Figure 8: A schematic drawing of hydrogen spillover from metal to oxide.

Hydrogen spillover to irreducible oxides is sometimes considered to be a thermodynamically unfavourable process,[100] and therefore it is likely that on zirconia the oxide itself is solely responsible for the dissociation of H_2.

5.1.2 CO adsorption

Both experimental and computational studies [101, 102, 63] have demonstrated that CO absorbs most likely linearly onto the top sites of Zr atoms via carbon. Experimentally, linear CO adsorption is observed using DRIFTS [101]. A computational study by Kauppinen *et al.* [102] found the adsorption energy of CO on m-ZrO_2 surface to be -0.38 eV, with the Zr–C bond length being 2.60 Å. This bond is quite long, indicating that interaction between CO and ZrO_2 is not particularly strong.

CO adsorption on zirconia with different surface models has previously been studied computationally by Maleki and Pacchioni, [63], who studied monoclinic ZrO_2 with ($\bar{1}11$) and ($\bar{2}12$) surfaces, tetragonal ZrO_2 with (101) and (134) surfaces and zirconia nanoparticles with composition of $Zr_{16}O_{34}$ and $Zr_{40}O_{80}$. On monoclinic zirconia, adsorption energies were quite similar on both ($\bar{1}11$) and ($\bar{2}12$) surfaces, ranging from -0.49 eV to -0.56 eV depending on the surface site. The tetragonal (101) surface has only one kind of 7-coordinated Zr atoms, and CO adsorbed on the top site of these atoms has similar adsorption energy compared to the monoclinic surface (-0.50 eV). On stepped (134) surface there was found to be more variation in energies. The strongest adsorption was found to be slightly more exothermic on tetragonal surface compared to the monoclinic surface, and the weakest adsorption was also slightly less exothermic than on monoclinic surfaces. They also found that the optimal structures for CO binding on the $(\bar{2}12)$ surface is on the top sites of step Zr atoms, but the stepped structures didn't seem to have large effect on CO adsorption.

5.2 CO hydrogenation and reaction intermediates

CO hydrogenation is at the center of isosynthesis. The first hydrogenation of CO produces formyl, a HCO species. Hydrogenating formyl produces formaldehyde, and hydrogenation of formaldehyde gives a methoxy group. How these species are bound to the zirconia complicates the discussion about different surface species. For example, formyl can be bound to Zr via only its carbon atom, or it can bound via carbon and oxygen forming η^2-formyl. The same applies also for other species, like formdehyde, which can be present as η^2-formaldehyde. [92] Lattice oxygens could also participate and form surface species that resemble a formate.

5.2.1 Formate formation

Multiple articles [103, 104, 105, 101] considering methanol, CO and CO_2 reduction on zirconia based catalysts have reported formate species on the surface, and CO adsorption as a formate has been found to be likely, meaning that the formyl species given by the first hydrogenation are likely present as formates. Furthermore, there are little computational studies concerning formyl formation on zirconia, but some studies regarding formates on zirconia exist. Kouva *et al.* [101] have studied specifically water and carbon oxides on zirconia, including formate formation, and Kauppinen *et al.* [102] have studied formate formation in the context water-gas shift reaction. These studies assume formate formation to proceed through surface hydroxyls that are present especially in the WGS reaction due to dissociation of water. Even some earlier studies [106] have reported that mono-coordinated hydroxyl groups play an important role on formate formation. However, the mechanism in isosynthesis could be different, since mono-coordinated hydroxyl groups are not necessarily present in similar quantities in isosynthesis.

Formate can be present in two configurations, either as a monodentate in which other formate oxygen is not bonded to the zirconia surface, or bidentate where both oxygens are attached to the surface. DFT calculations for adsorption of formate has been conducted as early as 2008 by Korhonen *et al.* [107], concluding that bidentate was found to be the more stable structure. Figure 9 illustrates different ways how formate can be adsorbed on zirconia. The chelating bidentate structure is interesting also because it could be formed with a lattice oxygen.

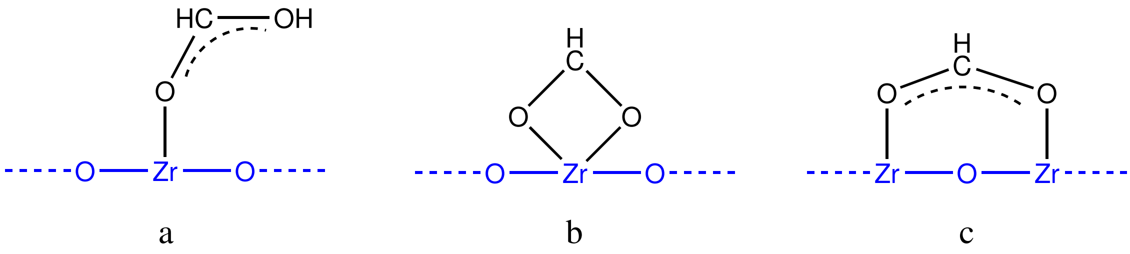

Figure 9: A schematic drawing for adsorption of formate as a) monodentate, b) chelating bidentate c) bridging bidentate.

5.2.2 Formaldehyde and methoxy formation

Consecutive hydrogenation of CO leads to the formation of formaldehyde and methoxy species. There are very few detailed mechanistic studies about the formation of these species, and for example it is unknown if all hydrogenation steps take place at the same active site. Therefore these hydrogenation reactions take an important portion of the computational part of this thesis.

The role of methoxy species in isosynthesis on zirconia have been studied by Maruya *et al.* [92] who proposed a mechanism in which a formate species is first reduced to methoxy, which then gives hydrogen back to surface, forming essentially CH_2 attached to one of the lattice oxygens. They concluded that the methoxy species is an important reaction intermediate in isosynthesis.

Study by Ouyang *et al.* [108] investigated the migration of methoxy groups from bridged structure to terminal site (figure 10) and found that the C–O bond of a methoxy group is not broken during this process.

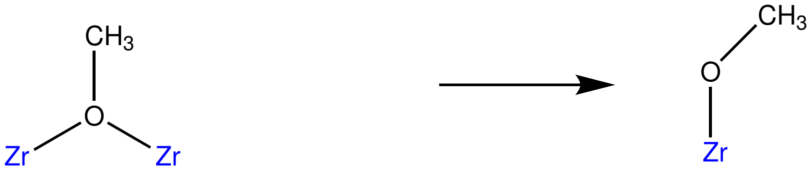

Figure 10: A schematic drawing representing methoxy migration from the bridged to the terminal site.

5.3 Chain growth and branching mechanism

After initiation, there are two suggested routes for carbon chain growth. First, the CO insertion which produces linear carbon chains. This is also one of the mechanisms argued to take place in FT-synthesis. The second mechanism involves aldol condensation, which could be responsible for the branching in the chain propagation.

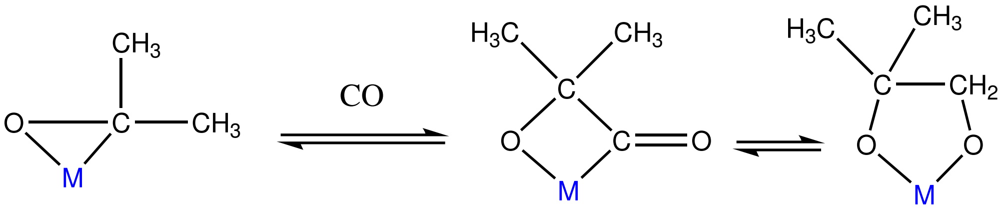

Figure 11: One proposed [92] mechanism for branched chain growth via CO insertion.

Maruya *et al.* [92] showed with ^{13}C NMR measurements that the central carbon of i$-$C$_4$ products come from the methoxide species, and other carbons are given by the gas phase CO. This would point to the mechanism shown in the figure 11, where the gaseous CO is inserted to the central carbon.

5.4 Formation of side products

In section 3.3.1, it was stated that side products in isosynthesis include mostly smaller hydrocarbons like C_1,C_2 and C_3 species, along with the CO_2, which is the most abundant side product. The mechanisms governing the formation hydrocarbon side products is unknown, but there exist some studies on adsorption and formation of CO_2[101, 109, 110]. This subject is discussed in more detail in section

5.4.1.

The formation of alcohols, especially methanol, is another possible unwanted side reaction that takes place on zirconia during isosynthesis. Zirconia is not really known for catalyzing methanol formation from syngas in large quantities; however, some amount of methanol is produced [111] Since oxygenated species are assumed to be reaction intermediates in the production of $i-C_4$ species, understanding alcohol formation is something that shouldn't be overlooked, but for now it is only briefly discussed. An early mechanistic study by He and Ekerdt [111] named two possible ways of syngas methanol synthesis on a ZrO_2 catalyst. These are hydrolysis of surface methoxide at lower temperatures (125 °C) and hydrogenolysis of more complex methyl-formate species at higher temperatures (580 °C – 610 °C). The latter would be the more likely scenario in isosynthesis due to the harsh reaction conditions and absence of water.

5.4.1 CO_2 formation

As discussed above, CO_2 formation in isosynthesis is a major problem, and understanding of the process is still lacking. One possible mechanism could be similar to the Mars-Van Krevelen mechanism, like the one associated with the WGS reaction. Absence of water in reaction suggest otherwise, but the presence of terminal hydroxyl groups could work similarly as in the WGS reaction. Yurkiv *et al.* [112] have studied CO oxidation on oxygen-enriched YSZ surface, and they found that an Eley-Rideal-type mechanism in which gas phase CO binds straight onto a lattice oxygen forming CO_2 is feasible. However, since forming oxygen vacancies on undoped zirconia is difficult, this mechanism might not be generalizable. It should also be noted that formate formation and CO_2 formation are closely related. It is found that when heated, CO adsorbed as bicarbonate or carbonate will release CO_2, but CO adsorbed as formate releases CO. [110]

Similarly to the formate adsorption, CO_2 adsorption models have been described in literature as mono-, bi- and tridentate. Study by Bachiller-Baeza *et al.* [109] concluded that CO_2 adsorption results in hydrogen carbonates, monodentate and bidentate carbonates. Similarly to other discussed surface species, it seems that these definitions can be quite ambiguous, and therefore it might be better to describe the adsorbed species as physisorbed CO_2 or chemisorbed ${CO_3}^{2-}$ species.

[113]

CO_2 adsorption seems to be dependent on the phase of zirconia. Experimental results have shown that monoclinic zirconia has a much higher adsorption capacity for CO_2 compared to the tetragonal phase [110]. Interestingly, at the first glance it seems that tetragonal zirconia produces less CO_2 compared to monoclinic zirconia; for example, the catalyst with tetragonal nature in table 14 (m-ZrO_2-Ref) has the lowest selectivity towards CO_2. The increased $i-C_4$ selectivity when CO_2 is added to the reactant stream mentioned in section 3.3.1, suggests that the CO_2 production is coupled in some unexpected way to the $i-C_4$ production.

5.5 Modified zirconia in isosyntheis

There are some studies concerning isosynthesis on modified zirconia surfaces. Already in section 5.1.1, the effects of nanostructructuring on hydrogen dissociation were discussed, and in section 4.3.1, Zn-doped ZrO_2 was mentioned to be a promising isosynthesis catalyst. The usefulness of Zn/ZrO_2 in isosynthesis is also hinted at by its ability to produce isobutene from ethanol as mentioned in section 4.4.2. Indeed, Zn-doped ZrO_2 has been found to exhibit improved selectivity towards isobutene. [52]. A computational study on Zn-doped ZrO_2 conducted by Mancera *et al.* [80] suggests that doping ZrO_2 with Zn promotes formation of oxygen vacancies, and increases both basicity and acidity of certain surface sites, while the total number of basic sites is increased. Zn-doped zirconia has also been used by Liu *et al.* [114] as a catalyst for the dehydrogenation of isobutane to isobutene, and their CO_2-TPD study concluded that Zn has an ability to neutralize strong Zr^{4+} $-O^{2-}$ acid pairs while generating new $Zr^{4+}-V_O$ and $Zr^{2+}-O^{2-}$ pairs, which reduces the surface acidity of ZrO_2. These results concerning acid-base properties of Zn-doped catalysts are in line with the earlier studies [89, 90] which have concluded that increased ratio of basic sites increases the $i-C_4$ selectivity.

The role of oxygen vacancies in isosynthesis is still unknown. From early on, there has been discussion that oxygen vacancies are required for active isosynthesis catalyst, and dopants that introduce O-vacancies and are similar in size to zirconium have been experimentally proven to be the most active.[5] On the other hand, zirconia is an irreducible oxide, and the energy needed for creating oxygen vacancies is relatively high. Then again, the reaction conditions for isosynthesis are quite rough, which could make the formation of oxygen vacancies feasible even for undoped zirconia.

6 Computational details

While zirconia is a somewhat studied material, previous computational studies on the full isosynthesis reaction network are still scarce. Therefore, in this thesis, isosynthesis catalyzed by zirconia is studied via computational methods. The DFT calculations conducted in this study are based on the important elementary steps discussed in section 5. The studied steps include syngas adsorption followed by heterolytic dissociation of H_2. After this, the hydrogenation of CO is studied all the way to the formation of OCH_3-species. Reaction network is expanded to CH_2 formation via C–O bond breaking and finally C–C bond formation via CO insertion is investigated. Figure 12 shows a schematic map of the reaction network that was considered.

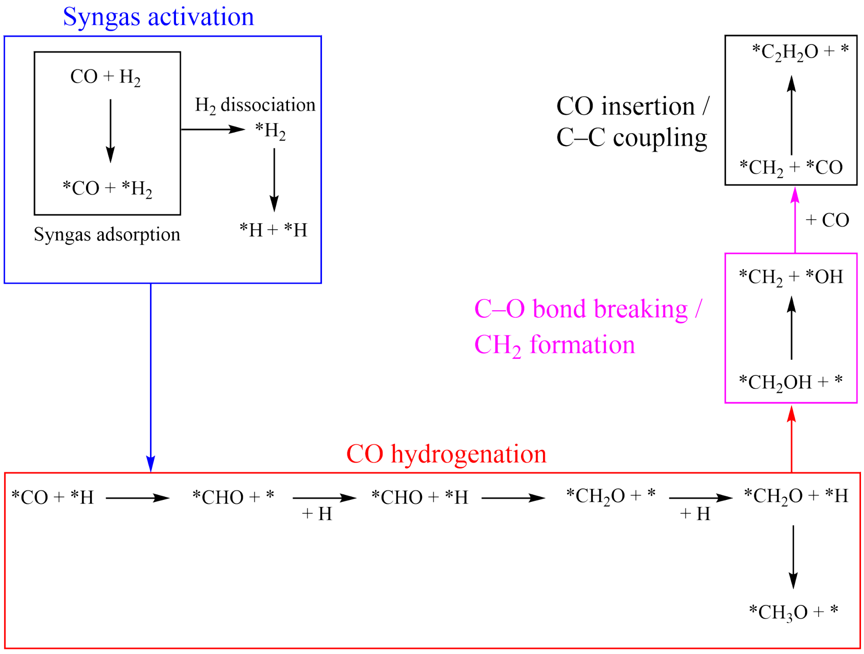

Figure 12: Schematic map of studied reaction network. Asterisks represent surface site.

The calculations started by building and optimizing a reasonable m-ZrO_2 surface structure, and from there the adsorption of H_2 and CO was probed, after which the reactions shown in the figure 12 were studied. In contrast to the earlier computational studies of zirconia chemistry, such as calculations by Kouva *et al.* ,[101] in this DFT study, the presence of terminal hydroxyls was omitted from the beginning. As discussed in section 5.2.1, surface hydroxyls can play an important role in formate formation, but in the absence of water, hydroxyl groups can't form via dissociation of H_2O. Instead, formation of these hydroxyls groups during the investigated reactions was studied. Table 2 lists the studied elementary steps with labels that are used throughout the text. Labels starting with h describe hydrogenation reactions, in other words reactions where a C–H bond is formed. Label r is used to distinguish reactions where an O–H bond is formed, label d describes dissociation reactions and i is for CO-insertion.

Table 2: Studied elementary steps.

label	**description**	**reaction**
dh	H_2 heterolytic dissociation	$H_2 \longrightarrow H^+ + H^-$
h1	hydrogenation	$CO + H \longrightarrow HCO$
h2	hydrogenation	$HCO + H \longrightarrow H_2CO$
h3	hydrogenation	$H_2CO + H \longrightarrow H_3CO$
r1	reduction	$H_2CO + H \longrightarrow H_2COH$
d1	dissociation	$H_2COH \longrightarrow H_2C + OH$
i1	C–C coupling	$H_2C + CO \longrightarrow H_2C_2O$

6.1 Computational methods

For all DFT calculations, the Python-based open source software package GPAW was used.[115, 116, 117]. The Kohn-Sham equations were solved with the PBE-functional [118] in real space using finite the difference-method. The k-point sampling in reciprocal coordinates was (4,4,1). The calculations were periodic only in x- and y-directions, except for the ab initio MD simulations for which full periodicity was implemented. A vdW-correction for the system was done using the correction scheme by Tkatchenko and Scheffler. [119]

To compensate the overdelocalization of electron density in DFT, discussed in section 2.1.2, the Hubbard U-correction was implemented for the zirconium d-bands. The U value was set to be 1.9 eV. The commonly used value for the U parameter for zirconia is around 4 eV,[71] but this precise value was found from a previous study.[60] An example of GPAW structure optimization script is shown in appendix 1. To speed up the calculations, the density mixing scheme shown in appendix 1 was used.

All the structures were initialized using the graphical interface of Atomic Simulation Environment (ASE)[117]. Some structure images, such as those shown in figure 14, were rendered using Avogadro software.[120] Building a surface model for the stepped m-ZrO_2 surface proved to more difficult than anticipated. The surface model is discussed in more detail in section 6.2, but an important detail about the model is that the periodic cell is slightly slanted and this induced a peculiar problem for the automatic definition of the grid points from defined grids spacing. Therefore, the grid points had to be manually determined for x, y and z directions. The grid points used for all the geometry optimizations in the(x,y,z) format are (60,32,156) for the cell, to give effectively 0.2 Å grid spacing. For the static DFT calculations, approximately 10 Å of vacuum is set below and above the surface slab.

Adsorption energies were calculated according to equation 10. More precisely, the used formula was

$$E_{\mathrm{ads}} = E_{(\mathrm{x}\,+\,\mathrm{m\text{-}ZrO_2})} - E_{\mathrm{x}}(g) - E_{(\mathrm{m\text{-}ZrO_2})}. \tag{17}$$

NEB was the main tool to find potential transition states for surface reactions. To perform an NEB calculation, an initial and a final state are first needed. An initial state can be, for example, some molecule adsorbed on the surface, and a final state the same molecule dissociated on the surface. For an NEB calculation path from initial to final state is interpolated, commonly using linear interpolation between the states. The interpolated path consist of a number of intermediate structures called images. Increasing the number of images makes the NEB algorithm usually more successful in finding the transition state, but this also increases the computational cost. Therefore, it is encouraged to try to minimize the number of images needed. With the interpolated path, the NEB algorithm is carried out. Depending on the size of the system, these calculations can take anything from 20 minutes to several days. The ideal result would be that the algorithm finds a single structure between the initial and the final state that doesn't have any forces driving the structure in any direction on the path.

Climbing image NEB is a modification of this method, and is used to drive one image as close to the saddle point on the minimum energy path as possible.[121] Usually, the calculations are started by regular NEB, and after sufficient convergence, the climbing image is switched on. In this study, regular NEB is done until the maximum forces (parameter fmax in script 3) are below 0.15 eV/Å. After this, the climbing image NEB is switched on and the convergence limit is set to 0.05 eV/Å. For NEB calculations, path interpolation was done with the script given in appendix 2. The NEB calculation was performed using the script in appendix 3.

To confirm that the minimum energy path saddle point found with the NEB method is the true transition state for the wanted reaction, a vibrational analysis is performed. The normal modes and natural frequencies are computed for the found structure (or for the part of it that is relevant). If the frequency of normal mode that is associated to the given reactions is imaginary, the structure is the transition state. In the ideal case, there should be only one normal mode with an imaginary frequency.

6.2 The m-ZrO_2 model

6.2.1 The bulk structure

The lattice parameters used for constructing bulk m-ZrO_2 were obtained from calculations by Korpelin *et al.*[60] The unit cell of the m-ZrO_2 structure defined by these cell parameters is shown in figure 13. These parameters were, however, calculated without any dispersion correction, so to see how dispersion affects the lattice parameters a somewhat experimental optimization was performed with the Nelder-Mead [122] algorithm. The result of this optimization is given on table 3.

The optimization of lattice parameters was done more as a curiosity using an experimental method, and it was performed simultaneously with all the other calculations. Therefore the bulk structure used for the m-$ZrO_2(\bar{2}12)$ surface was defined by parameters from the literature[60]. Table 3 shows that the lattice parameters obtained via Nelder-Mead optimization were different than the values

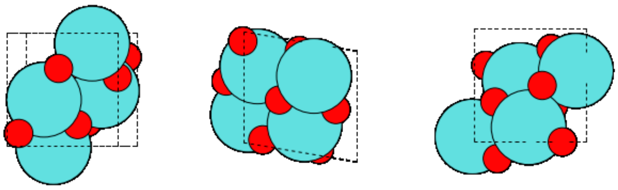

Figure 13: The bulk m-ZrO_2 cell from the x, y and z direction. Color coding: cyan = Zr, red = O.

Table 3: Lattice parameters for m-ZrO_2 calculated with the Nelder-Mead algorithm, and previous results from literature.

parameter	a	b	c	β
Nelder-Mead	5.243	5.211	5.415	100.5
Korpelin *et al.* [60]	5.197	5.263	5.365	99.6

found from the literature.

6.2.2 Surfaces

Some calculations were performed on a flat, m-$ZrO_2(\bar{1}11)$ surface (figure 14). However, interactions between the surface and H_2 proved to be so weak that the focus was almost immediately changed to a stepped structure. The philosophy behind this choice is that the stepped surface would model an step-like defect on a catalytic nanoparticle, while m-$ZrO_2(\bar{1}11)$ would correspond to a flat facet. As discussed in the earlier sections, nanostructuring can play an important role in isosynthesis, especially considering hydrogen activation, and therefore this kind of stepped structure is especially interesting.

The stepped surface was defined by Miller index $(\bar{2}12)$ and it was constructed via slicing the bulk structure. The plane orientation given by the Miller index, however, is insufficient to define how a surface terminates, because complex oxides can give different kinds of terminations depending from where the bulk structure is sliced. The termination is therefore fixed using stability criteria. [62] Slicing can also result in a non-stoichiometric structure, and for the final structures, some manual modifications had to be made to ensure a stoichiometric surfaces. In these calculations, the termination of the $(\bar{2}12)$ surface was decided by using a similar

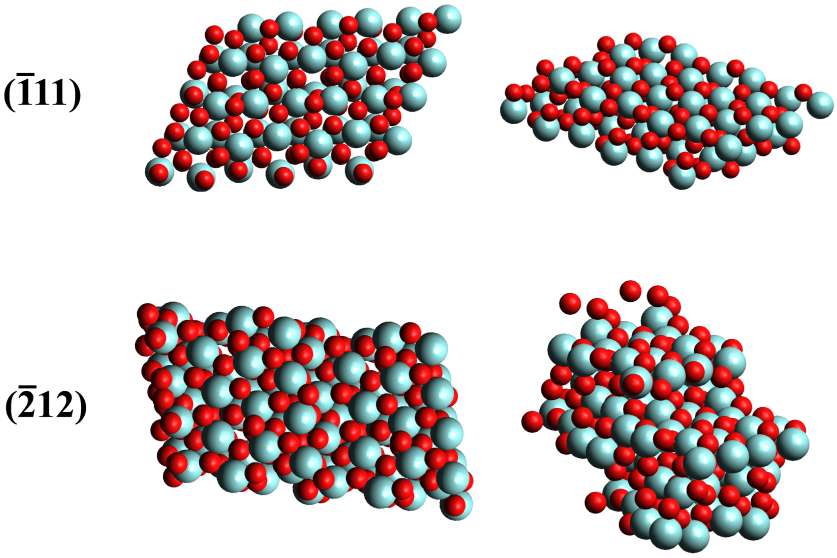

Figure 14: Optimized m-ZrO$_2$($\bar{1}11$) and m-ZrO$_2$($\bar{2}12$) surfaces. On left, surfaces from top, and on right, surfaces from an angled view.

($\bar{2}12$) surface from an earlier study [63] as a reference. Figure 16 shows the final optimized m-ZrO$_2$($\bar{2}12$) surface cell, which is repeated in figure 14 to better depict the structure of the periodic surface slab. The same figure also shows the difference between the used ($\bar{1}11$) and ($\bar{2}12$) surface structures. The stepped ($\bar{2}12$) surface has four Zr atoms wide repeating terraces which have a structure resembling the ($\bar{1}11$) surface. The step has 6-coordinated Zr atoms that are connected via bi-coordinated and tri-coordinated oxygen atoms. Figure 15 gives the up-close of the step.

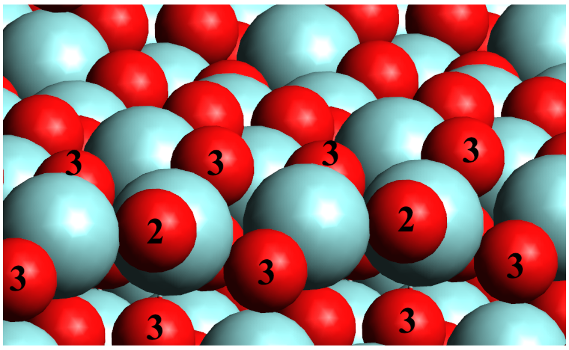

Figure 15: The step of the m-ZrO$_2$($\bar{2}12$) surface model. Numbers remark the coordination of oxygens.

In the optimized ($\bar{2}12$) surface structure, there are both 6- and 7 coordinated

Zr atoms. Since bulk m-ZrO_2 has only 7 coordinated Zr atoms, 6-coordinated surface atoms are undercoordinated compared to the bulk structure. Step sites are typically less coordinated, which causes them to be chemically more interesting, but with the ($\bar{2}12$) model it is unclear whether the steps can be described as low-coordinated sites, since 6-coordinated Zr atoms are also found on a terrace and on the flat ($\bar{1}11$) surface.

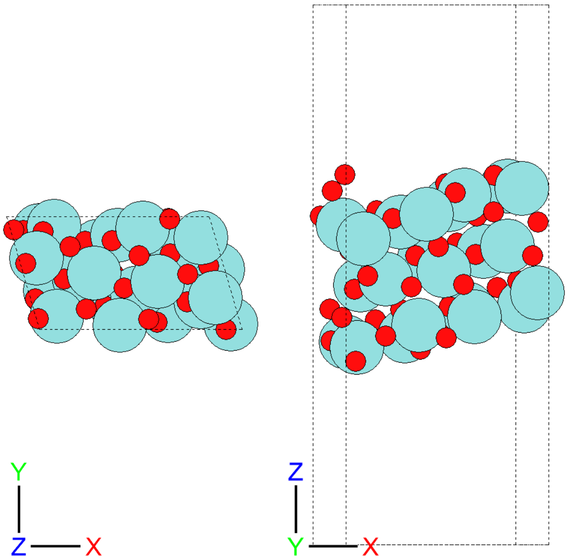

Figure 16: Optimized m-ZrO_2($\bar{2}12$) cell from x, y and z directions as seen on the ASE graphical interface. Cell boundaries are represented by dashed lines.

6.2.3 Thickness of the surface

Influence of the slab thickness on the adsorption energy of H_2 was briefly investigated by using the four structures shown in figure 17. The structures were created so that the top layer for each slab was identical, but the number of layers below the top layer was increased. Defining the thickness of a slab for a ($\bar{2}12$) surface turned out to be difficult, since depending on where the bulk structure was cut, the resulting structure terminated in differing ways. This can be seen by comparing the bottom layer of the structures in figure 17.

Considerable differences in adsorption energies were observed (table 4), and this complicates the interpretation of all calculations. Due to the effect seen in the table 4, it should be emphasized that the DFT results with the slab model shown

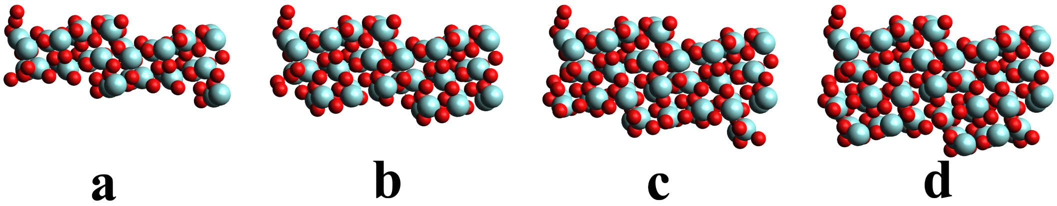

Figure 17: The side view of m-$ZrO_2(\bar{2}12)$ slabs with different thickness.

Table 4: H_2 adsorption energies and average time for a single SCF calculation in the structure optimization cycle

label	E_{ads} [eV]	time [min]
a	-0.255184	4.3
b	-0.875574	5.5
c	-0.47891	6.9
d	-1.16851	8.9

in figure 14 might be applicable only for thin slabs, and thicker slab would influence at least the adsorption energies. However, including more layers to the model would significantly increase the computational cost and therefore would not have been practical. The increase in computational cost can be seen from table 4, where the average times for a single SCF calculation are shown.

7 DFT results

7.1 Syngas adsorption

In this section, results concerning adsorption of CO and H_2 are discussed. Adsorption of CO is assumed to be associative and barrierless. Therefore CO adsorption is mainly studied by calculating adsorption energies for CO on different surface sites. For H_2 adsorption, both dissociative and the associative adsorption are studied, and the dissociation process is investigated via NEB calculations.

7.1.1 Dissociative adsorption of H_2

Associative adsorption of H_2 was first investigated on the flat m-$ZrO_2(\bar{1}11)$ surface, and according to the results, no meaningful bonding between surface and H_2 is present. The lowest energy structure has a distance a of 2.539 Å between the surface and H_2. The adsorption is slightly exothermic, and adsorption energies range from -0.09 eV to -0.19 eV. The best adsorption site for H_2 appears to be the top site of a Zr atom. The dissociated structure was not investigated on m-$ZrO_2(\bar{1}11)$, and instead focus was changed entirely to the m-ZrO_2 $(\bar{2}12)$ surface.

On the m-ZrO_2 $(\bar{2}12)$ surface, the adsorption of both H_2 molecule and dissociated hydrogen were studied. The adsorption of molecular H_2 was found to be mostly similar to the adsorption observed on the $(\bar{1}11)$ surface. The calculated adsorption energies range from -0.07 eV to -0.31 eV, and the most exothermic adsorption energies are observed on the top sites of zirconium atoms located on the step edge. The distance between the surface Zr and H_2 for this structure is 2.478 Å. The difference to the results on the $(\bar{1}11)$ surface is small, but the $(\bar{2}12)$ surface structure seems to slightly enhance adsorption of molecular H_2, and it seems that adsorption of molecular H_2 on zirconia is weak and mostly physisorption.

For dissociative adsorption, the energies calculated with respect to the gas phase H_2 reference range from endothermic 0.38 eV to exothermic -0.55 eV. Interestingly, adsorption sites for the most endothermic and the most exothermic sites are surprisingly similar. In both cases the dissociation is heterolytic, but the endothermic adsorption structure has hydrogen on tri-coordinated oxygen, while in the exothermic structure, one hydrogen is bound to a bi-coordinated oxygen. These structures can be seen in figure 18.

The main conclusion from these results is that the best adsorption geometries for dissociated H_2 supports the heterolytic dissociation. The results suggest that the used surface model behaves as expected and does not exhibit some more exotic reducible character seen with nano structures, where homolytic dissociation becomes the preferred dissociation mechanism (see section 5.1.1). Secondly, the most endothermic structure found also featured heterolytic dissociation, but tri-coordinated oxygens seem to be extremely unfavorable adsorption sites for the atomic H.

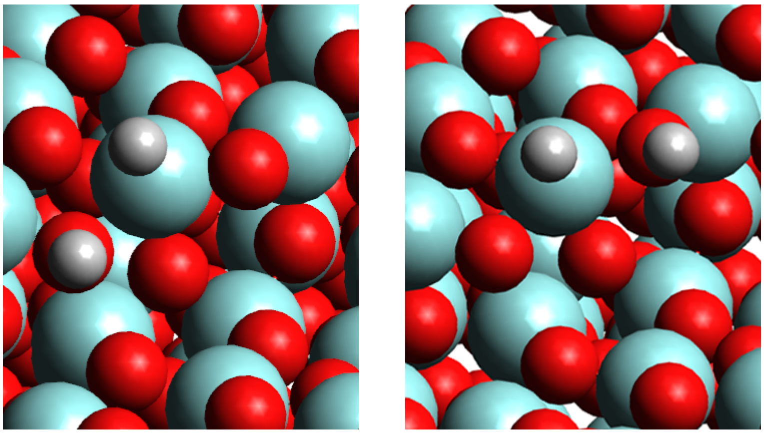

Figure 18: On the left, the structure with endothermic adsorption energy of 0.38 eV and on the right, the geometry with exothermic adsorption energy -0.55 eV. Adsorption energies are calculated with respect to gas phase H_2. Hydrogen is colored in white, otherwise color coding is the same as in figure 15.

Using the most stable adsorption structures as an initial and a final state for a dissociation reaction, an NEB calculation was performed to find the reaction barrier and transition state for the heterolytic dissociation at the step edge. The activation energy was found to be 0.387 eV, which is in line with the earlier discussion in section 5.1.1. The initial and the final state with the found transition state are shown in figure 19. The figure shows also the first example of an NEB-plot. The NEB-plot of H_2 dissociation is a good example since this is a relatively simple reaction and resulting NEB-plot is close to an ideal plot with just a single clear peak.

The most prominent result of these calculations is that hydrogen dissociation appears to be possible even on the undoped zirconia surface. Hydrogen adsorbs very weakly on zirconia, but the $(\bar{2}12)$ surface structure enhanced the binding of molecular H_2, and it might be the case that only these kinds of structures can provide active sites for H_2 dissociation. As discussed in section 5.1.1, the similar calculations conducted by Syzgantseva *et al.*[97] for m-ZrO_2 surfaces gave activation barriers between 0.28–0.65 eV. Therefore the determined 0.387 eV barrier for the heterolytic dissociation of H_2 on the stepped $(\bar{2}12)$ surface is in line with the earlier literature. However, Syzgantseva *et al.* found that the reaction energies on the $(\bar{1}11)$ and the $(\bar{1}01)$ surfaces are endothermic. The exothermic dissociation on the $(\bar{2}12)$ surface suggests that the step defects promote the H_2 dissociation.

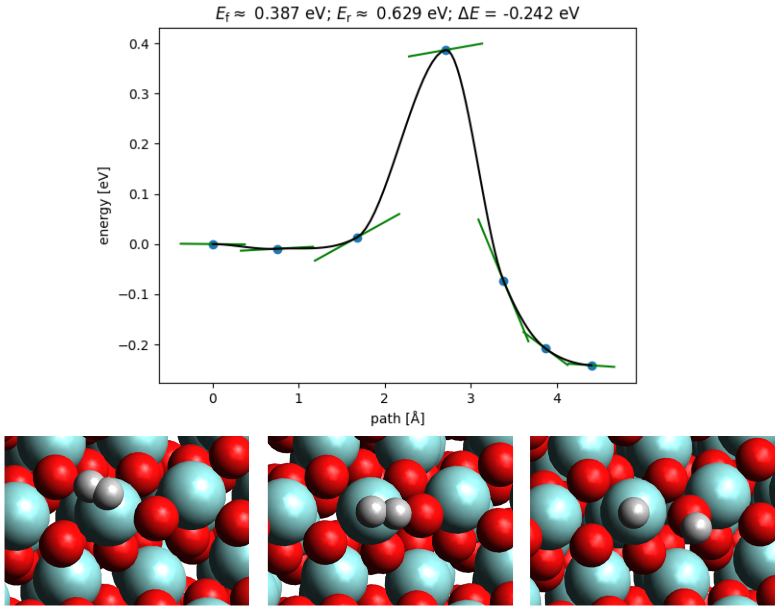

Figure 19: Heterolytic dissociation of H_2 with NEB plot. Structures from left to right are the initial state, transition state and final state for the reaction. In the NEB plot, the initial state corresponds to the leftmost dot on the graph, the transition state is the dot on top of the graph with almost horizontal tangent, and the final state is the rightmost dot. Each dot corresponds to an image used in the NEB calculation.

7.1.2 Adsorption of CO

As with the hydrogen, the adsorption of CO on the flat m-$ZrO_2(\bar{1}11)$ surface was investigated briefly, and the most stable found structure on this surface has an adsorption energy of -0.487 eV. On the $(\bar{2}12)$ surface, CO adsorption was investigated with and without coadsorbed hydrogen. Without coadsorbed hydrogen, the most stable adsorption geometry has an adsorption energy of -0.737 eV, and this structure is located on the terrace. The most exothermic adsorption energy on the step is extremely similar, -0.734 eV. For most of the tested structures, adsorption energies range between -0.20 eV and -0.74 eV. The most stable structures found showed that CO adsorbs linearly (figure 20) to the top sites of Zr atoms. This linear adsorption geometry is reported also by previous studies. [105]. In the linear CO adsorption the distance between a surface Zr and carbon is around 2.56 Å for step Zr and 2.55 Å for terrace Zr. In other words, the strength of adsorption on these two sites is practically identical.

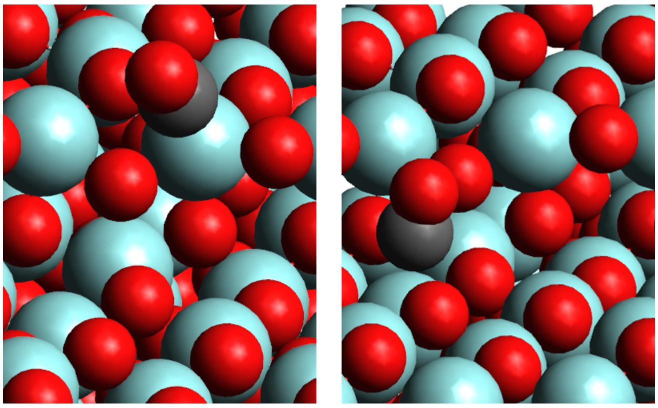

Figure 20: The most stable adsorption geometries of CO on step (left) and terrace (right) sites. Color code of carbon is black. Otherwise colors are the same as in other figures.

In more exotic adsorption structures, CO is bridged between Zr and the lattice oxygen, essentially forming CO_2. These structures share resemblance with the formate-like structures found to be the most stable adsorption geometries for formyl species (More about HCO in section 7.2.1), and therefore adsorption of CO was tested in a similar configuration. These structures, shown in figure 21, were found to be less stable than the linear structures, with adsorption energies of -0.16 eV on step Zr and +0.06 eV on terrace site.

To summarize the results, the adsorption energy of linearly adsorbed CO seems to be similar on all Zr-top sites. When comparing the adsorption on terrace to the adsorption on step, no clear difference was observed. The observation that the step don't have a significant effect on CO adsorption is also in line with the results of Maleki and Pacchioni [63] discussed in section 5.1.2. It is interesting to note that according to the results for CO and H_2 adsorption, the most significant effect of this step defect is its ability to dissociate H_2.

7.2 CO hydrogenation

7.2.1 First hydrogenation

Formyl species resulting from the first hydrogenation (reaction h1) were identified to be quite unstable. The most stable adsorption structure identified for HCO is

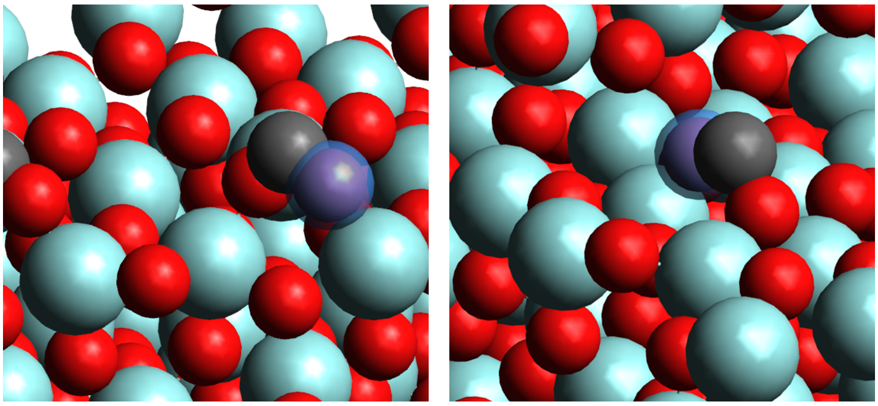

Figure 21: Unstable bridged CO_2-like adsorption structures for CO. On the left side, adsorption on terrace (-0.16 eV), and on the right side, adsorption on step Zr (0.06 eV). CO oxygen is highlighted with a blue color to distinguish it from the lattice.

one where the species is bound on a step zirconium. The adsorption energy for this structure is -1.687 eV. The second best structure with an adsorption energy of -1.628 eV was found for a structure in which carbon is bridged between lattice oxygen and formyl oxygen, forming a bidentate, formate-like structure similar to the CO_2 stucture shown in figure 21. This is an interesting structure, since multiple articles [103, 104, 105, 101] considering methanol, CO and CO_2 reduction on zirconia-based catalysts have reported formate species on zirconia surfaces, and this structure with the lattice oxygen involved resembles a formate. Adsorption of CO to the bridged, formate-like configuration is less stable than linearly adsorbed CO, as discussed in section 7.1.2. Therefore, it seems likely that CO first adsorbs linearly, and forms a bridged structure after the hydrogenation. Consequently, this provides a mechanism for the formate formation in which the surfaces hydroxyls are not needed.

Hydrogen atoms were assumed to diffuse on the surface, so that the H_2 dissociation on the step could also spread hydrogen atoms to the terrace sites. Hydrogen atoms on Zr-top sites were found to promote the hydrogenation better than the lattcie OH groups. For the finals tate of reaction h1, a feasible geometry where formyl is linearly adsorbed to Zr was identified (figure 22). This structure is an intermediate than can transform to a more stable formate structure (figure 22, initial state of reaction h2). The NEB calculation for reaction h1 was performed with a linearly adsorbed CO as the initial state, and the linearly adsorbed HCO intermediate shown in figure 22 as the final state. The activation energy for the reaction h1 was found to be 0.324 eV, which is slightly less that the activation energy of H_2 dissociation. The reaction energy for the reaction h1 is -0.576 eV.

7.2.2 Formaldehyde and methoxy formation

The second CO hydrogenation (reaction h2) step leads to formaldehyde. The best formaldehyde adsorption geometry is almost identical to the formate-resembling structure for HCO, and this has the adsorption energy of -2.375 eV. Therefore, for the second hydrogenation, the considered reaction is from formate to this structure (figure 22, reaction h2). In the structures for reaction h2 in figure 22, C has initially 2.7 Å distance to Zr atom, and in final state 2.9 Å distance to the Zr atom. The reaction h2 was found to have an almost negligible barrier of 0.09 eV. Reaction was also thermodynamically favorable, with the reaction energy of -0.763 eV.

The third hydrogenation in the sequence (reaction h3), the hydrogenation of formaldehyde, produces methoxy species. The final state of reaction h2 was found to be an unsuitable initial state for reaction h3, since the only stable adsorption geometry for methoxy was found to be linear (see the final state of reaction h3). A linear adsorption geometry for formaldehyde has an adsorption energy of -1.953 eV, and this was used as the initial state of reaction h3.

For the methoxy, linearly adsorbed OCH_3, like the terminal methoxy depicted in figure 10, was found to be the only viable structure for OCH_3 adsorption. Formation of methoxy from linearly adsorbed OCH_2 was investigated via NEB calculations and methoxy formation was found to be highly favorable, without any clear barrier and reaction energy of -2.090 eV. Reaction h3 in Figure 22 shows how the transition state for this reaction has formaldehyde bent closer to H atom on surface.

One interesting mechanistic detail is that both methoxy and linear formaldehyde are bound to the surface via O-Zr bond, meaning that because CO and formyl are bound from carbon, the CH_nO stucture has to flip during the methoxy formation. Flipping of the structure could happen through the formate-like h2 final state, and this kind of mechanism is discussed in the next section.

These calculations give some insights to the hydrogenation reactions, highlighting

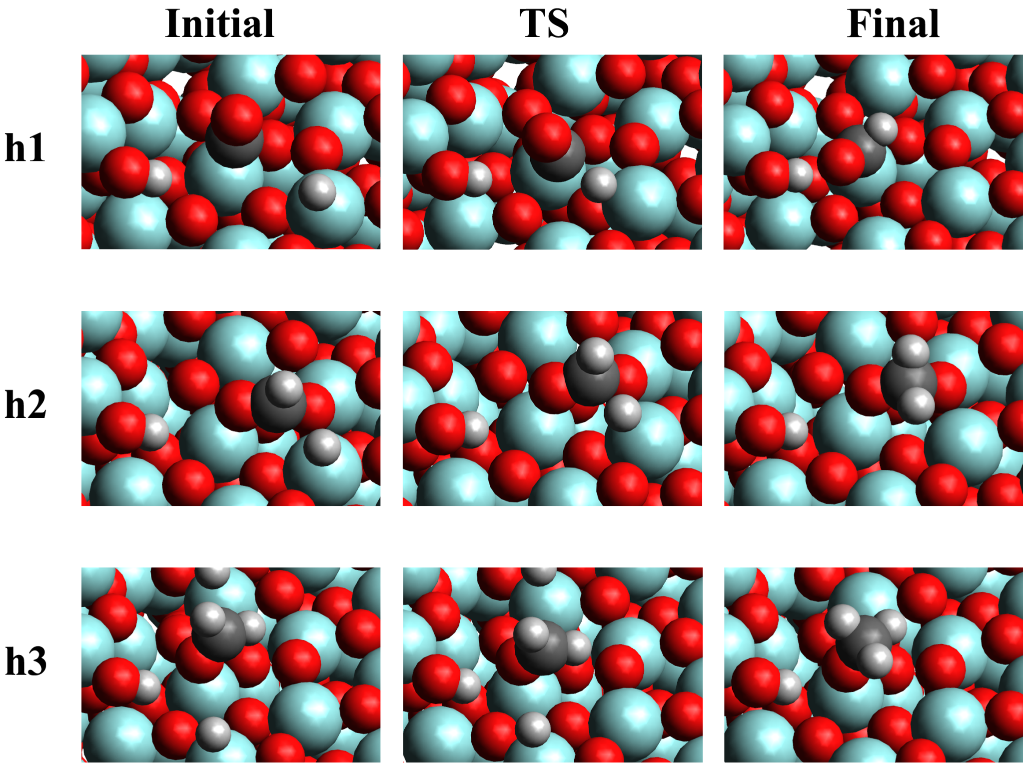

Figure 22: Three consecutive hydrogenation reactions for CO. Left column in initial state, middle is the found transition state and right column is the final state.

that the Zr-top sites work as a Brønsted acid in the hydrogenation reactions. Bi-coordinated surface OH groups were found to be mostly too stable to give up hydrogen. Terminal hydroxyls could behave differently, but those are left outside of these calculations. The most notable observation was that reaction h1 has the highest reaction barrier, while h2 and h3 have very low barriers. This suggests that the first hydrogenation step h1 is the rate controlling step governing the formation of formaldehyde and methoxy species.

Some questions remain open, most important being the feasibility of rearrangement of h1 final state to the formate-like h2 initial state. Thermodynamically this reaction is favourable, since the formate-like structure is the more stable one, but the activation energy for this reaction is still unknown. mainly because, for some reason, this particular reaction was surprisingly challenging for the NEB algorithm. One possible explanation is that a satisfactory interpolation between the initial and the final state was difficult, and the resulting path was too complex. Whatever the reason was, no satisfactory transition state was found for this reaction.

The formate-like adsorption geometry for formaldehyde included ZrO_2 lattice oxygen as a part of the molecule. Desorption of these formate like-species could be associated with formation of CO_2, however, if these species leaves the surface, it would lead to formation of oxygen vacancies, unless some more complicated mechanism is involved. Since selectivity for CO_2 is usually high in isosynthesis, investigating the role of this kind of mechanism could be beneficial.

7.3 C–O bond breaking

The most prominent problem for the studied reaction network is that CO-insertion didn't seem to happen readily between CO and adsorbed OCH_2 species. However, moving a CH_2 group from formaldehyde to lattice oxygen was found to give a species that is highly prone to forming of C–C bond. Therefore, the possibility of C–O bond breaking and methyl transfer reactions was investigated. This kind of mechanism has been proposed previously by Maruya *et al.* [92] They assumed that CO should be transformed to CH_2 species attached to one of the lattice oxygens. This mechanism resembles the one illustrated in figure 6 for the initiation of the carbon chain growth.

Transfer CH_2 to lattice oxygen could proceed by breaking a C–O bond of the final state of reaction h2 in figure 22. Since there is essentially two C–O bonds in this structure, the reaction could happen in both direction, forming either formaldehyde which is initial state of reaction h3 or CH_2 attached to the lattice oxygen. One mechanism that is promising for the reaction d1 is the H assisted dissociation (reaction d1), which involves reducing one oxygen of the bridged structure to an OH group. This results in a $HOCH_2$ intermediate, which then dissociates. Interestingly, this reaction also offers a mechanism for terminal OH formation, opening a possibility that subsequent hydrogenation reactions proceed with different mechanism utilizing terminal hydroxyls left to the surface.

The first step in this reaction scheme includes transferring an H atom from the surface to an oxygen of the adsorbed species. This reaction is labelled as r1. Unlike in the case of CH_nO hydrogenation reactions, H transfer from a lattice oxygen was found to be favourable in this reaction, as it seems that proton migration from

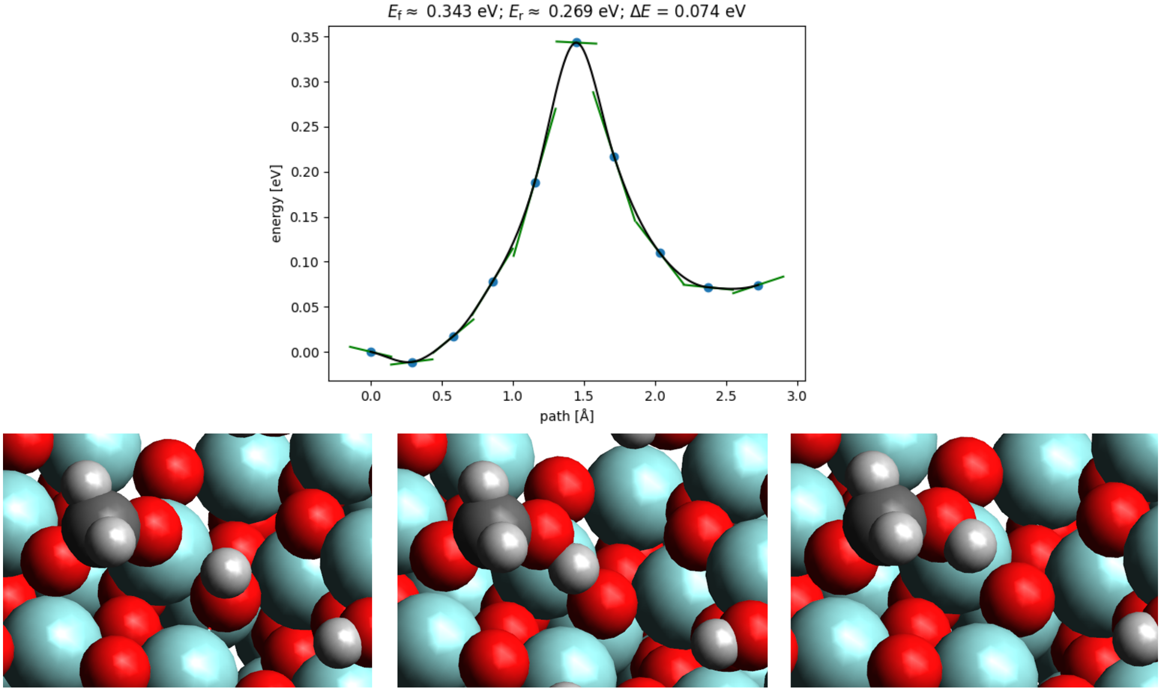

Figure 23: Reaction r1: Reduction of CH_2O species with corresponding NEB plot. Structure from left to right: the initial state, the transition state and the final state.

oxygen to oxygen happens more readily. Figure 23 shows again the initial and the final state found for this reaction, and the transition with the corresponding NEB plot.

Reaction r1 is followed by the reaction d1, a bond breaking reaction which results in the formation of a terminal OH group and the transfer of CH_2 to a bi-coordinated lattice oxygen. Structure optimization of the final state for this reaction gives an interesting bonding geometry where CH_2 is bonded to both bi-coordinated oxygen and Zr atom. This structure works also as an initial state for the CO insertion.

Reaction d1 has the highest activation energy out of all the reactions that were studied, 0.497 eV. Even tough activation energy is relatively high, thermodynamics on the other hand are highly favourable. The reaction energy of -2.4 eV made this also the most exothermic reaction. This reaction turned out to be remarkably ill-behaved in the NEB calculation, which can be seen by comparing the NEB plot in figure 24 to the r1 plot in figure 23, which is closer to an ideal NEB plot. Nonetheless, one transition state candidate was indentified, and vibrational

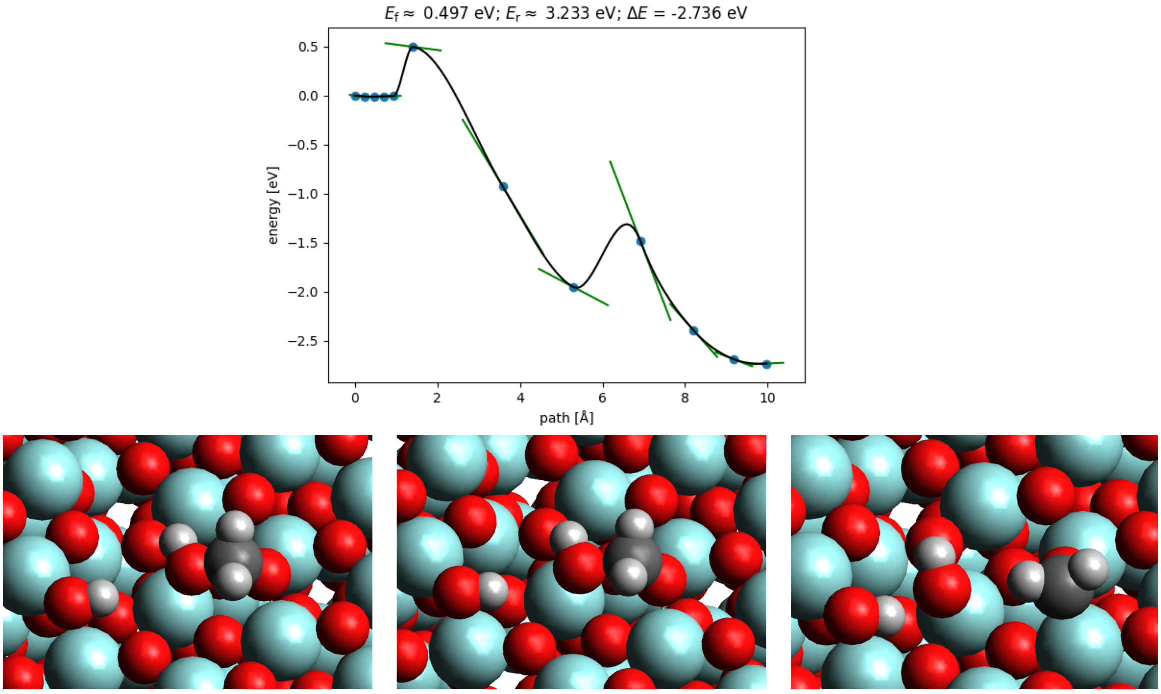

Figure 24: Reaction d1 and corresponding NEB plot. Structure from left to right: the initial state, the transition state and the final state.

analysis indeed confirmed that the found stucture is a transition state for the reaction. The behaviour of the d1 NEB is likely due to the effect of hydrogen coadsorption, which is discussed in section 7.6 where the same reaction is calculated also without coadsorbed hydrogen.

7.4 C–C coupling

There are a couple of possible ways to how carbon-carbon bonding could proceed. The first way is via CO-insertion, where a CO molecule binds to the structure forming carbon-carbon bond. This is believed to be also the initial way of C–C bond formation in isosynthesis [92], as discussed in section 5.3 Another possible way is bond formation via aldol condensation, but since in this thesis investigation is restricted to the formation of C_2 species, and C1 species can't couple via aldol condensation, only the CO-insertion is considered.

As stated briefly in section 7.3, it was found that CO insertion to a formaldehyde adsorbed onto zirconium is not feasible due to an unstable final structure, and

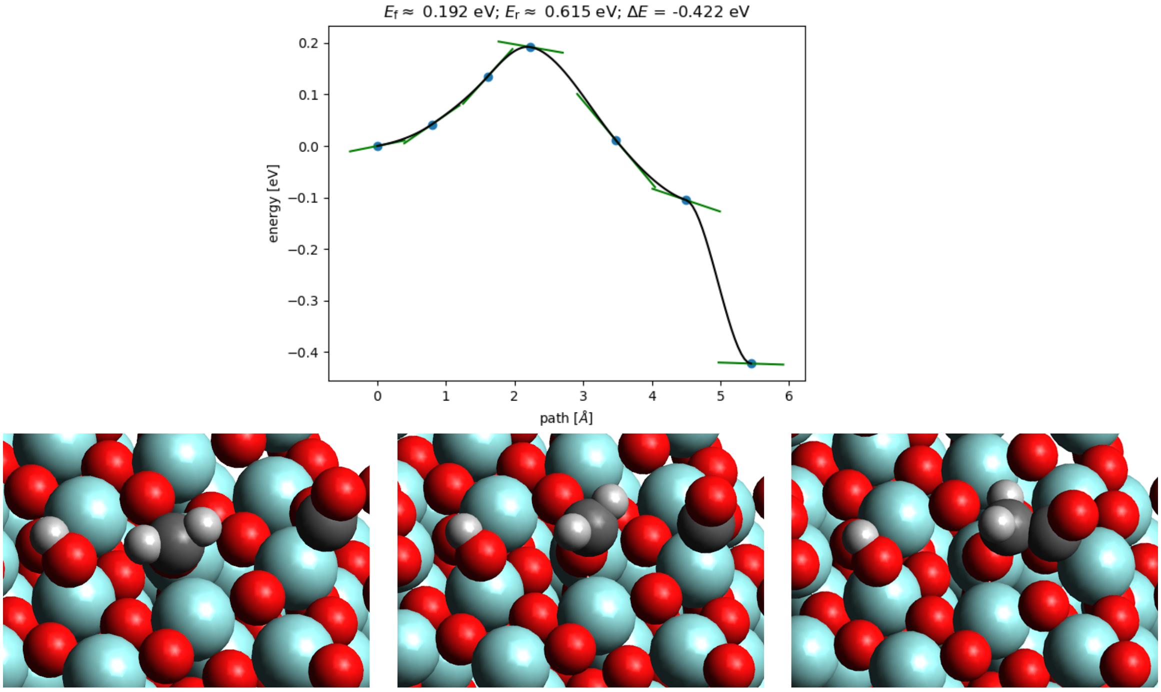

Figure 25: Reaction $i1_a$: CO insertion with corresponding NEB path.

therefore the C–O breaking reaction was investigated. CH_2 bound to a lattice oxygen was found to be highly susceptible to the CO insertion, and this gives us the reaction i1. The reaction energy of -0.422 eV tells that this elementary step is exothermic, and the NEB calculation for the path shown in figure 25 gave this reaction step a barrier of 0.192 eV. The reaction involves simultaneously both breaking the bond between CH_2 and Zr, and bond formation between CH_2 and CO. In this reaction, the inserted CO is first absorbed to edge Zr, which is the same site depicted in figure 20.

In the reaction $i1_a$, the OCH_2 molecule has to turn to complete the reaction, and it seems that the reaction barrier is mostly caused by this turning motion. This is further demonstrated by another NEB calculation (reaction $i1_b$), where the barrier is almost non-existent. This reaction has different initial sate, in which the inserting CO adsorbs to a terrace site instead of the step Zr. In this initial state, the OH group from the reaction d1 is also moved onto another Zr atom, and consequently the adsorption geometry for the initial state of this reaction resembles the linearly adsorbed formaldehyde. However, the transition state for this reaction is not confirmed via vibration analysis. The NEB plot in figure 26 shows how this

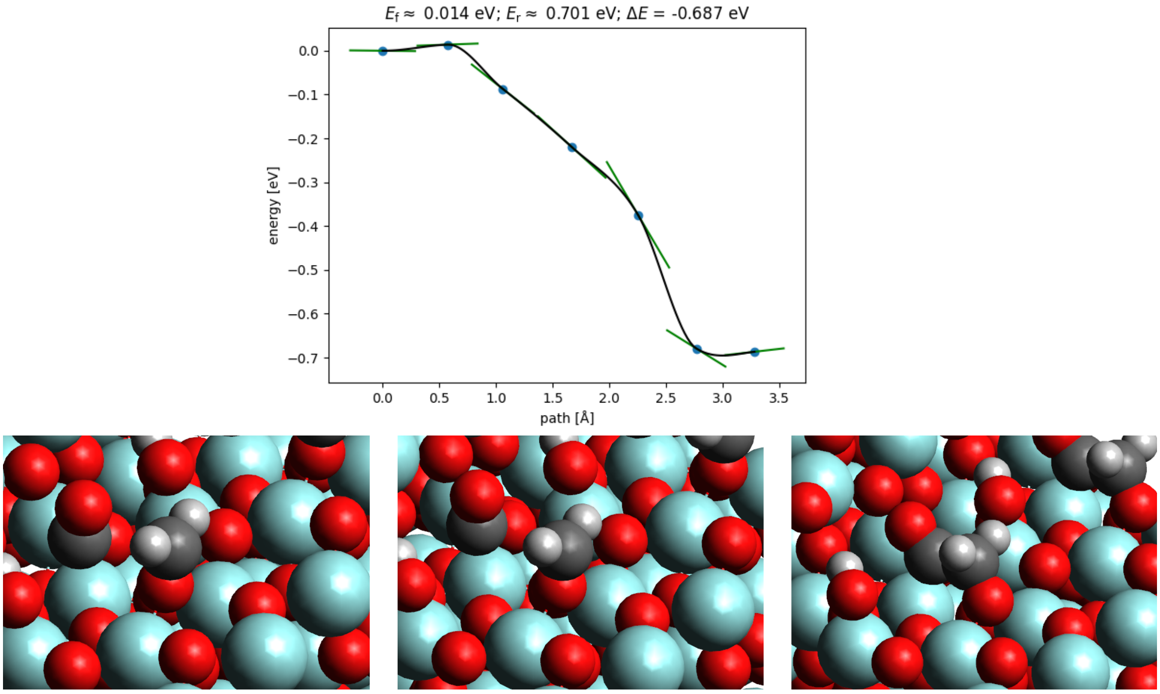

Figure 26: Reaction i1_b: CO insertion from different initial state. Structure from left to right: the initial state, the transition state and the final state.

another configuration leads to a basically barrierless, exothermic reaction. NEB gives a barrier of 0.014 eV, and a reaction energy of -0.687 eV. Since the barrier is almost non-existent and the initial state is structurally almost identical to the presumed transition state, it is more comfortable to talk about barrierless reaction and therefore the vibration analysis wasn't conducted for this path.

The results of these calculations show that the C–C coupling via CO insertion can happen remarkably easily from the configuration shown in figure 26. It could even be speculated that due to the low adsorption energy of CO, adsorption of a new CO during this state is not necessarily needed and the reaction could also proceed via the Eley-Rideal mechanism.

7.5 Adsorption of isobutane and isobutene

The calculations of this thesis mainly concerned the first steps of isosynthesis. However, adsorption of iso products was also investigated briefly on the flat$(\bar{1}11)$ surface.

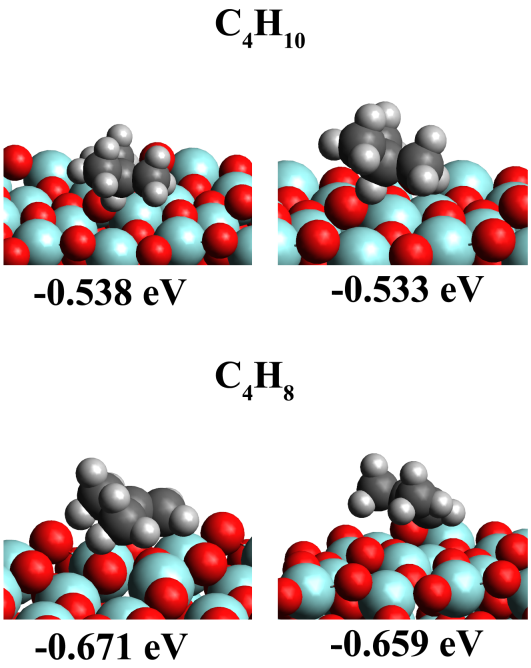

Figure 27: The best found adsorption geometries for isobutane (above) and isobutene (below) on the m-$ZrO_2(\bar{1}11)$ surface.

Because isobutane and isobutene are the desired products in isosynthesis, their adsorption onto a zirconia surface should be relatively weak. If these products absorb too strongly onto the surface, activity would be decreased. The two most stable adsorption geometries for isobutane and isobutene found on m-ZrO_2 $(\bar{1}11)$ surface are shown in figure 27. Adsorption energies are -0.538 eV for the isobutane, and -0.671 eV for the isobutene. Adsorption is therefore not too strong. The weak adsorption is also suggested by the long bond lengths between surface and the molecules. For the most stable structure of isobutene, Zr–C distance is 3.03 Å. For the most stable isobutane structure the shortest distance between the surface and the molecule is the distance between the central hydrogen and Zr, which is 2.728 Å. These results suggest that the adsorption between the m-ZrO_2 $(\bar{1}11)$ surface and i-C_4 products is mainly physisorption.

7.6 Effect of coadsorbates

In the beginning, coadsorbed hydrogen was included on the surface to balance the system, so that there would always be an even number of hydrogen atoms adsorbed onto the surface. These coadsorbed hydrogen atoms, however, turned out to have a significant effect on behavior of the system.

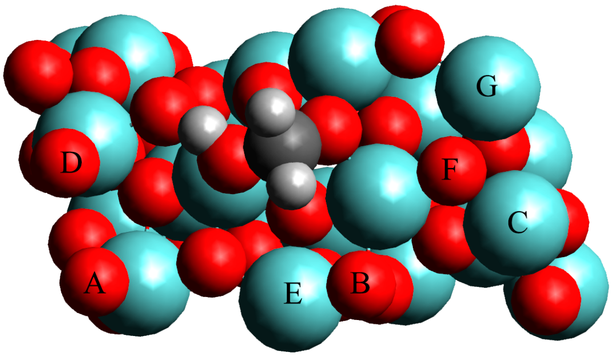

Figure 28: Structure used for testing the coadsorption effects, with labelling on each atom that was used.

To better understand how coadsorbed hydrogen affects the adsorption, the initial and final states of reaction d1 (see table 6) were calculated with varying numbers of hydrogen atoms adsorbed on different surface sites, and the reaction energies corresponding to the reaction d1 were calculated. The results of these calculations are shown in table 5. Figure 28 shows the used structure for the initial state without any coadsorbed hydrogen along with the labeling that is used in table 5. For selected structures density of states were also plotted to see if coadsorbed hydrogen affects the Fermi level. Lastly, the effect of coadsorption on the activation energy of reaction d1 was also studied by calculating NEB for reaction d1 without any coadsorbed hydrogen.

NEB calculation gave an energy barrier of 0.35 eV, which is slightly lower than the value of almost 0.5 eV given in section 7.3. Difference in the energy barrier with and without the coadsorbed hydrogen is not too large, but the effect on the reaction energy is significant. Without hydrogen, the reaction energy is -0.424 eV, which is almost 2 eV more endothermic than the reaction energy calculated in section 7.3. Notably the effect on the convergence of the NEB calculation is dramatic. Comparing the NEB plots (figures 24 and 29), one can see that without coadsorbed H, the NEB path is much smoother. These kind of results are expected if adsorbed hydrogens are close to investigated species, affecting the immediate chemical environment. In this case, however, there are multiple atoms between the CH_2OH species and the hydrogens, as seen in the figure 24. This indicates that the effect is non-local. The observed effect is unfortunate since it raises questions about the generalizability of the DFT results, such as the reaction energies. As such, the effect itself is quite interesting, albeit not totally unexpected since coadsorption is known to affect adsorption on oxides due to the acid-base interactions involved.[123]

Table 5: Calculated reaction energies for reaction d1 with different permutations of coadsorbed hydrogen. N is a number of coadsorbed H atoms, and the labels in positions refer to figure 28

N	ΔE [eV]	positions
0	-0.424451	-
1	-2.736	A
1	-2.882156	B
1	1.375279	C
1	-2.992604	D
2	0.147861	A,E
2	-0.096449	A,B
3	-2.915529	A, B, C
3	-2.840575	A,C,F
3	1.959234	C,E,F
3	-2.802185	B,C,F

As mentioned earlier, coadsorbed hydrogen atoms seem to have the most dramatic effect on the reaction energy. Figures 24 and 29 show that even though the atomic structures look similar, the reaction energy is significantly larger in the presence of coadsorbed hydrogen, which likely means that hydrogen can stabilize or destabilize some structures. A similar effect is observed in table 5, where the reaction energies stretch form endothermic 1.38 eV to exothermic -2.99 eV.

The effect of hydrogen coadsorption was also investigated in the context of CO adsorption. The absorption configuration of the hydrogen was the same as in figure 19. Adsorption geometries of figure 20 were calculated again with the coadsrorbed hydrogen. For the terrace site, coadsorption has practically no effect on distance between the surface Zr and C in CO. The distance is around 2.56 Å with and

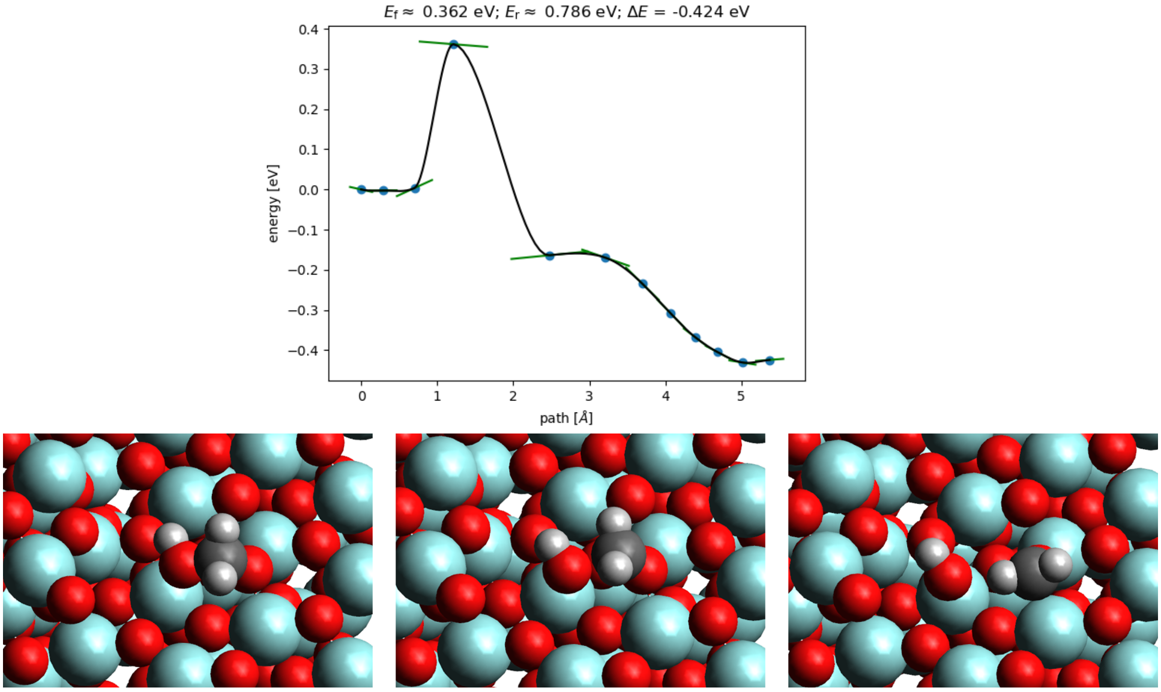

Figure 29: The NEB path for reaction d1 (figure 24) without coadsorbed hydrogen.

without the hydrogen. The effect on step Zr is larger and the distance between the surface Zr and carbon decreases from 2.56 Å to 2.29 Å when hydrogen in involved. This effect is not surprising, since in this configuration CO and one hydrogen are adsoprbed to the same Zr atom. Adsorption energies for CO with coadsorbed hydrogen were calculated using the formula

$$E_{\mathrm{surf+H_2+CO}} - E_{\mathrm{surf+H_2}} - E_{\mathrm{CO}}. \tag{18}$$

For the terrace, calculated adsorption energy is -0.656 eV, and for the step the energy is -0.471 eV. These result are relatively close to those given in section 7.1.2. The only notable difference is that the adsorption energy on the step site relative to the terrace site has increased, but considering the adsorption geometries in figure 30, this is somewhat expected.

Figure 31 shows how hydrogen coadsorption affects on density of states. Notably, coadsorption shifts the Fermi level of the system, indicating that the hydrogen adsorption can have a significant effect on the properties of the catalyst. These results, however, are insufficient to draw any trends.

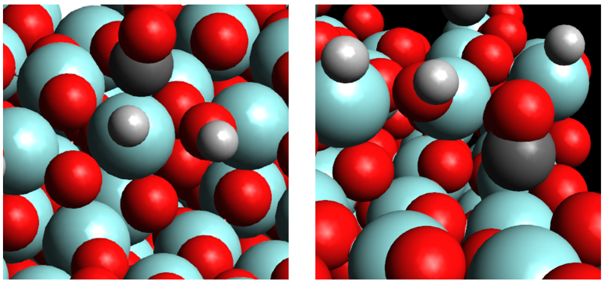

Figure 30: CO adsorption structures with coadsorbed hydrogen. Note that the CO adsorption sites are as in figure 20, but combined with the final state of H_2 dissociative adsorption in figure 19.

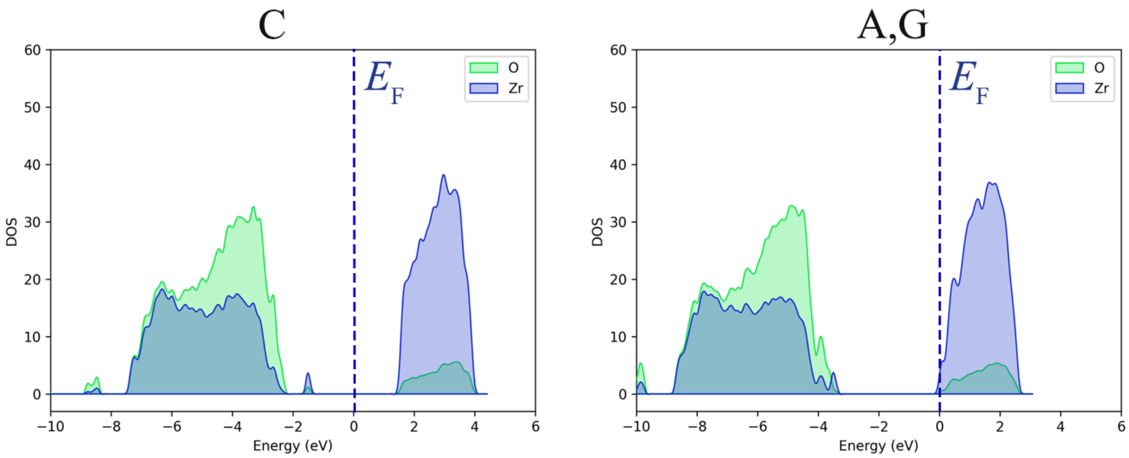

Figure 31: DOS plots for two structures with differing amounts of coadsorbed hydrogen. Labels C, A and G refer to hydrogen adsorption sites shown in figure 28 .The Fermi level is marked with a vertical line.

7.7 Summary of results

In this thesis, the focus of the calculations was on the initiation of the isosynthesis reaction on zirconia. The reactions studied consisted of a path from syngas adsorption to the first carbon-carbon bond formation. One path from syngas adsorption to C–C bond formation was identified. The investigated elementary steps are listed in the table 6 along with the barrier energies acquired from the NEB calculations.

According to the barrier energies, the hydrogenation of CO happens fairly easily given that there is excess hydrogen on the surface. CO-insertion occurs easily if the initially absorbed CO can be transformed to CH_2-species. More precisely,

Table 6: The considered elementary steps together with reaction energies (ΔE), activation energies (E_a) and imaginary vibration frequencies for the transition states

label	reaction	ΔE (eV)	E_a (eV)	vib (meV)
dh	$H_2 \longrightarrow H^+ + H^-$	-0.242	0.387	112.1i
h1	$CO + H \longrightarrow HCO$	-0.576	0.324	38.4i
h2	$HCO + H \longrightarrow H_2CO$	-0.764	0.089	45.0i
h3	$H_2CO + H \longrightarrow H_3CO$	-2.090	0.019	7.0i
r1	$H_2CO + H \longrightarrow H_2COH$	0.074	0.343	105.4i
d1	$H_2COH \longrightarrow H_2C + OH$	-2.397	0.497	9.7i
i1$_\mathbf{a}$	$H_2C + CO \longrightarrow H_2C_2O$	-0.422	0.192	19.0i
i1$_\mathbf{b}$	$H_2C + CO \longrightarrow H_2C_2O$	-0.687	0.014	-

for reactions to proceed, it seems to be necessary to transfer carbon to a lattice oxygen. Surprisingly, most of the elementary steps are exothermic, but this could also be due to the observed coadsorption effect, which makes the interpretation of reaction energies difficult. The largest activation energy was found for C–O bond breaking (reaction d1). Figure 32 shows the sketched reaction mechanism from CO adsorption to C–C coupling. The reactions happening on a catalytic surface are hard to depict with traditional structure diagrams, but together with the presented rendered images, figure 32 should give a good idea of the studied reaction path.

All in all, 6 elementary steps were identified for the path leading to the first C–C bond formation. These include all the reactions in table 6 excluding the methoxy formation (reaction h2), and the reaction that transforms the bonding geometry of HCO from linear to the formate structure. Normally, it would be ideal to plot the potential energy surface (PES). However, since there are still some gaps in the full reaction mechanism, full PES diagram cannot be drawn. The situation is further complicated by the changing number of hydrogen atoms in the periodic cell, which makes the calculation of adsorption energies difficult from the perspective of choosing the reference. Due to these complications, a PES diagram can easily be misleading, and therefore the choice was made to leave the diagram out. Instead, the reactions in table 6 should be understood as a closely related individual reaction steps.

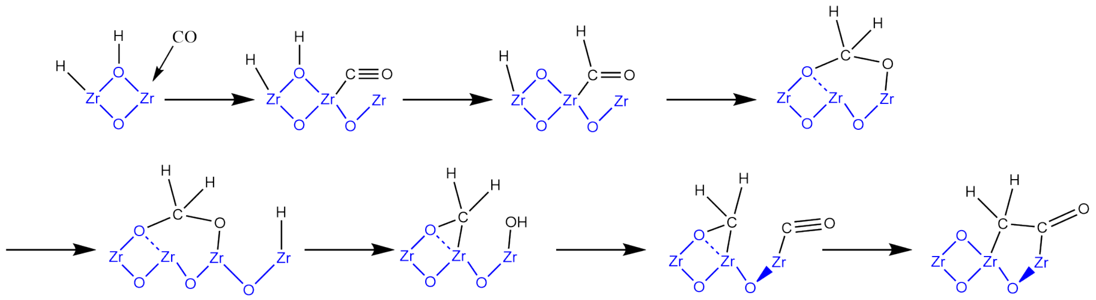

Figure 32: A schematic drawing for a possible mechanism leading to the first C_2 oxygenate species.

8 DFT molecular dynamics for syngas

One limitation of the static DFT calculations is that they describe the system at 0 K temperature. To gain a better understanding of the activation at the surface under more realistic reaction conditions, an arbitrary composition of syngas was simulated on m-$ZrO_2(\bar{2}12)$ surface in the NVT ensemble using a Langevin thermostat. The average temperature was kept at 700 K, as this is close to the reported temperature for isosynthesis [5]. The Langevin thermostat was chosen over the Nosé-Hoover or the Berendsen thermostats because it has been shown to give a more uniform temperature.[20] Proton and oxygen migration and diffusion have been simulated in bulk zirconia before [124], but at the moment of writing this thesis, surface diffusion from the perspective of heterogeneous catalysis with DFT-MD is a less studied subject.

Hydrogen is a bit problematic species for molecular dynamics, since the equations of motion are solved classically, and for light molecules like hydrogen the quantum mechanical nature is apparent. In these calculations the possibility of tunneling is omitted, but it is something that should be kept in mind. For practical reasons, the mass of hydrogen atoms was set to correspond to deuterium. This is commonly done to ensure that the system behaves adiabatically. [125]

Two simulation runs with slightly different initial configurations were computed. Both simulations included syngas in a 1:2 CO/H_2 ratio on a stepped m-ZrO_2 surface, which is the same model used in the other calculations. For the MD simulations the cell was repeated once to create a 4x4 surface slab consisting of 88 O atoms, 44 Zr atoms, two CO molecules and four H_2 molecules. Due to larger

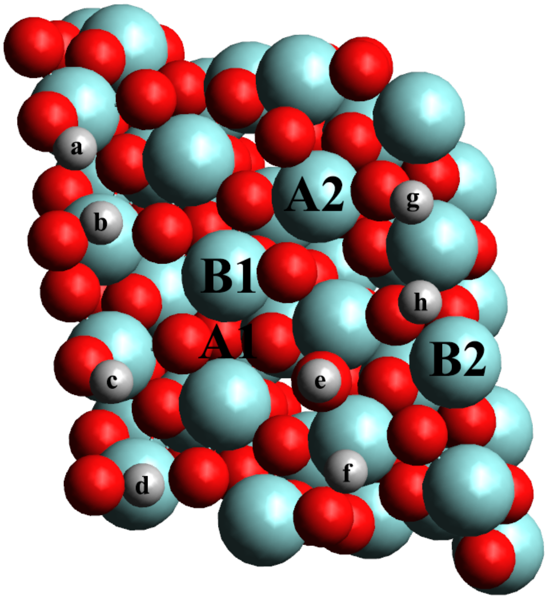

Figure 33: The top view of the initial states for DFT-MD simulations A and B. The CO molecules are not visualized. A and B mark the positions of CO molecules for each simulation.

cell, the grid points given in section 6 had to be redefined to ensure the 0.2 Å grid spacing. The new grid points for this cell were (60,64,156).

It was found that a non-periodic z-direction caused problems, as the simulation crashed immediately if one molecule happened to cross the upper boundary of the simulation cell. This is why periodic boundary conditions were implemented also in the z direction. Implementing full 3D periodic boundary conditions can be dangerous, since if two slabs are too close to each other in z-direction, calculations give an incorrect description for the potential energy surface. To ensure that the vertically periodic surfaces affect the results as little as possible, the vacuum between the surface slabs was increased to approximately 35 Å.

The H_2 molecules was dissociated onto the surface. The initial positions of the hydrogen atoms is the same in the both simulation runs, but the positions of the CO molecules were changed. Figure 33 shows the initial states of the two runs, which are labelled as A and B. The total simulation times with 1 fs time steps for the simulations A and B were 13 ps, and 11 ps, respectively.

8.1 Results of MD simulations

Figure 34 shows repeated surfaces before and after the simulations. These images show how hydrogen has spread out and reacted with CO. Different surface species formed during the simulations can also be seen. At first glance, it seems that hydrogen is more able to move around the surface compared to the CH_nO species. Notably, according to the simulations, hydrogen atoms can transfer between bi-coordinated lattice oxygens.

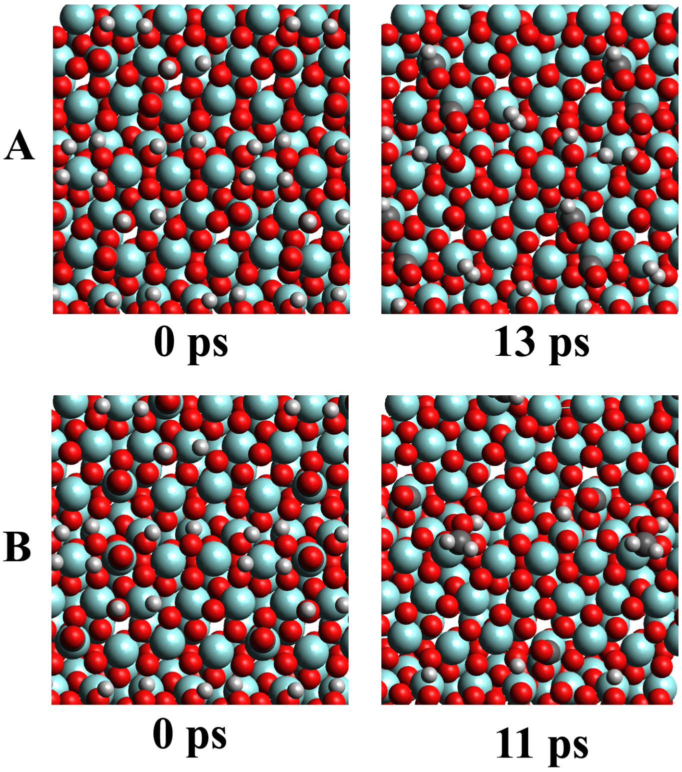

Figure 34: Surfaces A (top) and B (bottom) before and after the MD simulation.

When running MD simulations, it is important to ensure that the average temperature is maintained properly, and the temperature is uniform and no temperature gradients are observed in different parts of the system. [20] With this in mind, the temperatures of both simulations were plotted to see if any anomalies can be detected (Figure 35). The thermalization phase can be seen as a large spike at the beginning of the both simulations. Thermalization seems to take around 2 ps, after which the temperature remains steadily around 700 K. The figure also shows separately the average temperature of hydrogen atoms, and it seems that it is in line with the overall temperature of the system.

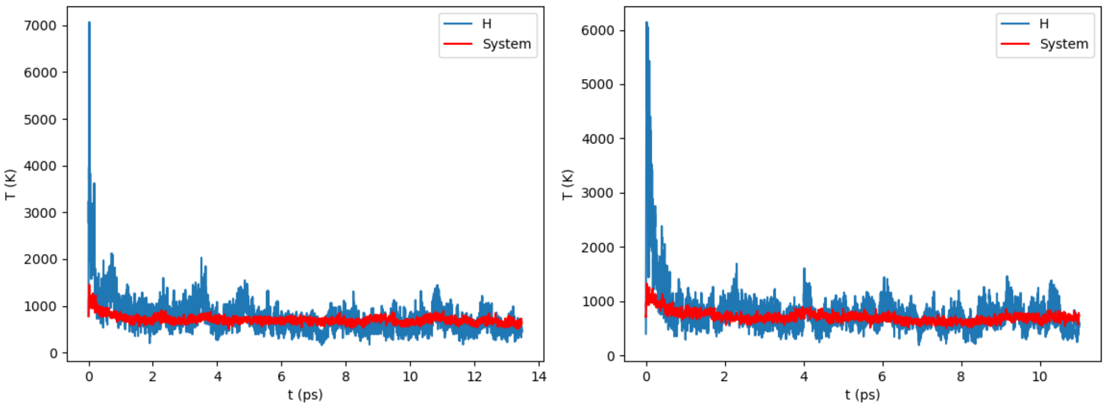

Figure 35: The temperature variation as a function of time. Simulation A on the left and simulation B on the right. The red line depicts the average temperature of the whole system and the blue line is the average temperature of hydrogen atoms.

8.1.1 Observed chemistry

During both simulations, some of the hydrogen atoms combined to H_2 and desorbed, while some H atoms stayed on the surface and participated in surface reactions. One H_2 formation was observed during the thermalization phase of each simulation, and this happened at 0.51 ps in simulation A , and at 0.29 ps in simulation B. In simulation B, another H_2 formation event is observed at 4.0 ps, and on simulation A at 12.2 ps. These later H_2 formation and desorption events are more interesting, since they happen after the thermalization phase and suggest that at 700 K dissociatively adsorbed hydrogen can easily recombine back to molecular H_2.

To visualize the migration of hydrogen atoms better, kernel density estimation was used to construct a heat map out of the atomic position throughout the simulations (figure 36).

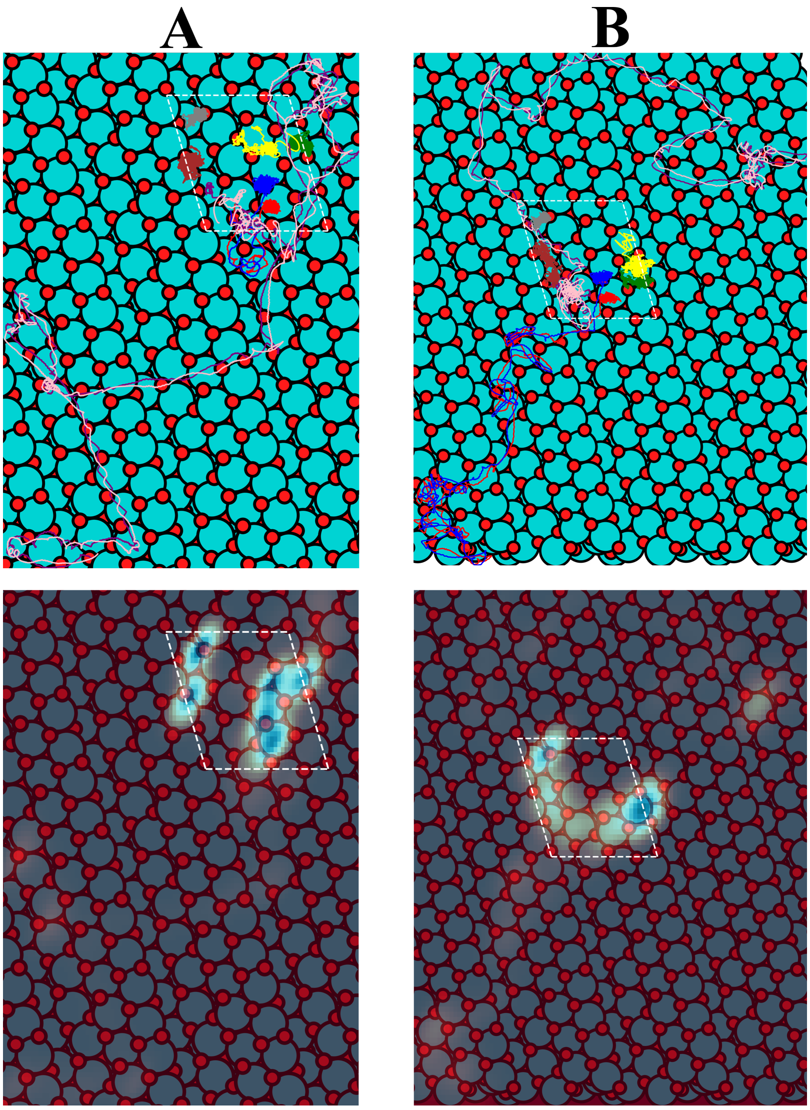

Figure 36: Paths of individual hydrogen atoms on zirconia surface (above) and heat maps calculated with KDE highlighting sites where hydrogen atoms spend most time during simulations A and B (below). The white dashed lines represent boundaries of the periodic cell.

For calculating the KDE, a scipy implementation with Gaussian kernel-functions was used. [126] Heat maps for both simulations and paths of individual hydrogen atoms are shown in figure 36. The figure shows how recombined hydrogen molecules start to migrate around the surface and leave the original cell, while other hydrogen atoms move less.

In simulation B, one desorbed H_2 molecule started to exhibit strong attraction to the surface after it had drifted for a while. This can be seen in the figure 36 B heatmap as the lighter spot at the upper right corner of the plot. Seeing some kind of interaction between surface and gas phase H_2 gives more credibility to the possibility of dissociative adsorption of H_2 on zirconia. CO hydrogenation was also observed during both runs. In simulation B, two consecutive hydrogenations happen during the thermalization phase. Since the reaction takes place during the thermalization, not much can be deduced about the feasibility of these reactions under the target temperature. However, the resulted formaldehyde didn't react further during the simulation which suggest that the structure is somewhat stable at 700 K. In simulation A, hydrogenation is seen after the thermalization. Hydrogen atoms h and g are initially close to each other, but after 10 ps, hydrogen g combines with the carbon of A2 CO. This reaction is nicely visualized by plotting the distance between hydrogens h and g along with the distance between the hydrogen g and the carbon of the CO molecule (figure 37). Plot 37 shows that, at the beginning, hydrogen h has almost the same distance to hydrogen g and carbon A2. The distance between hydrogen h and carbon A2 oscillates approximately between 1 and 3 Å, until the hydrogenation reaction takes place around 10 ps.

In simulation B, one of the hydrogens reduces formaldehyde to H_2COH species. This reaction can lead to methanol formation. Interestingly, methoxy formation was not observed, which should be a highly favourable reaction according to the static DFT calculations. likely due to the fact that after formaldehyde and H_2 formation there is no hydrogen left for methoxy formation. Also, two 10 ps runs can't completely describe possible reactivity on the surface.

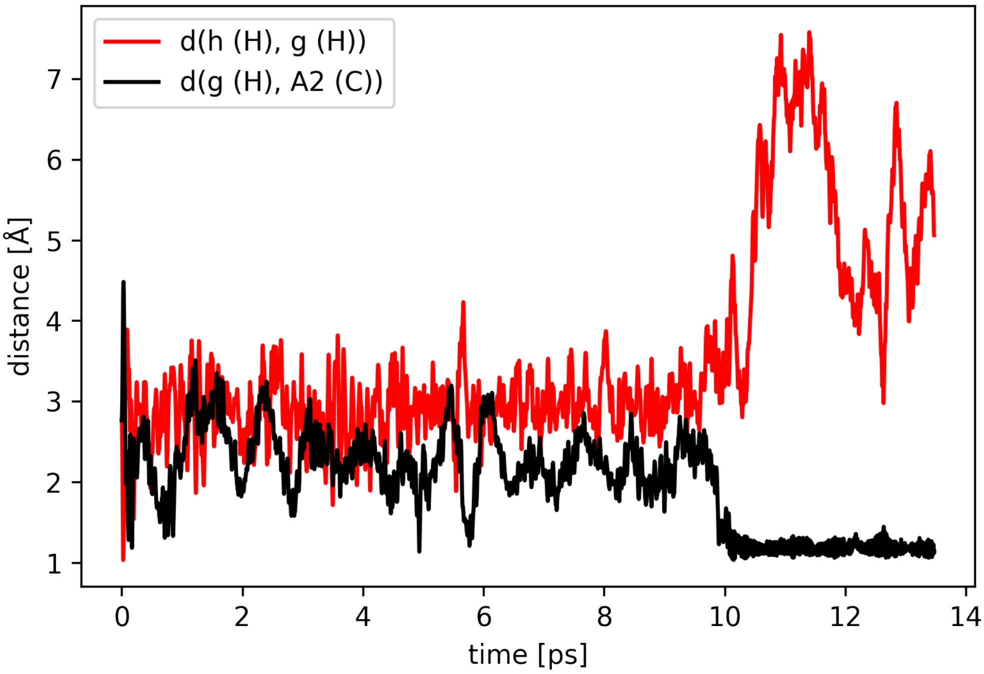

Figure 37: Distance between hydrogen atoms h and g and distance between carbon A2 and hydrogen g during simulation A.

8.1.2 Surface restructuring

One important factor concerning catalytic materials are possible structural changes during the reaction at real reaction conditions. Static DFT calculations depict the surface as unchanging, but this is not necessarily true, and some hints of possible changes in the ZrO_2 structure were observed via the DFT-MD simulations. In the simulation A structure of the catalyst remained relatively unchanged, but during the thermalization phase of simulation B, one of the bi-coordinated OH groups at the step site rearranged to form terminal OH group and oxygen vacancy. The formed hydroxyl was stable enough to remain in this position for the rest of the simulation. Figure 38 depicts this process by showing this particular OH group at the beginning and at the end of the simulation A. Since the rearrangement of the oxygen happened during the thermalization phase it is unclear how easily this process actually proceeds, but it could be that the coadsorption of CO on the step plays a role in this event.

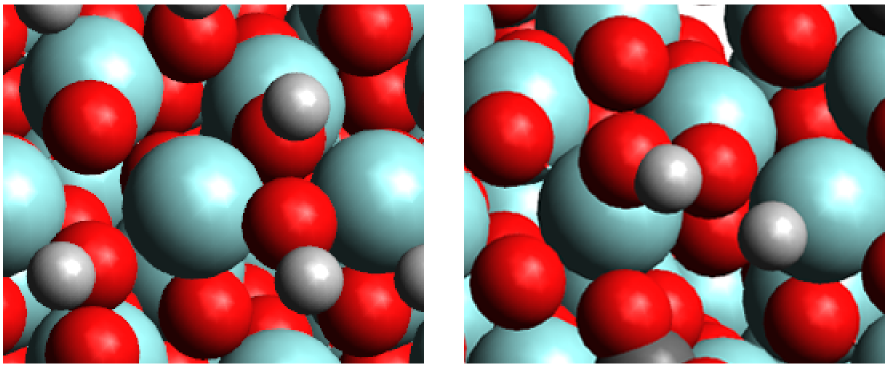

Figure 38: A bi-coordinated hydroxyl group at 0 ps (left) moves to the top site of a Zr atom, becoming a terminal hydroxyl (right), where it stays until the end of the simulation at 13 ps.

These observations are in line with the earlier studies stating that bi-coordinated oxygens form more stable vacancies, and surface structuring can enhance the formation of vacancies.[59] The event seen in the simulation offers one possible mechanism for the formation of terminal hydroxyls, and the role of structural defects or nanostructuring in the formation of these groups is a subject that could be interesting to study further.

8.2 Limitations of the MD model

When looking more carefully at atoms close to periodic boundaries, one can see how problems could arise easily. In the simulations hydrogen atoms h and b are at the opposite sites of the cell, but the periodic image of hydrogen b is right next to hydrogen h (see figure 33). This oversight of periodicity resulted in quite high local hydrogen coverage on the step, while the terrace had less hydrogen. This might be the reason for the fast H_2 formation observed during the thermalization phases of the simulations.

Another problem that concerns both DFT-MD calculations is that the used surface models lack the gas phase syngas altogether, and therefore DFT-MD can't give an entirely accurate description of the real reaction conditions. Most importantly adsorption of CO is not depicted in these simulations, and the coverage of the surface is arbitrary.

9 Conclusions

The computational study conducted for this thesis investigated the chemistry involved in the initialization of isosynthesis on a stepped m-ZrO_2 surface. It was found that while the step defect promoted the heterolytic dissociation of H_2, it did not have a significant effect on the adsorption energy of CO. These results support the earlier literature considering the ability of stepped ZrO_2 to facilitate dissociative adsorption.[67]

One possible pathway for C–C coupling on zirconia was identified, in which hydrogenated CO forms η^2-formaldehyde species with a lattice oxygen, and this species proceeds to form a C_2H_2O species via CO insertion. The investigated mechanism (figure 32) shares some resemblance to suggested mechanisms from the 1980s and 1990s [5, 92] (figure 6). From the studied elementary steps, the breaking of the C–O bond was found to be the most energetically demanding step. When it comes to the hydrogenation reactions, the formyl formation has the highest reaction barrier, while formaldehyde and methoxy formation were found to have substantially lower, almost non-existent barriers.

Coadsorption of hydrogen appears to have a significant effect on the properties of zirconia, and this results in much more complex behavior than anticipated. This phenomenon affects the reaction energies, and due to this effect, it is unclear how generalizable now calculated DFT results are. Therefore, a more detailed look on hydrogen coadsorption would make an interesting topic for further studies.

The DFT-MD simulations of syngas on a periodic m-ZrO_2 surface showed that hydrogenation reactions can happen at 700 K. With the two 10 ps simulation runs, hydrogenation, and associative desorption of H_2 were observed, but the most notable result of the simulations is the restructuring of a bi-coordinated step lattice oxygen to a terminal hydroxyl and an oxygen vacancy.

The formation of terminal hydroxyl groups in the absence of H_2O was also a topic of interest, and two possible mechanisms for this event were identified. The first is the restructuring of bi-coordinated lattice oxygens mentioned above, and the second is the reaction d1 (table 6), which produces one hydroxyl via dissociation of $HOCH_2$.

To give a concluding remark, the computational work done in this study supported the previous literature in many ways, and revealed more details concerning the initial phases of isosynthesis on zirconia. There still remain a lot of unknowns concerning the full reaction network, such as the detailed chain growth and branching mechanism and possible side reactions like methanol formation, and these would be interesting topics to explore with further calculations.

References

[1] Maitlis, P. M. and de Klerk, A., *Greener Fischer-Tropsch Processes: For Fuels and Feedstocks*, John Wiley & Sons, Incorporated, Somerset, Germany, **2013**.

[2] Kim, H., Kim, D., Park, Y.-K. and Jeon, J.-K., Synthesis of jet fuel through the oligomerization of butenes on zeolite catalysts, *Res. Chem. Intermed.*, **2018**, 44, 3823–3833.

[3] Guo, X., Guo, L., Zeng, Y., Kosol, R., Gao, X., Yoneyama, Y., Yang, G. and Tsubaki, N., Catalytic oligomerization of isobutyl alcohol to jet fuels over dealuminated zeolite Beta, *Catal. Today*, **2021**, 368, 196–203.

[4] Shah, Y. T. and Perrotta, A. J., Catalysts for Fischer-Tropsch and Isosynthesis, *Product R&D*, **1976**, 15, 123–131.

[5] Anthony, R. G. and Akgerman, A., Catalyst and process development for synthesis gas conversion to isobutylene. final report, september 1, 1990–january 31, 1994, **1994**, texas A&M Univ., College Station, TX (USA). Research Foundation.

[6] Verkerk, K. A., Jaeger, B., Finkeldei, C.-H. and Keim, W., Recent developments in isobutanol synthesis from synthesis gas, *Appl. Catal. A: Gen.*, **1999**, 186, 407–431.

[7] Nørskov, J. K., Studt, F., Abild-Pedersen, F. and Bligaard, T., *Fundamental Concepts in Heterogeneous Catalysis*, John Wiley & Sons, Incorporated, **2014**.

[8] Chorkendorff, I. and Niemansverdriet, J. W., *Concepts of modern catalysis and kinetics*, 3rd, rev. edition, Wiley-VCH, Newark, **2017**.

[9] van Santen, R. A., *Modern Heterogeneous Catalysis*, Wiley-VCH, **2017**.

[10] Szabo, A. and Ostlund, N., *Modern Quantum Chemistry: Introduction to advanced electronic structure theory*, 3rd, rev. ed edition, Dover publications, INC, Mineola, New York, USA, **1989**.

[11] Sholl, D. S., *Density Functional Theory: A Practical Introduction*, Wiley-Interscience, **2009**.

[12] Koch, W., *A chemist's guide to density functional theory*, 2nd ed edition, Wiley-VCH, Weinheim, **2001**.

[13] Chen, B. W. J., Xu, L. and Mavrikakis, M., Computational Methods in Heterogeneous Catalysis, *Chem. Rev.*, **2021**, 121, 1007–1048.

[14] Kresse, G. and Furthmüller, J., Efficient iterative schemes for *ab initio* total-energy calculations using a plane-wave basis set, *Phys. Rev. B*, **1996**, 54, 11169–11186.

[15] Hammer, B., Hansen, L. B. and Nørskov, J. K., Improved adsorption energetics within density-functional theory using revised Perdew-Burke-Ernzerhof functionals, *Phys. Rev. B*, **1999**, 59, 7413–7421.

[16] Kulik, H. J., Perspective: Treating electron over-delocalization with the dft+u method, *J. Chem. Phys.*, **2015**, 142, 240901.

[17] Korpelin, V., Sahoo, G., Ikonen, R. and Honkala, K., ReO as a Brønsted acidic modifier in glycerol hydrodeoxygenation: Computational insight into the balance between acid and metal catalysis, *J. Catal.*, **2023**, 422, 12–23.

[18] Liu, H., Zhang, R., Ling, L., Wang, Q., Wang, B. and Li, D., Insight into the preferred formation mechanism of long-chain hydrocarbons in fischer–tropsch synthesis on Hcp Co(10-11) surfaces from DFT and microkinetic modeling, *Catal. Sci. Technol.*, **2017**, 7.

[19] Grabow, L. C. and Mavrikakis, M., Mechanism of Methanol Synthesis on Cu through CO_2 and CO Hydrogenation, *ACS Catal.*, **2011**, 1, 365–384.

[20] Korpelin, V., Kiljunen, T., Melander, M. M., Caro, M. A., Kristoffersen, H. H., Mammen, N., Apaja, V. and Honkala, K., Addressing Dynamics at Catalytic Heterogeneous Interfaces with DFT-MD: Anomalous Temperature Distributions from Commonly Used Thermostats, *J. Phys. Chem. Lett.*, **2022**, 13, 2644–2652.

[21] Sato, R., Ohkuma, S., Shibuta, Y., Shimojo, F. and Yamaguchi, S., Proton Migration on Hydrated Surface of Cubic ZrO2: Ab initio Molecular Dynamics Simulation, *J. Phys. Chem. C*, **2015**, 119, 28925–28933.

[22] Reddy, B. M., Khan, A., Lakshmanan, P., Aouine, M., Loridant, S. and Volta, J.-C., Structural Characterization of Nanosized CeO $_2$ -SiO $_2$, CeO $_2$ -TiO$_2$, and CeO$_2$ -ZrO$_2$ Catalysts by XRD, Raman, and HREM Techniques, *J. Phys. Chem. B*, **2005**, 109, 3355–3363.

[23] Christensen, A. and Carter, E. A., First-principles study of the surfaces of zirconia, *Phys. Rev. B*, **1998**, 58, 8050–8064.

[24] Witoon, T., Chalorngtham, J., Dumrongbunditkul, P., Chareonpanich, M. and Limtrakul, J., CO$_2$ hydrogenation to methanol over Cu/ZrO$_2$ catalysts: Effects of zirconia phases, *J. Chem. Eng.*, **2016**, 293, 327–336.

[25] McFarland, E. W. and Metiu, H., Catalysis by Doped Oxides, *Chem. Rev.*, **2013**, 113, 4391–4427, publisher: American Chemical Society.

[26] Li, W., Nie, X., Jiang, X., Zhang, A., Ding, F., Liu, M., Liu, Z., Guo, X. and Song, C., ZrO$_2$ support imparts superior activity and stability of Co catalysts for CO$_2$ methanation, *Appl. Catal. B: Environ.*, **2018**, 220, 397–408.

[27] Fuller, M. P. and Griffiths, P. R., Diffuse reflectance measurements by infrared Fourier transform spectrometry, *Anal. Chem.*, **1978**, 50, 1906–1910.

[28] Xie, C., Yan, D., Li, H., Du, S., Chen, W., Wang, Y., Zou, Y., Chen, R. and Wang, S., Defect Chemistry in Heterogeneous Catalysis: Recognition, Understanding, and Utilization, *ACS Catal.*, **2020**, 10, 11082–11098.

[29] Lunsford, J. H., Catalytic conversion of methane to more useful chemicals and fuels: a challenge for the 21st century, *Catal. Today*, **2000**, 63, 165–174.

[30] Yusuf, M., Farooqi, A. S., Al-Kahtani, A. A., Ubaidullah, M., Alam, M. A., Keong, L. K., Hellgardt, K. and Abdullah, B., Syngas production from greenhouse gases using Ni–W bimetallic catalyst via dry methane reforming: Effect of W addition, *Int. J. Hydrog. Energy*, **2021**, 46, 27044–27061.

[31] Horn, R. and Schlögl, R., Methane Activation by Heterogeneous Catalysis, *Catal. Lett.*, **2015**, 145, 23–39.

[32] Siang, T., Jalil, A., Liew, S., Owgi, A. and Rahman, A., A review on state-of-the-art catalysts for methane partial oxidation to syngas production, *Catal. Rev.*, **2022**, 1–57.

[33] LeValley, T. L., Richard, A. R. and Fan, M., The progress in water gas shift and steam reforming hydrogen production technologies – A review, *Int. J. Hydrog. Energy*, **2014**, 39, 16983–17000.

[34] Chen, W.-H. and Chen, C.-Y., Water gas shift reaction for hydrogen production and carbon dioxide capture: A review, *Appl. Energy*, **2020**, 258, 114078.

[35] Kohn, M. P., Castaldi, M. J. and Farrauto, R. J., Biogas reforming for syngas production: The effect of methyl chloride, *Appl. Catal. B: Environ.*, **2014**, 144, 353–361.

[36] Wang, Y., Huang, L., Zhang, T. and Wang, Q., Hydrogen-rich syngas production from biomass pyrolysis and catalytic reforming using biochar-based catalysts, *Fuel*, **2022**, 313, 123006.

[37] Yu, M., Wang, K. and Vredenburg, H., Insights into low-carbon hydrogen production methods: Green, blue and aqua hydrogen, *Int. J. Hydrog. Energy*, **2021**, 46, 21261–21273.

[38] Bozzano, G. and Manenti, F., Efficient methanol synthesis: Perspectives, technologies and optimization strategies, *Prog. Energy Combust. Sci.*, **2016**, 56, 71–105.

[39] Studt, F., Behrens, M., Kunkes, E. L., Thomas, N., Zander, S., Tarasov, A., Schumann, J., Frei, E., Varley, J. B., Abild-Pedersen, F., Nørskov, J. K. and Schlögl, R., The Mechanism of CO and CO $_2$ Hydrogenation to Methanol over Cu-Based Catalysts, *ChemCatChem*, **2015**, 7, 1105–1111.

[40] Rui, N., Shi, R., Gutiérrez, R. A., Rosales, R., Kang, J., Mahapatra, M., Ramírez, P. J., Senanayake, S. D. and Rodriguez, J. A., CO $_2$ Hydrogenation on ZrO $_2$ /Cu(111) Surfaces: Production of Methane and Methanol, *Ind. Eng. Chem. Res.*, **2021**, 60, 18900–18906.

[41] Liu, Y.-M., Liu, J.-T., Liu, S.-Z., Li, J., Gao, Z.-H., Zuo, Z.-J. and Huang, W., Reaction mechanisms of methanol synthesis from CO/CO_2 hydrogenation on Cu_2O(111): Comparison with Cu(111), *J. CO2 Util.*, **2017**, 20, 59–65.

[42] Kang, J., He, S., Zhou, W., Shen, Z., Li, Y., Chen, M., Zhang, Q. and Wang, Y., Single-pass transformation of syngas into ethanol with high selectivity by triple tandem catalysis, *Nat. Commun.*, **2020**, 11, 827.

[43] Ail, S. S. and Dasappa, S., Biomass to liquid transportation fuel via Fischer Tropsch synthesis – Technology review and current scenario, *Renew. Sust. Energ. Rev.*, **2016**, 58, 267–286.

[44] Ojeda, M. and Rojas, S., *Biofuels from Fischer-Tropsch Synthesis*, Nova Science Publishers, Incorporated, New York, USA, **2010**.

[45] Hodala, J. L., Moon, D. J., Reddy, K. R., Reddy, C. V., Kumar, T. N., Ahamed, M. I. and Raghu, A. V., Catalyst design for maximizing C5+ yields during Fischer-Tropsch synthesis, *Int. J. Hydrog. Energy*, **2021**, 46, 3289–3301.

[46] Chen, W., Filot, I. A. W., Pestman, R. and Hensen, E. J. M., Mechanism of Cobalt-Catalyzed CO Hydrogenation: 2. Fischer–Tropsch Synthesis, *ACS Catal.*, **2017**, 7, 8061–8071.

[47] Cao, D.-B., Li, Y.-W., Wang, J. and Jiao, H., Chain growth mechanism of Fischer–Tropsch synthesis on Fe5C2(001), *J. Mol. Catal. A: Chem.*, **2011**, 346, 55–69.

[48] Erkey, C., Wang, J., Postula, W., Feng, Z., Phillip, C. V., Akgerman, A. and Anthony, R. G., Isobutylene production from synthesis gas over zirconia in a slurry reactor, *Ind. Eng. Chem. Res.*, **1995**, 34, 1021–1026.

[49] Khaodee, W., Jongsomjit, B., Assabumrungrat, S., Praserthdam, P. and Goto, S., Investigation of isosynthesis via CO hydrogenation over ZrO2 and CeO2 catalysts: Effects of crystallite size, phase composition and acid–base sites, *Catal. Commun.*, **2007**, 8, 548–556.

[50] Zhu, Z. and He, D., CO hydrogenation to iso-C4 hydrocarbons over CeO_2–TiO_2 catalysts, *Fuel*, **2008**, 87, 2229–2235.

[51] Zhang, R., Liu, H. and He, D., Pure monoclinic ZrO_2 prepared by hydrothermal method for isosynthesis, *Catal. Commun.*, **2012**, 26, 244–247.

[52] Wu, X., Tan, M., Tian, S., Song, F., Ma, Q., He, Y., Yang, G., Tsubaki, N. and Tan, Y., Designing ZrO_2-based catalysts for the direct synthesis of isobutene from syngas: The studies on Zn promoter role, *Fuel*, **2019**, 243, 34–40.

[53] Li, Y., He, D., Zhang, Q., Xu, B. and Zhu, Q., Influence of reactor materials on i-C4 synthesis from CO hydrogenation over ZrO_2 based catalysts, *Fuel Process. Technol.*, **2003**, 83, 39–48.

[54] Li, Y., He, D., Ge, S., Zhang, R. and Zhu, Q., Effects of CO_2 on synthesis of isobutene and isobutane from $CO_2/CO/H_2$ reactant mixtures over zirconia-based catalysts, *Appl. Catal. B: Environ.*, **2008**, 80, 72–80.

[55] Ganduglia-Pirovano, M. V., Hofmann, A. and Sauer, J., Oxygen vacancies in transition metal and rare earth oxides: Current state of understanding and remaining challenges, *Surf. Sci. Rep.*, **2007**, 62, 219–270.

[56] Helali, Z., Jedidi, A., Syzgantseva, O. A., Calatayud, M. and Minot, C., Scaling reducibility of metal oxides, *Theor. Chem. Acc.*, **2017**, 136, 100.

[57] Ruiz Puigdollers, A., Schlexer, P., Tosoni, S. and Pacchioni, G., Increasing Oxide Reducibility: The Role of Metal/Oxide Interfaces in the Formation of Oxygen Vacancies, *ACS Catal.*, **2017**, 7, 6493–6513.

[58] Hu, Z. and Metiu, H., Effect of Dopants on the Energy of Oxygen-Vacancy Formation at the Surface of Ceria: Local or Global?, *J. Phys Chem. C*, **2011**, 115, 17898–17909.

[59] Syzgantseva, O. A., Calatayud, M. and Minot, C., Revealing the Surface Reactivity of Zirconia by Periodic DFT Calculations, *J. Phys. Chem. C*, **2012**, 116, 6636–6644.

[60] Korpelin, V., Melander, M. M. and Honkala, K., Reducing the irreducible: Dispersed metal atoms facilitate reduction of irreducible oxides, *J. Phys. Chem. C*, **2022**, 126, 933–945.

[61] Mullins, D. R., The surface chemistry of cerium oxide, *Surf. Sci. Rep.*, **2015**, 70, 42–85.

[62] Noguera, C., *Physics and Chemistry at Oxide Surfaces*, Cambridge University Press, **1996**.

[63] Maleki, F. and Pacchioni, G., Characterization of Acid and Basic Sites on Zirconia Surfaces and Nanoparticles by Adsorbed Probe Molecules: A Theoretical Study, *Top. Catal.*, **2020**, 63, 1717–1730.

[64] Spezzati, G., Benavidez, A. D., DeLaRiva, A. T., Su, Y., Hofmann, J. P., Asahina, S., Olivier, E. J., Neethling, J. H., Miller, J. T., Datye, A. K. and Hensen, E. J., CO oxidation by Pd supported on CeO_2(100) and CeO_2(111) facets, *Appl. Catal. B: Environ.*, **2019**, 243, 36–46.

[65] Song, F., Bai, L., Moysiadou, A., Lee, S., Hu, C., Liardet, L. and Hu, X., Transition Metal Oxides as Electrocatalysts for the Oxygen Evolution Reaction in Alkaline Solutions: An Application-Inspired Renaissance, *J. Am. Chem. Soc.*, **2018**, 140, 7748–7759.

[66] Kinage, A. K., Upare, P. P., Kasinathan, P., Hwang, Y. K. and Chang, J.-S., Selective conversion of glycerol to acetol over sodium-doped metal oxide catalysts, *Catal. Commun.*, **2010**, 11, 620–623.

[67] Ruiz Puigdollers, A., Tosoni, S. and Pacchioni, G., Turning a Nonreducible into a Reducible Oxide via Nanostructuring: Opposite Behavior of Bulk ZrO_2 and ZrO_2 Nanoparticles Toward H_2 Adsorption, *J. Phys. Chem. C*, **2016**, 120, 15329–15337.

[68] Vayssilov, G. N., Lykhach, Y., Migani, A., Staudt, T., Petrova, G. P., Tsud, N., Skála, T., Bruix, A., Illas, F., Prince, K. C., Matolı´n, V., Neyman,

K. M. and Libuda, J., Support nanostructure boosts oxygen transfer to catalytically active platinum nanoparticles, *Nat. Mater.*, **2011**, 10, 310–315.

[69] Liu, Y., Wang, W., Xu, X., Marcel Veder, J.-P. and Shao, Z., Recent advances in anion-doped metal oxides for catalytic applications, *J. Mater. Chem. A*, **2019**, 7, 7280–7300.

[70] Migani, A., Vayssilov, G. N., Bromley, S. T., Illas, F. and Neyman, K. M., Greatly facilitated oxygen vacancy formation in ceria nanocrystallites, *Chem. Commun.*, **2010**, 46, 5936.

[71] Puigdollers, A. R., Illas, F. and Pacchioni, G., Structure and Properties of Zirconia Nanoparticles from Density Functional Theory Calculations, *J. Phys. Chem. C*, **2016**, 120, 4392–4402.

[72] Furuta, S., Matsuhashi, H. and Arata, K., Biodiesel fuel production with solid amorphous-zirconia catalysis in fixed bed reactor, *Biomass Bioenergy*, **2006**, 30, 870–873.

[73] Kouva, S., Review: monoclinic zirconia, its surface sites and their interaction with carbon monoxide, *Catal. Sci. Technol.*, **2015**, 5, 3473–3490.

[74] Yashima, M., Kakihana, M. and Yoshimura, M., Metastable-stable phase diagrams in the zirconia-containing systems utilized in solid-oxide fuel cell application, *Solid State Ion.*, **1996**, 86-88, 1131–1149.

[75] Zhang, Y. and Lawn, B., Novel Zirconia Materials in Dentistry, *J. Dent. Res.*, **2018**, 97, 140–147.

[76] Darolia, R., Thermal barrier coatings technology: critical review, progress update, remaining challenges and prospects, *Int. Mater. Rev.*, **2013**, 58, 315–348.

[77] Wu, X.-m., Tan, M.-h., Geng, H.-l., Zhao, S.-y., Xu, B. and Tan, Y.-s., Effect of crystal structure of ZrO_2 catalyst on isobutene synthesis from CO hydrogenation, *J. Fuel Chem. Technol.*, **2023**, 51, 473–481.

[78] Sinhamahapatra, A., Jeon, J.-P., Kang, J., Han, B. and Yu, J.-S., Oxygen-Deficient Zirconia (ZrO_2-x): A New Material for Solar Light Absorption, *Sci. Rep.*, **2016**, 6, 27218.

[79] Zaytseva, Y. A., Panchenko, V. N., Simonov, M. N., Shutilov, A. A., Zenkovets, G. A., Renz, M., Simakova, I. L. and Parmon, V. N., Effect of Gas Atmosphere on Catalytic Behaviour of Zirconia, Ceria and Ceria–Zirconia Catalysts in Valeric Acid Ketonization, *Top. Catal.*, **2013**, 56, 846–855.

[80] Mancera, R. R. C., Vaiss, V. S., Espino, O. E. E., de Avillez, R. R., Appel, L. G. and Costa, L. T., Zn-doping and oxygen vacancy effects on the reactivity and properties of monoclinic and tetragonal ZrO_2: a DFT study, *J. Mol. Model.*, **2022**, 28, 358.

[81] de Souza, E. F. and Appel, L. G., Oxygen vacancy formation and their role in the CO_2 activation on Ca doped ZrO_2 surface: An ab-initio DFT study, *Appl. Surf. Sci.*, **2021**, 553, 149589.

[82] Hengne, A. M., Samal, A. K., Enakonda, L. R., Harb, M., Gevers, L. E., Anjum, D. H., Hedhili, M. N., Saih, Y., Huang, K.-W. and Basset, J.-M., Ni-Sn-Supported ZrO $_2$ Catalysts Modified by Indium for Selective CO_2 Hydrogenation to Methanol, *ACS Omega*, **2018**, 3, 3688–3701.

[83] Stagg-Williams, S. M., Noronha, F. B., Fendley, G. and Resasco, D. E., CO2 Reforming of CH4 over Pt/ZrO2 Catalysts Promoted with La and Ce Oxides, *J. Catal.*, **2000**, 194, 240–249.

[84] López, D. E., Goodwin, J. G., Bruce, D. A. and Furuta, S., Esterification and transesterification using modified-zirconia catalysts, *Appl. Catal. A: Gen.*, **2008**, 339, 76–83.

[85] Grecea, M. L., Dimian, A. C., Tanase, S., Subbiah, V. and Rothenberg, G., Sulfated zirconia as a robust superacid catalyst for multiproduct fatty acid esterification, *Catal. Sci. Technol.*, **2012**, 2, 1500.

[86] Sun, J., Zhu, K., Gao, F., Wang, C., Liu, J., Peden, C. H. F. and Wang, Y., Direct Conversion of Bio-ethanol to Isobutene on Nanosized $Zn_xZr_yO_z$ Mixed Oxides with Balanced Acid–Base Sites, *J. Am. Chem. Soc.*, **2011**, 133, 11096–11099.

[87] Liu, X.-M., Lu, G. and Yan, Z.-F., Nanocrystalline zirconia as catalyst support in methanol synthesis, *Appl. Catal. A: Gen.*, **2005**, 279, 241–245.

[88] Frei, M. S., Mondelli, C., Cesarini, A., Krumeich, F., Hauert, R., Stewart, J. A., Curulla Ferré, D. and Pérez-Ramírez, J., Role of Zirconia in Indium Oxide-Catalyzed CO_2 Hydrogenation to Methanol, *ACS Catal.*, **2020**, 10, 1133–1145.

[89] Su, C., Li, J., He, D., Cheng, Z. and Zhu, Q., Synthesis of isobutene from synthesis gas over nanosize zirconia catalysts, *Appl. Catal. A: Gen.*, **2000**, 202, 81–89.

[90] Li, Y., He, D., Yuan, Y., Cheng, Z. and Zhu, Q., Selective Formation of Isobutene from CO Hydrogenation over Zirconium Dioxide Based Catalysts, *Energy Fuels*, **2001**, 15, 1434–1440.

[91] He, M.-Y., White, J. M. and Ekerdt, J. G., CO and CO_2 hydrogenation over metal oxides: a comparison of ZnO, TiO_2 and ZrO_2, *J. Mol. Catal.*, **1985**, 30, 415–430.

[92] Maruya, K.-i., Takasawa, A., Haraoka, T., Domen, K. and Onishi, T., Role of methoxide species in isobutene formation from CO and H_2 over oxide catalysts methoxide species in isobutene formation, *J. Mol. Catal. A: Chem.*, **1996**, 112, 143–151.

[93] Jackson, N. B. and Ekerdt, J. G., Isotope studies of the effect of acid sites on the reactions of C3 intermediates during isosynthesis over zirconium dioxide and modified zirconium dioxide, *J. Catal.*, **1990**, 126, 46–56.

[94] Radha, A. V., Bomati-Miguel, O., Ushakov, S. V., Navrotsky, A. and Tartaj, P., Surface Enthalpy, Enthalpy of Water Adsorption, and Phase Stability in Nanocrystalline Monoclinic Zirconia, *J. Am. Ceram. Soc.*, **2009**, 92, 133–140.

[95] Zhang, L., Zhou, M., Wang, A. and Zhang, T., Selective Hydrogenation over Supported Metal Catalysts: From Nanoparticles to Single Atoms, *Chem. Rev.*, **2020**, 120, 683–733.

[96] Aireddy, D. R. and Ding, K., Heterolytic Dissociation of H_2 in Heterogeneous Catalysis, *ACS Catal.*, **2022**, 12, 4707–4723.

[97] Syzgantseva, O., Calatayud, M. and Minot, C., Hydrogen Adsorption on Monoclinic (-111) and (-101) ZrO_2 Surfaces: A Periodic ab Initio Study, *J. Phys. Chem. C*, **2010**, 114, 11918–11923.

[98] Kondo, J., Sakata, Y., Domen, K., Maruya, K. and Onishi, T., Infrared study of hydrogen adsorbed on zro_2, *J. Chem. Soc., Faraday trans.*, **1990**, 86, 397–401.

[99] Tseung, A. C. C. and Chen, K. Y., Hydrogen spill-over effect on Pt/WO_3 anode catalysts, *Catal. Today*, **1997**, 38, 439–443, iSBN: 0920-5861, 1873-4308.

[100] Xiong, M., Gao, Z. and Qin, Y., Spillover in Heterogeneous Catalysis: New Insights and Opportunities, *ACS Catal.*, **2021**, 11, 3159–3172.

[101] Kouva, S., Andersin, J., Honkala, K., Lehtonen, J., Lefferts, L. and Kanervo, J., Water and carbon oxides on monoclinic zirconia: experimental and computational insights, *Phys. Chem. Chem. Phys.*, **2014**, 16, 20650–20664.

[102] Kauppinen, M. M., Melander, M. M., Bazhenov, A. S. and Honkala, K., Unraveling the Role of the Rh–ZrO_2 Interface in the Water–Gas-Shift Reaction via a First-Principles Microkinetic Study, *ACS Catal.*, **2018**, 8, 11633–11647.

[103] Larmier, K., Liao, W.-C., Tada, S., Lam, E., Verel, R., Bansode, A., Urakawa, A., Comas-Vives, A. and Copéret, C., CO_2 -to-Methanol Hydrogenation on Zirconia-Supported Copper Nanoparticles: Reaction Intermediates and the Role of the Metal-Support Interface, *Angew. Chem. Int. Ed.*, **2017**, 56, 2318–2323.

[104] Weigel, J., Koeppel, R. A., Baiker, A. and Wokaun, A., Surface Species in CO and CO_2 Hydrogenation over Copper/Zirconia: On the Methanol Synthesis Mechanism, *Langmuir*, **1996**, 12, 5319–5329.

[105] Jung, K. T. and Bell, A. T., The effects of synthesis and pretreatment conditions on the bulk structure and surface properties of zirconia, *J. Mol. Catal. A: Chem.*, **2000**, 163, 27–42.

[106] Graf, P., de Vlieger, D., Mojet, B. and Lefferts, L., New insights in reactivity of hydroxyl groups in water gas shift reaction on Pt/ZrO_2, *J. Catal.*, **2009**, 262, 181–187.

[107] Korhonen, S. T., Calatayud, M. and Krause, A. O. I., Structure and Stability of Formates and Carbonates on Monoclinic Zirconia: A Combined Study by Density Functional Theory and Infrared Spectroscopy, *J. Phys. Chem. C*, **2008**, 112, 16096–16102.

[108] Ouyang, F., Kondo, J. N., Maruya, K. and Domen, K., IR study on migration of $^{1}8OCH_3$ species on ZrO_2, *Catal. Lett.*, **1998**, 179–181.

[109] Bachiller-Baeza, B., Rodriguez-Ramos, I. and Guerrero-Ruiz, A., Interaction of Carbon Dioxide with the Surface of Zirconia Polymorphs, *Langmuir*, **1998**, 14, 3556–3564.

[110] Pokrovski, K., Jung, K. T. and Bell, A. T., Investigation of CO and CO_2 Adsorption on Tetragonal and Monoclinic Zirconia, *Langmuir*, **2001**, 17, 4297–4303.

[111] He, M.-Y. and Ekerdt, J. G., Methanol formation on zirconium dioxide, *J. Catal.*, **1984**, 90, 17–23.

[112] Yurkiv, V., Gorski, A., Bessler, W. G. and Volpp, H.-R., Density functional theory study of heterogeneous CO oxidation over an oxygen-enriched yttria-stabilized zirconia surface, *Chem. Phys. Lett.*, **2012**, 543, 213–217.

[113] Chen, H.-Y. T., Tosoni, S. and Pacchioni, G., A DFT study of the acid–base properties of anatase TiO_2 and tetragonal ZrO_2 by adsorption of CO and CO_2 probe molecules, *Surf. Sci.*, **2016**, 652, 163–171.

[114] Liu, Y., Xia, C., Wang, Q., Zhang, L., Huang, A., Ke, M. and Song, Z., Direct dehydrogenation of isobutane to isobutene over Zn-doped ZrO_2 metal oxide heterogeneous catalysts, *Catal. Sci. Technol.*, **2018**, 8, 4916–4924.

[115] Enkovaara, J., Rostgaard, C., Mortensen, J. J., Chen, J., Dułak, M., Ferrighi, L., Gavnholt, J., Glinsvad, C., Haikola, V., Hansen, H. A., Kristoffersen, H. H., Kuisma, M., Larsen, A. H., Lehtovaara, L., Ljungberg, M., Lopez-Acevedo, O., Moses, P. G., Ojanen, J., Olsen, T., Petzold, V., Romero, N. A., Stausholm-Møller, J., Strange, M., Tritsaris, G. A., Vanin, M., Walter, M., Hammer, B., Häkkinen, H., Madsen, G. K. H., Nieminen, R. M., Nørskov, J. K., Puska, M., Rantala, T. T., Schiøtz, J., Thygesen, K. S. and Jacobsen, K. W., Electronic structure calculations with GPAW: a real-space

implementation of the projector augmented-wave method, *J. Phys.: Condens. Matter*, **2010**, 22, 253202.

[116] Mortensen, J. J., Hansen, L. B. and Jacobsen, K. W., Real-space grid implementation of the projector augmented wave method, *Phys. Rev. B*, **2005**, 71, 035109.

[117] Larsen, A. H., Mortensen, J. J., Blomqvist, J., Castelli, I. E., Christensen, R., Dułak, M., Friis, J., Groves, M. N., Hammer, B., Hargus, C., Hermes, E. D., Jennings, P. C., Jensen, P. B., Kermode, J., Kitchin, J. R., Kolsbjerg, E. L., Kubal, J., Kaasbjerg, K., Lysgaard, S., Maronsson, J. B., Maxson, T., Olsen, T., Pastewka, L., Peterson, A., Rostgaard, C., Schiøtz, J., Schütt, O., Strange, M., Thygesen, K. S., Vegge, T., Vilhelmsen, L., Walter, M., Zeng, Z. and Jacobsen, K. W., The atomic simulation environment—a python library for working with atoms, *J. Phys.: Condens. Matter*, **2017**, 29, 273002.

[118] Perdew, J. P., Burke, K. and Ernzerhof, M., Generalized Gradient Approximation Made Simple, *Phys. Rev. Lett.*, **1996**, 77, 3865–3868.

[119] Tkatchenko, A. and Scheffler, M., Accurate Molecular Van Der Waals Interactions from Ground-State Electron Density and Free-Atom Reference Data, *Phys. Rev. Lett.*, **2009**, 102, 073005.

[120] Hanwell, M. D., Curtis, D. E., Lonie, D. C., Vandermeersch, T., Zurek, E. and Hutchison, G. R., Avogadro: an advanced semantic chemical editor, visualization, and analysis platform, *J. Cheminformatics.*, **2012**, 4, 17.

[121] Henkelman, G., Uberuaga, B. P. and Jónsson, H., A climbing image nudged elastic band method for finding saddle points and minimum energy paths, *J. Chem. Phys.*, **2000**, 113, 9901–9904.

[122] Scipy, Documentation for nelder-mead optimization, `https://docs.scipy.org/doc/scipy/reference/optimize.minimize-neldermead.html`, Last accessed on 2023-1.9.

[123] Chrétien, S. and Metiu, H., Acid–Base Interaction and Its Role in Alkane Dissociative Chemisorption on Oxide Surfaces, *J. Phys. Chem. C*, **2014**, 118, 27336–27342.

[124] Rabone, J. and Van Uffelen, P., DFT-based Metadynamics simulation of proton diffusion in tetragonal zirconia at 1500 K, *J. Nucl. Mater.*, **2015**, 459, 30–36.

[125] Tuckerman, M., Laasonen, K., Sprik, M. and Parrinello, M., Ab initio molecular dynamics simulation of the solvation and transport of hydronium and hydroxyl ions in water, *J. Chem. Phys.*, **1995**, 103, 150–161.

[126] Scipy, Documentation for kernel density estimation, `https://docs.scipy.org/doc/scipy/reference/generated/scipy.stats.gaussian_kde.html`, Last accessed on 2023-4.5.

Appendix

1. GPAW structure optimization script
2. Path interpolation script, 2 p.
3. GPAW NEB script, 2 p.
4. GPAW DFT-MD script, 2 p.

APPENDIX 1

```
from ase.io import read
from ase.optimize import BFGS
from gpaw import GPAW, PW, Mixer, FermiDirac
from ase.calculators.vdwcorrection import vdWTkatchenko09prl
from gpaw.analyse.hirshfeld import HirshfeldDensity, HirshfeldPartitioning
from gpaw.analyse.vdwradii import vdWradii


surf = read("mZrO2_-212_3_layers_c_COH_H_tst_2.traj") # luettava rakenne
surf.set_pbc([True, True, False]) # jaksollinen vain tasossa

# output-tiedostonimen perusosa
f = "mmZrO2_-212_3_layers_c_COH_H_tst_2_opt"

# laskimen saadot
calc = GPAW(xc='PBE',
            mode='fd',
            gpts=(60,32,156),
            kpts=(4,4,1),
            maxiter=599,
            setups={'Zr': ':d,1.9'},
            mixer=Mixer(0.364, 100, 104),
            txt=f+'.txt')


# van der Waals -laskin
radii = vdWradii(surf.get_chemical_symbols(), 'PBE')
cc = vdWTkatchenko09prl(HirshfeldPartitioning(calc),
                        radii,
                        vdWDB_alphaC6={'Zr': [112, 1360],
                                       'O': [5.4, 15.6],
                                       'C': [12, 46.6],
                                       'H': [4.5, 6.5]})

surf.set_calculator(cc)

# geometrian optimointialgoritmi
opt = BFGS(surf, logfile=f+'.log', trajectory=f+'.traj')
opt.run(fmax=0.05)
```

APPENDIX 2 (1/2)

```
from ase.io import read, write, Trajectory
from ase.neb import NEB
from ase.autoneb import AutoNEB
from ase.optimize import BFGS, FIRE
#from ase.parallel import rank, size, parprint
from ase.parallel import world, parprint
from gpaw import GPAW, Mixer, FermiDirac
from gpaw.poisson import PoissonSolver
from gpaw.eigensolvers import Davidson
from gpaw.utilities import h2gpts
from ase.calculators.vdwcorrection import vdWTkatchenko09prl
from gpaw.analyse.hirshfeld import HirshfeldDensity,HirshfeldPartitioning
from gpaw.analyse.vdwradii import vdWradii

# read in the neb path
images = []
for i in range(0,7):
        image = read('neb{:03d}.traj'.format(i))
        images.append(image)
# set up parallelization
mobile = len(images) - 2 # number of moving (i.e. non-endpoint) images
n = world.size // mobile
j = 1 + world.rank // n
assert mobile * n == world.size

# set calculator for each image
for i in range(1,mobile+1):
        image = images[i]
        ranks = range((i-1)*n, (i)*n)
        if world.rank in ranks:
                c = GPAW(xc='PBE',
                         mode='fd',
                         gpts=(60,32,156),
                         kpts=(4,4,1),
                         maxiter=599,
                         txt='neb{:03d}.txt'.format(i),
                         communicator=ranks,
                         setups={'Zr': ':d,1.9'},
                         mixer=Mixer(0.364, 100, 104))

                radii = vdWradii(image.get_chemical_symbols(), 'PBE')
                cc = vdWTkatchenko09prl(HirshfeldPartitioning(c),
                                        radii,
                                        vdWDB_alphaC6={'Zr': [112, 1360],
                                                       'O': [5.4, 15.6],
                                                       'C': [12, 46.6],
                                                       'H': [4.5, 6.5]})
                image.set_calculator(cc)

# do normal NEB until forces reasonable
neb = NEB(images, parallel=True, climb=False, method='eb')
```

```
opt = FIRE(neb, logfile='neb.log')
if world.rank % n == 0:
        traj = Trajectory('neb{:03d}.traj'.format(j), 'a', images[j], master=True)
        opt.attach(traj)
opt.run(fmax=0.15)

# switch to climbing image to finalize
neb = NEB(images, parallel=True, climb=True, method='eb')
opt = FIRE(neb, logfile='neb.log')
if world.rank % n == 0:
        traj = Trajectory('neb{:03d}.traj'.format(j), 'a', images[j], master=True)
        opt.attach(traj)
opt.run(fmax=0.05)
```

```
from ase import *
from ase.io import read, write, PickleTrajectory
from ase.optimize import FIRE, BFGS
from ase.parallel import parprint, rank, size
#from gpaw import *
#from gpaw.utilities.timing import ParallelTimer
from ase.neb import *
import argparse

desc = 'Create␣a␣NEB␣path␣using␣existing␣structures␣at␣selected␣points␣of␣the␣path.\n\
First␣and␣last␣files␣provided␣must␣be␣endpoints␣of␣the␣path.␣(I.e.␣the␣script\n\
does␣not␣extrapolate.)\n\
NB:␣the␣images␣are␣zero-indexed!\n\
NB:␣the␣images␣must␣be␣provided␣in␣the␣right␣order!\n\
Usage␣example:\n\
python␣interpolate.py␣-f␣a.traj␣b.traj␣c.traj␣d.traj␣-i␣0␣4␣6␣7␣-o␣neb\n\
This␣creates␣an␣8-image␣NEB␣path␣with␣a.traj␣and␣d.traj␣at␣the␣ends,␣b.traj\n\
at␣image␣4␣and␣c.traj␣at␣image␣6.␣The␣rest␣are␣interpolated␣with␣the␣idpp\n\
scheme,␣and␣the␣files␣are␣named␣as␣neb000..neb007.traj.\
'

parser = argparse.ArgumentParser(description=desc,
            formatter_class=argparse.RawDescriptionHelpFormatter)
parser.add_argument('--files', '-f', type=str, nargs='+')
parser.add_argument('--indices', '-i', type=int, nargs='+')
parser.add_argument('--out', '-o', type=str, default='neb')

args = parser.parse_args()
files = args.files
indices = args.indices
out = args.out

assert indices == sorted(list(set(indices))), "Indices␣must␣be␣different␣and␣in␣order."
assert 0 in indices, "Index␣list␣must␣include␣0␣(first␣image)."
assert len(files) >= 2, "At␣least␣2␣files␣needed."
assert len(files) == len(indices),\
"The␣number␣of␣files␣has␣to␣be␣the␣same␣as␣the␣number␣of␣indices."

first = files[indices.index(0)]
path = [first]*(max(indices)-1)

for i in range(len(indices)-1):
    image1 = read(files[i])
    image2 = read(files[i+1])
    index1 = indices[i]
    index2 = indices[i+1]
    images = [image1]
    images += [image1.copy() for i in range(index2-index1-1)]
    images += [image2]
    neb = NEB(images)
```

```
    if len(images) >= 3:
        neb.interpolate('idpp')
#         neb.interpolate()
    path[index1:index2] = neb.images

for i in range(indices[-1]+1):
    write(out+'{:03d}.traj'.format(i), path[i])
```

```
from ase.md import MDLogger
from gpaw import *
from ase import *
from ase.io import *
from ase.md.langevin import Langevin
from ase.md.nvtberendsen import NVTBerendsen
from ase.md.verlet import VelocityVerlet
from ase.md.npt import NPT
from ase.units import fs,kB
from ase.md.velocitydistribution import MaxwellBoltzmannDistribution
from ase.parallel import paropen
from ase.calculators.vdwcorrection import vdWTkatchenko09prl
from gpaw.analyse.hirshfeld import HirshfeldDensity, HirshfeldPartitioning
from gpaw.analyse.vdwradii import vdWradii

# set the system

to_read = 1
to_write = to_read + 1
base_file = 'mZrO2_syngas_5'
file_type = '.traj'

atoms = read('{0}{1}{2}'.format(to_read,base_file,file_type))
atoms.set_pbc([True, True, True])

for atom in atoms:
    if atom.symbol == 'H':
        atom.mass = 2.

calc = GPAW(gpts=(60,64,156),
            xc='PBE',
            mode='lcao',
            spinpol=False,
            basis='dzp',
            txt='{0}{1}.txt'.format(to_write,base_file),
            parallel={'sl_auto' : True},
            setups={'Zr': ':d,1.9'},
            mixer=Mixer(0.364, 100, 104),
            convergence={'eigenstates': 1.0e-4,
                         'density': 1.0e-5,
                         'energy': 1.0e-4})
atoms.set_calculator(calc)
atoms.get_potential_energy()


radii = vdWradii(atoms.get_chemical_symbols(), 'PBE')
cc = vdWTkatchenko09prl(HirshfeldPartitioning(calc), radii,
                        vdWDB_alphaC6={'Zr': [112, 1360],
                                       'O': [5.4, 15.6],
                                       'C': [12, 46.6],
                                       'H': [4.5, 6.5]})
```

```
atoms.set_calculator(cc)
atoms.get_potential_energy()

# temperature setup
T = 700  # K
ET = kB*T  # kBT --> temperature in eV
MaxwellBoltzmannDistribution(atoms, temperature_K = T)

# Langevin NVT dynamics
dyn = Langevin(atoms, 1.*fs, temperature=ET, friction=0.02)

# NVE dynamics
#dyn = VelocityVerlet(atoms, timestep=1.*fs)

# attach log, traj and velocity
dyn.attach(MDLogger(dyn, atoms, '{0}{1}.log'.format(to_write,base_file), header=True, stress=False,
           peratom=False, mode="a"), interval=10)

traj = Trajectory('{0}{1}{2}'.format(to_write,base_file,file_type), 'w', atoms)
dyn.attach(traj.write, interval=1)

# run
dyn.run(steps=2000)
traj.close()
```